Tribocorrosion under fluid lubrication: Modeling wear of CoCrMo artificial hip joints

PAR

Shoufan CAO

ÉCOLE POLYTECHNIQUE
FÉDÉRALE DE LAUSANNE

Suisse
2016

Acknowledgements

Firstly, I would like to express my sincere appreciation to my supervisor Dr. Stefano Mischler, who gave me the precious opportunity to join his Tribology and Interface Chemistry (TIC) group to do my PhD thesis. I greatly appreciate the professional guidance, time, patience and encouragement he devoted to me in these four years. What impressed me the most is that every time when I was facing some difficulties, he could always give me inspiring ideas to tackle the problem, which speeded up a lot the progress of my PhD research. I am grateful to the very valuable discussions with him, after which my passion in research was always been exited to the highest level. This thesis is impossible to be finished without his numerous help. Also, I thank him a lot for giving me so many opportunities to attend international conferences to learn the frontier knowledge and develop network.

Then, I want to thank the experts in the jury committee of my defense, Prof. Nuria Espallargas from NUST, Norway, Dr. Claude Rieker from Zimmer Biomet, Switzerland, and Prof. Stephen Ferguson from ETHZ, as well as the president of the jury committee Prof. Patrik Hoffmann from EPFL.

I would like to thank the current and ancient members of the TIC group as well as the people who were working in the group temporally for creating very nice working atmosphere and all the help they gave me. Firstly, I want to acknowledge the nice TIC PhD student group: Sandra Guadalupe was the only PhD student when I joined the group and she gave me numerous instructions and help from the scientific research to the EPFL campus life as well as the daily life in Lausanne. Special thanks to the other PhD students in this group: Angela Bermudez, Leili Batooli, Fabio Cova, Valentine Magnin and Vance Nguyen. We spent so much time together and I really enjoyed all the activities we organized together. I appreciate a lot their company which makes my PhD life much more colorful. I am grateful to Pierre Mettraux for the SEM and XPS analysis as well as the mechanical and electrical technical work he did for me in my tribometer and the lab facilities I was using. Nicolas Xanthopoulos should also be acknowledged

Abstract

Wear is still the key problem causing the failure and limiting the lifetime of artificial hip joints, especially for the polymer acetabular cup in the metal-on-polymer and ceramic-on-polymer articulations. To reduce the wear, metal-on-metal articulation has been developed but the continuous release of nano-sized metal ions and particles into the body is of long-term concern of the patient's health.

The implanted artificial hip joints are surrounded by synovial fluid, which on one hand acts as lubricant, alleviating the wear of implants but on the other hand introduces corrosion to the metal components. The interaction between wear and corrosion, called tribocorrosion, has been proposed as one of the crucial degradation mechanisms of metal implants. Tribocorrosion models have been developed in the past neglecting however lubrication effects. This constitutes the motivation for this work which aims at developing a composite wear model considering both tribocorrosion and lubrication effects to quantitatively describe and predict material degradation of passive metals (typically CoCrMo alloys) in hip joints.

Based on the plastic deformation of the contacting asperities, an existing tribocorrosion model was expanded in order to include the lubrication effects by replacing the total normal load by the effective normal load which is the load carried only by the contacting asperities. The difference between these two loads is the load carried by the hydrodynamic fluid film flowing through the asperity junctions. The effective normal load was related to the total normal load based on Dowson's empirical running-in wear and minimum hydrodynamic film thickness correlation, which was derived from a large number of CoCrMo metal-on-metal hip joint simulator results. The composite model was then calibrated using well-controlled tribocorrosion experiments carried out in a dedicated tribometer from the literature.

The calibrated model was found predicting precisely wear rates observed in tribometers and the running-in wear rates of metal-on-metal hip joints tested

in simulators published in the literature. The model also allows identifying the dominating wear mechanisms (mechanical or chemical) and evaluating the influence of well-defined material, mechanical, electrochemical and physical parameters. The model could be successfully applied to other CoCr alloys of different carbide concentrations provided plastic deformation of the asperities remains the prevailing wear mechanism, as postulated in the model.

In an attempt to further generalize the model, Dowson's empirical correlation was tentatively replaced by a mechanistic approach describing the real contact area and thus the effective normal force as a function of the topography of the contact surface and the hydrodynamic film thickness. The validity of the approach was assessed using tribocorrosion experiments carried out in H_2SO_4 – glycerol solutions exhibiting different viscosities. The topography was described using experimental Abbott – Firestone curves of the wear surface profile after cut-off of the waviness. The experimental mechanical and chemical wear rates were found to be consistent with this model approach. This shows that surface topography should be included in more general tribocorrosion models. However, tools to anticipate the evolution of surface topography during wear are not available at present and this limits the possibility of the model to predict tribocorrosion rate.

Keywords: Tribocorrosion, Lubrication, Modeling, Wear, CoCrMo alloys, Artificial hip joints

Résumé

L'usure est toujours le principal problème provoquant l'échec et limitant la durée de vie des articulations d'hanche artificielles, en particulier pour les combinaisons cupule cotyle en polymère et têtes fémorales en métalliques ou céramique. Pour réduire l'usure, le couplage métal-métal a été mis au point. Cependant, le relargage continu dans le corps de ions et de particules métalliques de taille nanométrique constitue une préoccupation à long terme.

Les articulations des hanches artificielles implantées sont entourées par le liquide synovial, qui d'une part agit comme lubrifiant, réduisant ainsi l'usure, mais d'autre part, introduit le risque de corrosion des composants métalliques. L'interaction entre l'usure et la corrosion, dite tribocorrosion, a été proposée comme l'un des mécanismes essentiels de la dégradation des implants métalliques. Les modèles de tribocorrosion développés par le passé ont négligent les effets de lubrification. Cet état de fait constitue la motivation pour ce travail qui vise à développer un modèle d'usure composite tenant compte des effets de tribocorrosion et de lubrification pour décrire quantitativement la dégradation des métaux passifs (type alliage CoCrMo) dans les articulations de la hanche.

Un modèle existant de tribocorrosion, basé sur la déformation plastique des aspérités en contact, a été modifié de manière à inclure les effets de lubrification par le remplacement de la force normale totale par la force normale effective, c.à.d. la charge supportée uniquement par les aspérités en contact. La force normale effective est reliée à la force normale totale par l'élaboration d'une relation empirique proposée par Dowson reliant l'usure d'articulations de l'hanche type métal sur métal avec l'épaisseur minimale du film hydrodynamique. Le modèle composite a ensuite été étalonné en utilisant des expériences de tribocorrosion bien contrôlées menées en laboratoire avec un tribomètre dédié.

Le modèle calibré prédit avec précision les taux d'usure observés dans les tribomètres ainsi que l'usure mesurée en phase de rodage sur simulateurs de hanche et publiées dans la littérature scientifique. Le modèle permet également l'identification des mécanismes d'usure dominant (mécanique ou chimique) et

d'évaluer l'influence de facteurs mécaniques, électrochimiques et physiques. Le modèle peut être appliqué avec succès à d'autres alliages CoCr avec des concentrations en carbure différentes selon la déformation plastique des aspérités reste le mécanisme d'usure dominant, tel que postulé dans le modèle.

Dans une tentative de généraliser le modèle, la relation empirique Dowson a été provisoirement remplacée par une approche mécaniste décrivant la surface de contact réelle, et par conséquent la force normale effective, en fonction de la topographie de la surface de contact et l'épaisseur du film hydrodynamique. La validité de l'approche a été évaluée à l'aide d'expériences de tribocorrosion réalisées dans des mélanges de solution acide sulfurique et glycérol présentant différentes viscosités. Les prédictions du modèle modifié sont cohérentes avec les résultats expérimentaux. Cela montre que la topographie de la surface doit être incluse dans des modèles plus généraux de tribocorrosion. Cependant, les outils pour anticiper l'évolution de la topographie de la surface lors de l'usure ne sont pas disponibles à l'heure actuelle et cela limite la possibilité de prédire précisément le taux de tribocorrosion.

Mots-clés: Tribocorrosion, Lubrification, Modélisation, Usure, Alliages CoCrMo, Articulations d'hanche artificielles

Table of Contents

Chapter 1 Introduction

Hip joints provide an important movement of the human body. Unfortunately, the natural hip joints sometimes lose functionality as a consequence of diseases or accidents. Artificial hip joints have been studied and clinically used to replace the disabled natural joints since the 1950s [1,2]. They helped and help a multitude of patients recover the functionality of their hip joints.

Wear is still one of the key problems causing the failure and limiting the lifetime of artificial hip joints, especially for the polymer acetabular cups. So, extensive wear studies are essential to understand wear mechanisms and evaluate design factors. Considering the materials for the head-cup bearing, polymer coupled with metal or ceramic was used to ensure low friction. However, soft polymers usually undergo large wear causing the release of a large amount of micrometer-size wear debris inducing in turn osteolysis and aseptic loosening of the implants (wear particle disease) [3,4]. Metal-on-metal (MoM) and ceramic-on-ceramic (CoC) articulations were developed as a low wear alternative to polymers. However, these articulations may release large amounts of metallic ions by contact with the corrosive body fluids [3,5,6]. This constitutes a potential health risk if those ions enter organs such as liver or spleen [7].

There is thus a clear clinical interest in minimizing the material release from artificial hip joints. This constitutes the rationale for investigating the involved material release mechanisms and for developing appropriate models correlating materials degradation to well-defined physical parameters. This study aims thus at developing a predictive mechanistic based degradation model of CoCrMo artificial hip joints by combining existing tribocorrosion and lubrication formalisms.

The background of the wear studies of artificial hip joints and the involved mechanisms for MoM artificial hip joints such as tribocorrosion and lubrication will be reviewed in Chapter 2. The existing wear models for artificial hip joints will also be reviewed. From these, the objective of the thesis will be fixed.

Then, a composite wear model for MoM artificial hip joints will be developed in Chapter 3, which combines tribocorrosion and lubrication aspects. The model is based on the plastic deformation of the contacting metal asperities and correlates Archard's mechanical wear model, wear accelerated corrosion model and an empirical MoM hip joint wear versus minimum hydrodynamic film thickness equation (Dowson's equation) found in literature.

Then, the model will be calibrated using a well-controlled tribocorrosion study carried out in a tribometer found in the literature. Tribocorrosion studies of CoCr alloys of different carbide concentrations will be used to assess the applicability of the model to different CoCr alloys.

In Chapter 4, the model predictions will be compared to several experimental studies (carried out in both tribometers and simulators). Due to the lack of the values of the passivation charge density, before comparison, the passivation charge densities of a CoCrMo alloy in three solutions at different passive potentials are measured and compared to literature data, which reveal the linear dependency on potential of passivation charge density for CoCrMo alloys. This constitutes a method to estimate passivation charge density of CoCrMo alloys based on applied potential.

In Chapter 5, the model will be validated for MoM artificial hip joints by comparing the model predictions with simulator experimental results published in the literature. A thorough literature review is made in order to extract the experimental parameters and wear results. Then, the parameters will be applied to the model to predict the running-in wear rates and compared to experimental results. From the good correlation between model predictions and experimental results, the model will be validated to predict the running-in wear rates of MoM artificial hip joints.

The usefulness of the model will be demonstrated in Chapter 6 by showing instructive predictions the model can give, such as the instantaneous mechanical, chemical and total wear rates in one gait cycle of the human's walking. The effect of the involved parameters can also be evaluated by the model, which gives useful information about how to reduce the wear of MoM artificial hip joints by optimizing the design of the essential parameters and about how to choose the most compatible hip implants for individual patient.

The generalization of the model to other conditions is limited by the empirical nature of Dowson's correlation. So, in Chapter 7, an attempt is made to develop a mechanistic model to describe the effective normal load. The approach is based on the topography of the asperities and the hydrodynamic fluid film thickness. Then, the new effective normal load model will be incorporated into the tribocorrosion model to develop the composite model and comparison between model predictions and one set of experimental results will be carried out in order to validate the model.

Finally, Chapter 8 will give a general discussion and the conclusions will be presented in Chapter 9.

Chapter 2 State of the art

2.1 Wear of artificial hip joints

Hip joint, involving femoral head and acetabulum, provides one of the most important movements of the human body. The two parts are wrapped in a capsule, well lubricated and nourished by synovial fluid [8], as shown in Figure 2.1. Unfortunately, the natural hip joint sometimes loses functionality as a consequence of diseases or accidents. Hip joint replacement is a common clinical solution in such events and artificial hip joints have been studied and clinically used to replace the disabled natural joints since the 1950s [1,2], which help lots of patients recovering the functionality of hip joints.
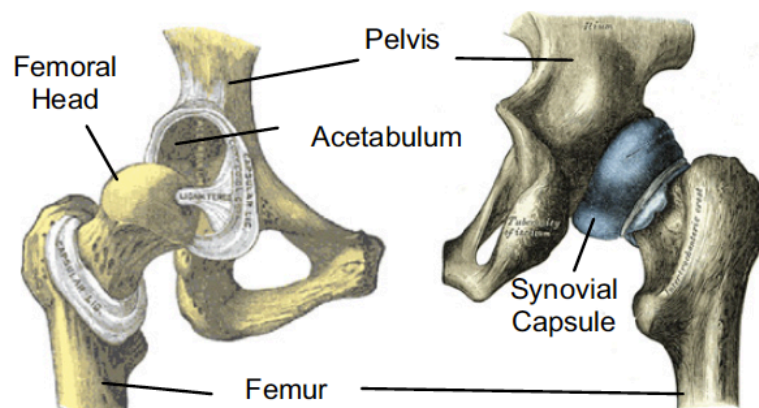
Figure 2.1 Anatomy of natural hip joint [8]

Nowadays, with the development of material, mechanical, chemical and medical technology, artificial joint replacements are more and more effective in providing normal functions to the patients suffering from severe joint diseases. The joint replacement treatment has been continuously evolved, from hips and knees to other major synovial joints, e.g. lumbar, ankle, shoulder [9-11]. Only for the hip joint replacements, there are about 200,000 and 80,000 interventions per year in USA and UK, respectively, and they are estimated to increase of about 170% by 2030 [12]. However, wear induced failure is still a major factor limiting

the long-term performance of the joint replacements, particularly for younger and more active patients who expect a lifetime of artificial hip joints in excess of 20 years.

In principle, there are three parts in a total hip joint replacement (THR): acetabular cup which is fixed into the acetabulum on the pelvis, stem inserted into the femur and femoral head fixed on the top of the stem as well as contacting with acetabular cup, as shown in Figure 2.2(a). The selection of the biomaterials for the components of implants (especially for the bearing surfaces) is of great importance and directly determines the performance and lifetime of implants. Considering the THR, several materials have been used for the acetabular cup and femoral head and different articulations have been developed, as shown in Figure 2.2(b). The employed material couplings can be divided into two main families: low friction hard-on-soft material combinations (metal-on-polymer MoP and ceramic-on-polymer CoP) and low wear hard-on-hard bearings (metal-on-metal MoM, ceramic-on-ceramic CoC and ceramic-on-metal CoM). Although both designs constitute valid solutions, specific problems have appeared.

(b)

(a)   (c)   (d)
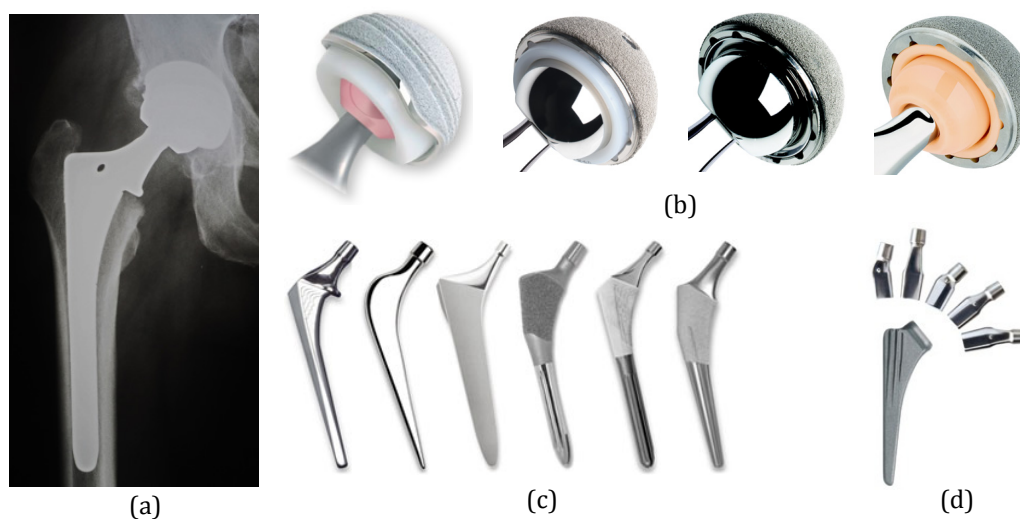
Figure 2.2 Artificial hip joint (a) and the main components: (b) head-cup articulation, (c) stem, (d) modular stem (images from OrthoInfo, Stryker Orthopaedics, Zimmer and Dr. Mohan Krishna A's blog)

In the low friction couplings, the soft polymer, usually ultra high molecular

weight polyethylene (UHMWPE), undergoes high wear causing the release of a large amount of micrometer-size wear debris that stimulate a cascade of reactions involving macrophages and giant cells, production of biochemical mediators of inflammation, cellular recruitment and bone resorption [13], ultimately causing osteolysis and aseptic loosening of the implant (wear particle disease) [3,4].

As alternatives, the hard MoM, CoC and CoM articulations exhibit much less wear than polymers. Released wear particles from the metals are of nanometer-size and can thus be phagocytized by macrophages [13]. However, MoM and CoM articulations may release large amounts of metallic ions by contact with the corrosive body fluids as indicated by the high ions levels in blood [14] found postoperatively in patients with THR. This constitutes a potential pathological risk if those ions enter organs such as liver or spleen [7]. Ceramics (alumina, zirconia) are usually associated with their brittle nature, which differently from the relatively soft wear of metals, can induce cracks of the ceramics and block the movement of the artificial hip joint, needing immediate revision of the implant [3].

The stem is usually made of titanium alloys due to their high biocompatibility, low weight and outstanding corrosion resistance [3]. Different shapes and surface finishing are proposed in order to enhance the fixation of the stem to the femur, as shown in Figure 2.2(c). Modular stems were also designed, with a separate neck connecting the femoral head and stem. By doing this, the length and inclination of the neck can be modified, as shown in Figure 2.2(d), in order to adapt the length and offset to specific patients. This design effectively reduces the time and amount of work in the preparation of the stem. However, it introduces one more interface (between the stem and the neck) to the artificial hip joint system, which has been found to initiate fretting wear and corrosion problems [15,16]. In addition to that, no matter separate neck is used or not, fretting and corrosion also happen in the interfaces between the femoral head and stem (or neck) taper and between the stem and the bone [17].

There is thus a clear clinical interest in minimizing the material release from artificial hip joints. Extensive wear studies are essential to understand wear mechanisms and evaluate design factors. This study focuses on the wear at the

interface between the femoral head and acetabular cup of MoM artificial hip joints. For MoM hip joints, the implanted metals are surrounded by synovial fluid which is a complex water based solution containing chemically aggressive constituents such as sodium chloride, hyaluronic acid, etc, as shown in Table 2.1 [18]. On one hand, synovial fluid provides a corrosive medium for the implant metals. Clear evidence of wear and corrosion has been detected in explants [3,19-21] where metal debris was generated by the combined effect of these two degradation mechanisms which is usually called tribocorrosion. On the other hand, synovial fluid acts as lubricants, alleviating the wear of artificial hip joints [8,22,23]. These two aspects will be described in details in the following sections.

Table 2.1 Major constituents of synovial fluid [18]

Constituent	Content [g/L]
Water	970.00
Sodium	3.30
Potassium	0.16
Calcium	0.06
Chloride	3.80
Protein	20.33
Hyaluronic acid	3.20

In the literature, wear of hip joints was investigated in vitro using either tribometers (material testing) or simulators (component testing). Tribometers usually employ a simple configuration such as ball-on-flat or pin-on-disc under simple movement with constant loads and speeds. While simulators are designed to follow the same geometrical configuration (ball-in-socket) of artificial hip joints and apply similar mechanical loading and motion of hip joints established during a gait in order to mimic the real condition. Tribometers are very flexible, normally not specific situation oriented, and can be easily coupled with electrochemical set-ups. Most of the mechanical and electrochemical parameters can be well controlled so that the effect of the involved parameters can be studied. Thus, tribometers are more suitable for mechanism investigations, while imulator tests, of course, are closer to the real conditions. However, certain parameters are not constant (e.g. normal load, sliding speed) or not easy to be

measured (e.g. wear volume), which leads to the results complicated to interpret. And, in order to simulate the lifetime of artificial hip joints, it takes long time to carry out the tests, e.g. 5 million cycles. In addition, it is not easy to couple electrochemical set-ups to monitor the corrosion responses in hip joint simulator.

2.2 Tribocorrosion

Tribocorrosion is a material degradation or transformation induced by simultaneous action of wear and corrosion [6]. It is found in many engineering applications such as biomedical implants, chemo-mechanical polishing, nuclear power plants, mining equipment, and food processing devices [24].

Most corrosion resistant metals or alloys generate an insoluble oxide layer (passive film) on their surface, which acts as a barrier against the release of ions. This is called "passivation". The passive film is usually just several nanometers thick but can effectively prevent the corrosion of the metal substrate [24,25]. However, if wear exists in the system, which damage the passive film and expose the much more active bare metal surface to the solution (named depassivation), corrosion of metal continues until the surface is been passivated again (repassivation). This is defined as wear accelerated corrosion, a phenomenon that together with mechanical wear contributes to the overall degradation in tribocorrosion [6,24-26]. If cyclic wear presents inducing continuous depassivation/repassivation cycles of the passive metal, the material degradation can be significantly increased.

The consequences of coupling wear and corrosion are complex. It is not just simply the sum of the wear in the absence of corrosive medium and corrosion in absence of wear. Friction and wear indeed modify the sensitivity of material to corrosion and conversely corrosion modifies the conditions of friction. The interaction between mechanical and chemical factors governing tribocorrosion is not yet fully understood [6,24].

2.2.1 Tribocorrosion experimental set-up

Tribocorrosion can be studied experimentally in laboratories under well-

controlled electrochemical conditions by coupling the mechanical and electrochemical methods. In principle, a tribometer is needed to generate a mechanical movement such as reciprocating sliding and a potentiostat is used to impose different potentials and measure the current. Figure 2.3 shows a schematic of a typical potentiostatic set-up for tribocorrosion measurements [24]. A specific potential between the working electrode (WE) and reference electrode (RE) can be applied using a potentiostat by passing an appropriate current between the working electrode and counter electrode (CE). The evolution of the current can be recorded which represent the tribocorrosion responds of the metal. In addition, the connection between the WE and CE can be disabled to do tribocorrosion tests under open circuit potential (OCP) and similarly do galvanic tribocorrosion tests with the WE and RE disconnected. Mischler [24] reviewed the different tribocorrosion techniques, which showed the different possibilities to incorporate electrochemical methods into tribometer to study the tribocorrosion mechanisms.
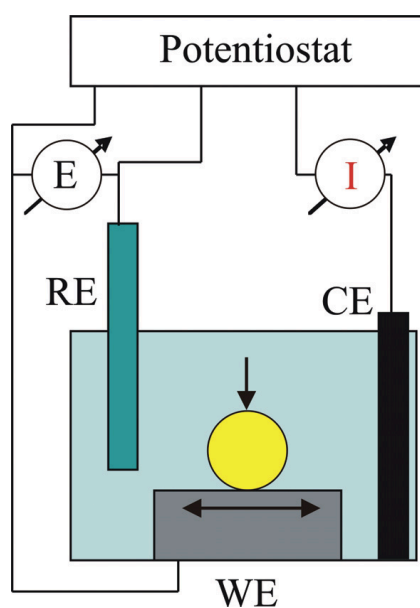
Figure 2.3 Schematic of a typical potentiostatic set-up for tribocorrosion measurements [24]

The group at the University of Leeds is currently developing electrochemical set-ups to be applied to hip joint simulators [27,28], as shown a schematic in Figure 2.4. Due to the special configuration and complex movements of the hip joint simulator, electrochemical cell is not easy to be

incorporated. For example, all the metal parts except the investigating surfaces of the head and cup should be well isolated from the solution in the cell in order to avoid galvanic coupling between different metallic pieces. The reference electrode should be as close as possible to the contacting area between the head and cup to avoid ohmic resistance of the body-simulated solution, which is not easy to guarantee due to the large movement of the head. Nevertheless, OCP was measured in their simulator experiments and the passivation of the CoCrMo alloys was found feathered by the cathodic shift of the potential at the onset of the motion and potential recovery when the motion is stopped [27,28], which has been commonly observed in tribometer tribocorrosion experiments [24].
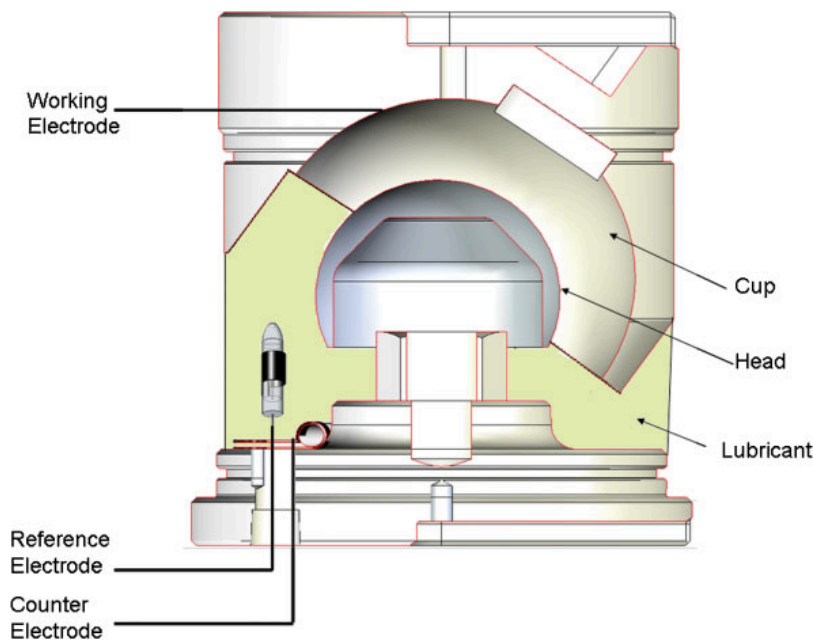
Figure 2.4 Schematic of a typical hip joint simulator station incorporated with electrochemical devices [27]

Using these experimental methods, the passivation and depassivation of passive metals have been clearly shown in the potential step and tribocorrosion experiments. As shown in Figure 2.5(a), using a three-electrode set-up demonstrated in Figure 2.4(a) without the rubbing ball, after applying a cathodic potential which suppress the oxidation of the metal, the current jumps to a very high value (oxidation of the metal) when the applied potential is switched from cathodic to an anodic value. Then, the current decreases quickly to a very low value, which shows the passivation of the metal. As another sample, in

reciprocating tribocorrosion tests (Figure 2.5b), when the rubbing starts, the current increases immediately because of the depassivation of the metal (break down of the passive film) and when the rubbing stops, the current decreases dramatically and promptly due to the passivation of the metal.

(a)

(b)
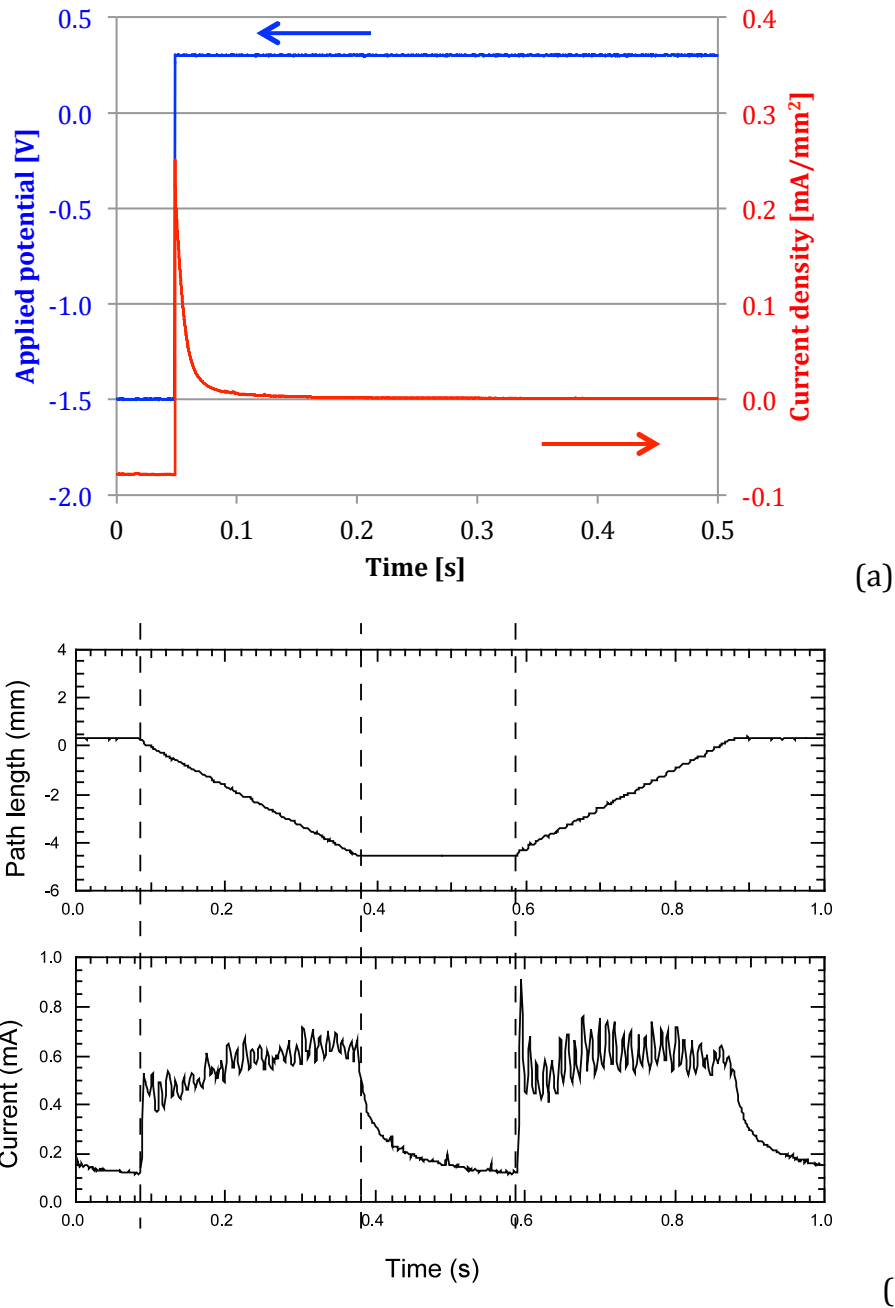
Figure 2.5 Experimental evidence of the passivation and depassivation of passive metals [29,30]

2.2.2 The effect of electrochemical conditions

Electrochemical conditions are essential to the corrosion behavior of

passive metals. This is well represented by polarization curve that shows the extent of current density at specific potentials. Figure 2.6 shows the typical anodic partial polarization curve of passive metals with three domains in the curve. After OCP that is the electric potential difference established spontaneously between metal and solution, the metal is in active domain with relatively high oxidation rate. Then, with the generation of the passive film, the oxidation of the metal is effectively suppressed and the current decreases to a very low value and here it starts the passive domain. In this region, the corrosion rate of passive metals is much lower than active metals. When the potential is very high, it goes to transpassive domain where the current increases abruptly due to the dissolution of the passive film.
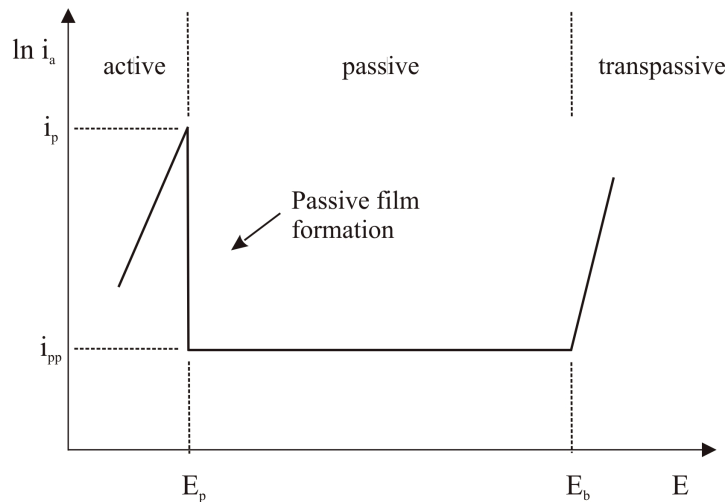
Figure 2.6 Typical anodic partial polarization curve of passive metals [31]

Electrochemical conditions are also known to critically affect the tribocorrosion behavior of metals. Guadalupe et al. [30] carried out CoCrMo alloy tribocorrosion experiments using a tribometer and found very different wear results at different applied potentials, as shown in Figure 2.7(a). A marked wear transition from cathodic to passive domain was found. This transition can be explained by the passive state reached by the CoCrMo alloy above the passive potential that generates wear accelerated corrosion and promotes mechanical wear by rendering the metal more prone to breakdown [24,30]. Indeed, suppressing passivity of CoCrMo alloys by nitrogen implantation eliminated the transition [32]. It has been found in many tribocorrosion studies that with

cathodic potential applied, wear accelerated corrosion is inhibited and the material degradation is mainly mechanical removal [29,30,33,34]. Also, it can be seen from Figure 2.7(a) that even in cathodic domain or passive domain, the wear varies at different potentials. This demonstrates the crucial role played by electrochemical conditions on wear of CoCrMo alloys. Mischler et al. [6] collected the tribocorrosion results of CoCrMo alloys in body-simulated solutions tested at different applied potentials and found a similar wear transition from low potentials to high potentials, as shown in Figure 2.7(b).

(a)   (b)
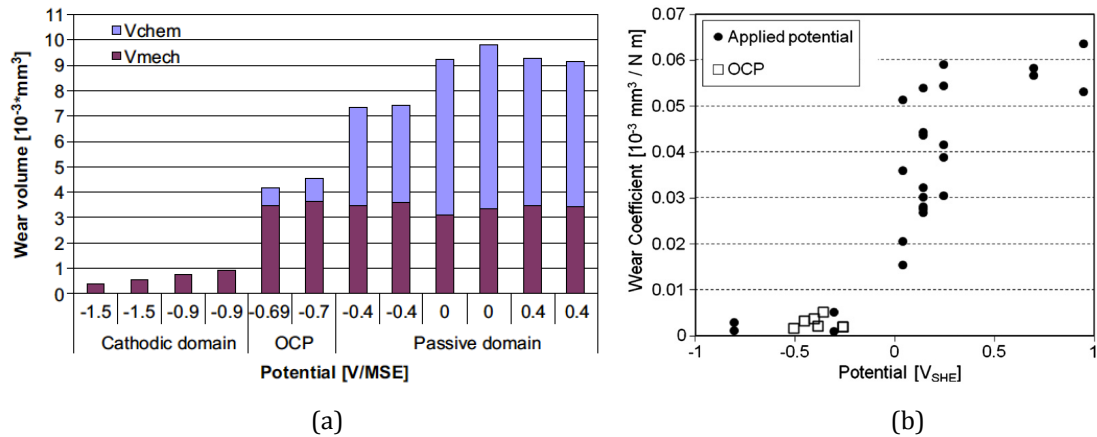
Figure 2.7 Plot of experimental wear as a function of the CoCrMo electrode potential established in the contact (figures extracted from[30] and [6])

Note that mechanical wear is also affected by the corrosion conditions and in particular by the presence of surface oxide films which may render the metal more brittle and prone to wear, or may act as lubricant [24]. Therefore, the synergism between wear and electrochemical corrosion is quite complex and the material loss caused by tribocorrosion is not simply the sum of wear in dry friction and corrosion taken separately.

2.2.3 Tribocorrosion modeling

Tribocorrosion has been the object of several studies aimed at elucidating the interaction mechanisms of wear and corrosion and at developing predictive models for describing material degradation induced by synergistic effects of wear and corrosion [25]. A general model was proposed by Uhlig [35] in 1954 for fretting corrosion based on two distinct mechanisms: mechanical wear and

wear accelerated corrosion. Then, Mischler et al. [24,26,31] applied the model to sliding tribocorrosion and further studied the interaction between mechanical wear and electrochemical corrosion. According to these studies, the total wear U_{tot} removed by tribocorrosion is given by Equation (2.1):

$$U_{tot} = U_{mech} + U_{chem} \tag{2.1}$$

where, U_{mech} is mechanical wear and U_{chem} is chemical wear. As shown in Figure 2.8, U_{mech} is the metal mechanically removed by the indenter and U_{chem} is the oxidized metal and can be further subdivided into two parts: the wear accelerated corrosion inside the wear track and the corrosion outside the wear track. Since the former one is normally much larger comparing to the latter one in a tribocorrosion system, only the wear accelerated corrosion is considered in the calculation of chemical wear.
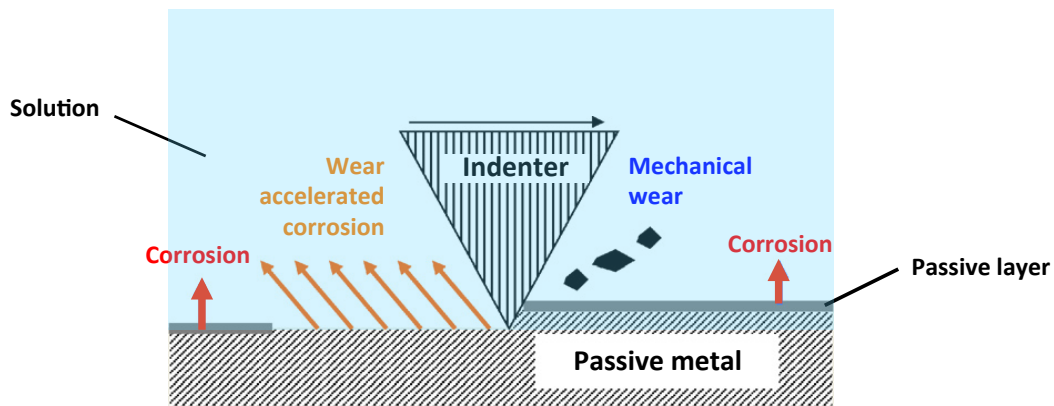
Figure 2.8 Schematic of the wear and corrosion in a tribocorrosion system [6]

Early mechanical wear formalisms were based on the assumption that wear volume is linearly proportional to the normal load (F_n) and sliding distance (L), as shown in Equation (2.2). L can be further split into sliding velocity (v_s) multiplying sliding time. k is the wear coefficient.

$$U = kF_n L = kF_n v_s t \tag{2.2}$$

These formalisms are consistent with Archard's theorem [36] implying a proportionality between wear and the real area of contact established at plastically deforming asperity junctions and the sliding distance. The real area of

contact is given by the ratio of normal load to indentation hardness, which modifies Equation (2.2) into Equation (2.3). H is the surface hardness.

$$U = k\left(\frac{F_n}{H}\right)L = k\left(\frac{F_n}{H}\right)v_s t \tag{2.3}$$

Such models are commonly used for their simplicity and wide validity, and predictions from such models were found to correlate well with experimental data obtained from dry friction tests [36].

Studies of wear accelerated corrosion of passive metals are usually carried out by imposing a passive electrode potential to the metal while rubbing against a counterpart. In this way, the acceleration of corrosion can be measured by recording the current necessary to maintain the passive potential. The excess current can be related to the material loss through Faraday's law [31]. Mischler et al. [26] and Landolt et al. [29] proposed a mechanistic approach which correlates the extent of current to the passivation charge density (Q_p) and the depassivation rate (R_{dep}), as shown in Equation (2.4).

$$I_p = R_{dep} \cdot Q_p \tag{2.4}$$

Q_p is the charge per surface area needed to form the passive film from the bare metal or reform the passive film when the passive film is removed. So, it represents the charge flow (corresponding to the amount of oxidized metal) during the depassivation and repassivation. Q_p can be determined by independent electrochemical experiments, e.g. the charge is measured by integrating the current density when switching the applied potential from cathodic to a given passive potential.

Based on this approach, several models [29] are available for describing the extent of anodic current as a consequence of plastic deformation induced by sliding at asperity contacts. These models predict a proportionality b between wear accelerated corrosion rate and the ratio of normal load to hardness at a power ranging from 0.5 (rough surface sliding against smooth counterpart) to 1 (both counterparts rough), and linear proportionality to the sliding velocity and the passivation charge density, as shown in Equation (2.5):

$$I_p = K v_s Q_p \left(\frac{F_n}{H}\right)^b \tag{2.5}$$

where, K is a proportionality factor including number of asperities in simultaneous contact and depassivation probability of the contacting surface elements.

Such models were found to accurately describe the tribocorrosion behavior of a CoCrMo alloy under idealized laboratory conditions (inert ceramic counterpart, sulfuric acid as model electrolyte, high contact pressure exceeding the plastic yield of the alloy, stroke frequency lower than a few Hz in order to allow sufficient time for repassivation between two strokes) [30].

2.3 Fluid lubrication

Fluid lubrication was studied from the late nineteenth century when hydrodynamic lubrication was found in gears and rolling contact bearings [37]. Lubrication has been found to influence the friction and wear properties of almost all materials in lubricated engineering applications. The effect of lubrication conditions on friction can be illustrated using Stribeck curve developed at the beginning of the twentieth century [38]. There are mainly three lubrication regimes in the Stribeck curve: boundary, mixed and hydrodynamic lubrication, as shown in Figure 2.9.
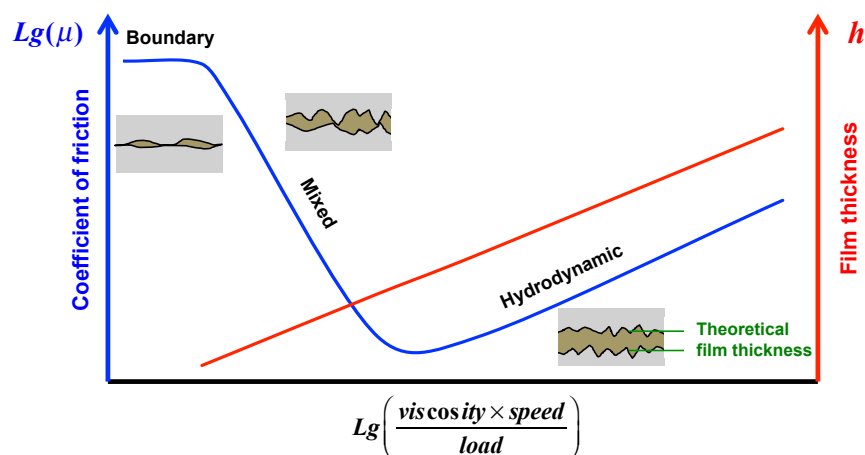
Figure 2.9 The influence of lubrication on friction (Stribeck curve)

Different regimes exhibit quite different friction properties. In boundary

lubrication regime, the counterparts are seldom separated and only very little lubricants are trapped inside. In this regime, the coefficient of friction is high because of the large solid-solid contact area. If the contact is further separated, there will be more lubricants inside the contact. In this regime, it is believed that between the two counterparts, due to the surface roughness, asperities are contacting and then deformed or making scratches on the plain surface of the counterpart. While between the asperities, the lubricants separate the contact. That is why it is called mixed lubrication. Due to the less and less asperity contacts, the direct contact of the counterparts decreases and thus friction is reduced. Finally, with the increase of the separation, the counterparts can be completely separated, which means the friction is only from the shear stress of the fluid film between the counterparts.

There is a theoretical method to estimate the lubrication regimes based on the λ ratio [8] defined as:

$$\lambda = \frac{h_{min}}{R_a{'}} \tag{2.6}$$

where, h_{min} corresponds to the minimum film thickness and $R_a{'}$ is the composite surface roughness of the two counterparts which can be calculated by $R_a{'}=(R_{a1}+R_{a2})^{0.5}$. If $\lambda < 1$, boundary lubrication occurs, while $\lambda > 3$ indicates hydrodynamic lubrication. When $1 < \lambda < 3$, mixed lubrication prevails. In many situations, λ ratio can only be used to approximately estimate the lubrication regime since the surface roughness is not easy to be determined for textured contact surfaces. For example, the wear surface after reciprocating sliding present roughness much higher perpendicular to the sliding direction than that in the sliding direction. Sometimes third bodies can increase locally the surface roughness. Typically, the minimum film thickness of MoM artificial hip joints varies from 0 to more than 50 nm, as shown in Figure 2.10. If surface roughness R_a = 10 nm is considered (this is the typical roughness of artificial hip joints), the λ ratio is from 0 to more than 3, which means MoM artificial hip joints operate under all of the three lubrication regimes because of the variation of load and velocity during gait.
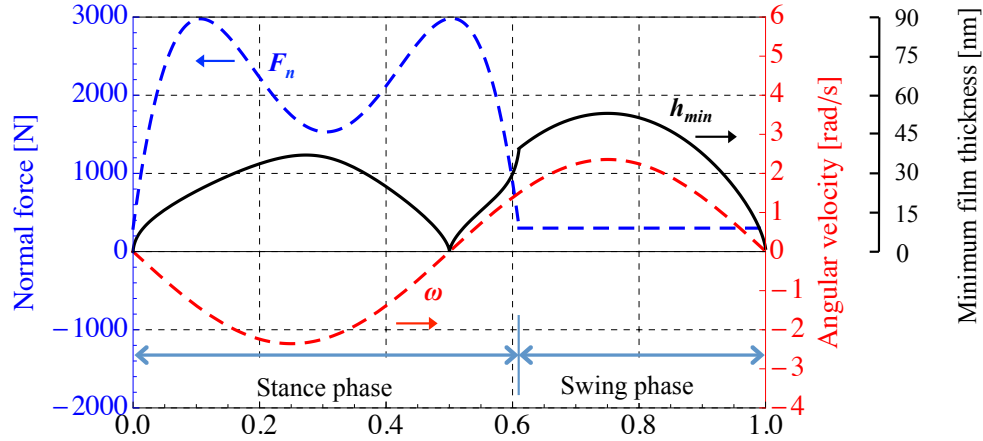
Figure 2.10 The variation of minimum film thickness in one gait cycle due to the variation of normal load and angular velocity according to ISO 14242-1 (head radius: 18 mm and radial clearance: 30 μm)

The minimum film thickness h_{min} can be calculated using the Hamrock-Dowson formula developed in 1978 [39].

$$h_{min} = 2.8 \left(\frac{u\eta}{E'R'}\right)^{0.65} \left(\frac{F_n}{E'R'^2}\right)^{-0.21} R' \qquad (2.7)$$

where, u is the entraining velocity, $u=(v_1+v_2)/2$, v_1 and v_2 are the sliding velocities of the two counterparts, respectively. η is the viscosity of solution, and F_n is the normal load. E' is the effective Young's modulus and R' is the effective radius of curvature, $1/R'=1/R_1+1/R_2$ (for convex surfaces), $1/R'=1/R_1-1/R_2$ (for concave surfaces). This formula is based on the Reynolds' theory which assumes that the fluid is Newtonian and has a perfect wettability on the contact surfaces [39]. The formula was widely used to predict the film thickness and estimate the lubrication regimes by λ ratio which is the minimum film thickness divided by surface roughness, as shown before.

Wear is also dramatically influenced by lubrication conditions. It is believed that wear is much more severe in boundary lubrication regime comparing to mixed and hydrodynamic lubrication. In mixed lubrication regimes, the total normal load is carried partially by asperity contacts and partially by the hydrodynamic fluid film. Increasing fluid film thickness reduces the load carried by asperities and thus it is supposed to reduce wear. As an example, Dowson [40] compared steady state wear rates from independent simulator experiments with

19

corresponding hydrodynamic film thicknesses calculated using Equation (2.7) and observed that very low wear rates (corresponding to wear coefficients in the range of 10^{-9} mm^3/Nm) were achieved when the film thickness exceeds 15-20 nm (Figure 2.11). Below this threshold, the wear rate increased by more than 2 orders of magnitude when decreasing film thickness from 15 to 5 nm. These data clearly show the importance of hydrodynamic lubrication to wear.
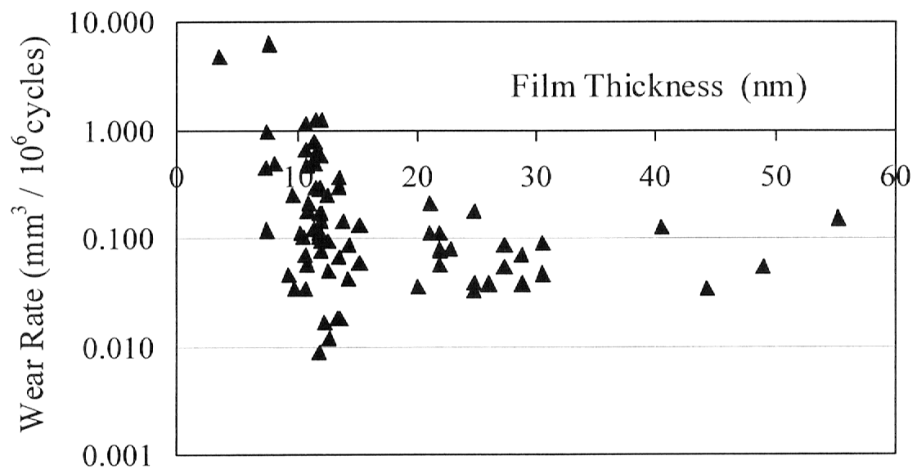
Figure 2.11 In-vitro wear rate of MoM artificial hip joints as a function of theoretical fluid film thickness [40]

For MoM hip joints, one usually observes two distinctive regimes in the simulator tests [41,42]. Initially, the femoral and acetabular components show a relatively rapid but decreasing wear rate over the first 0.5 to 2 million cycles in a hip joint simulator, or 0.5 to 2 years in vivo considering an average walking frequency of 1 Hz. This feature is generally attributed to a running-in process. Once this process has been completed, the rate of wear becomes steady and relatively low. These two distinctive regimes are shown in Figure 2.12. Clearly, the wear study of the running-in period is of great importance to evaluate the wear properties of MoM artificial hip joints since most of the wear is from the running-in period.
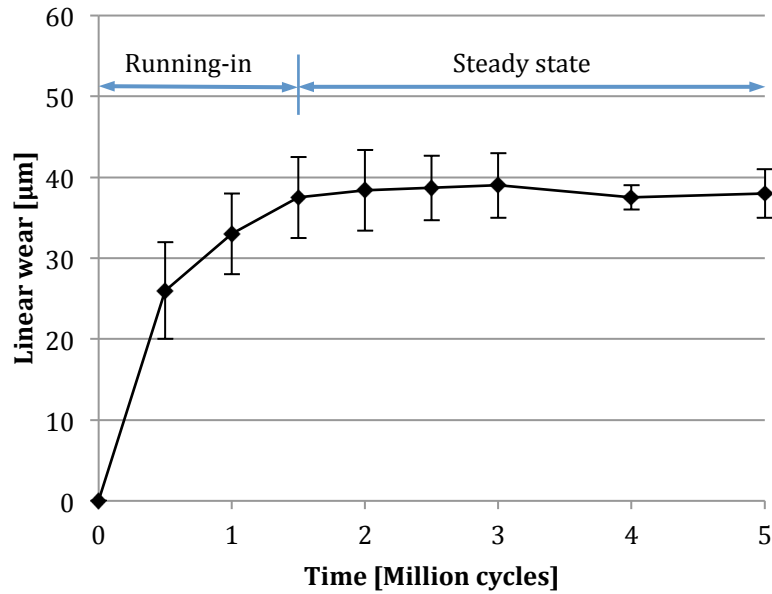
Figure 2.12 The evolution of linear wear with time of a self-mated MoM hip joint tested in hip joint simulator (CoCr alloy, head radius: 28 mm, radial clearance: 118.95 μm) [42]

Even the picture is clear that higher film thickness results in lower wear, no mechanistic model was developed to quantitatively describe this phenomenon. Indeed, Dowson [23] found out by comparing a large amount of experimental wear data from simulators (Figure 2.13) that the extent of both running-in and steady state wear are inversely proportional to the hydrodynamic fluid film thickness with different powers, which constitutes the only quantitative model correlating wear with lubrication parameters, as shown in Equation (2.8).

$$U = \left[\frac{93.97}{\left(h_{\min}(nm) \right)^{1.49}} + \frac{1.87}{\left(h_{\min}(nm) \right)^{1.02}} (n_t - n_r) \right] mm^3 \qquad (2.8)$$

where, U is the volumetric wear, n_r is the million loading cycles at the end of running-in period and n_t is the actual number of accomplished million cycles, respectively. h_{min} is the minimum film thickness as calculated using the Hamrock-Dowson film thickness equation (Equation (2.7)). The first term in the equation represents the running-in wear while the second term describes the steady-state wear. Apparently, this model is an empirical correlation based on hydrodynamic film thickness and doesn't consider material dependent parameters such as hardness and surface chemical reactions.

(a)

(b)
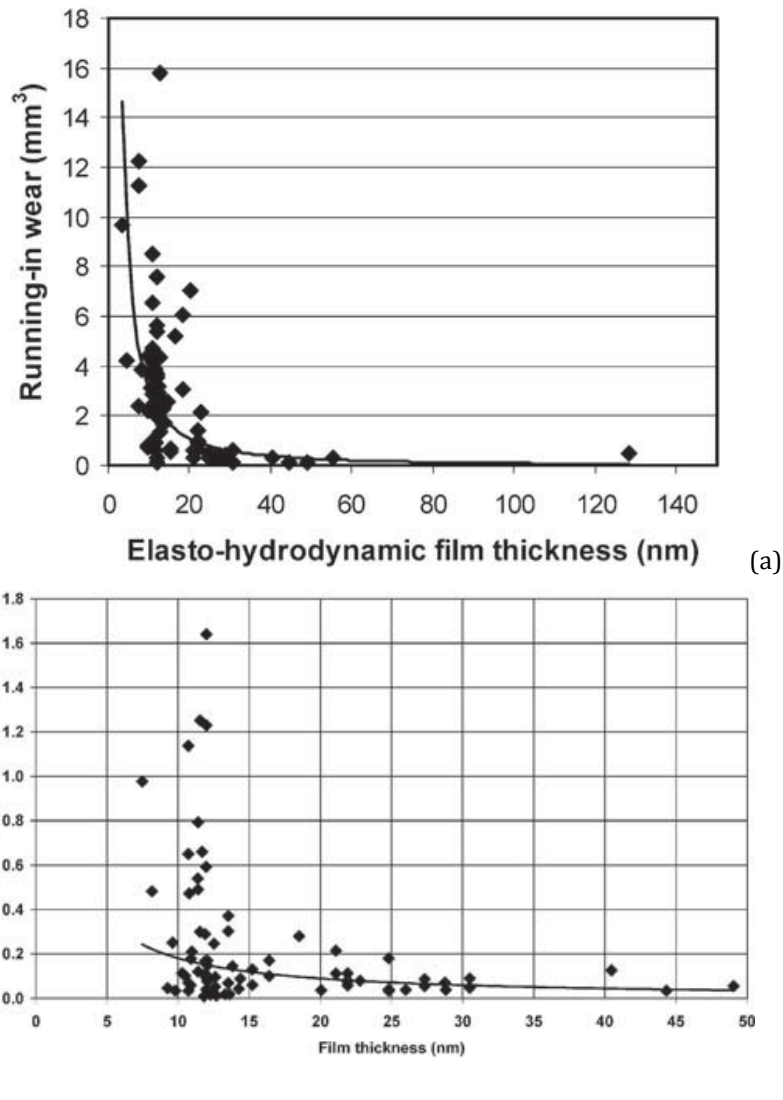
Figure 2.13 Experimental running-in wear (a) and steady state wear rate (b) at different hydrodynamic film thickness [23]

Considering the running-in wear correlation with the minimum film thickness, as shown in Equation (2.9), the considered experimental results have large scatterings as shown in Figure 2.14 which is a partial enlargement of the Figure 2.13(a).

$$U_{running-in} = \frac{93.97}{(h_{min})^{1.49}} \tag{2.9}$$
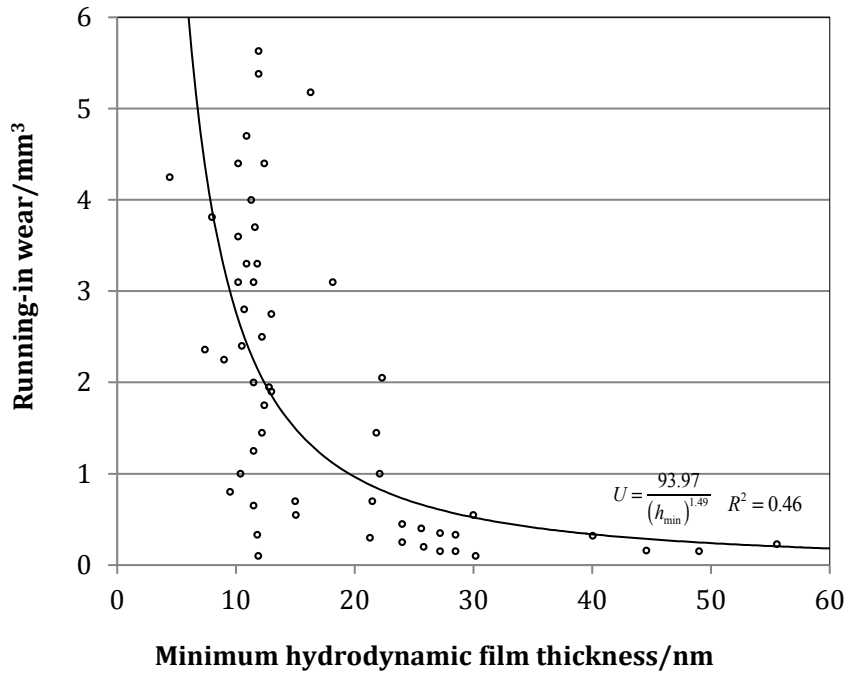
Figure 2.14 The partial enlarged view of Dowson's running-in wear and minimum hydrodynamic film thickness correlation derived from [23]

The reason for these scatterings can be from the variety of the experimental conditions and parameters in the hip joint simulator tests in the literature but only head radius and clearance values were considered as variables in the calculation of the minimum film thickness in Figure 2.14. The experimental results were from eight laboratories in the UK, Canada and USA, which means different kinds of simulators have been used possibly with different load curves and motions applied. Also, the lubricant used in simulators was calf serum solution but can be with different concentrations and different additives such as EDTA and NaN_3 that may affect the viscosity of the solution and influence the wear results. Different CoCrMo alloys were used, which results in different wear properties. In Dowson's study, he used average values for the normal load, angular velocity, Young's modulus, Possion's ratio as well as viscosity in the calculation of the minimum hydrodynamic film thickness. Considering these factors, it is not surprising to get a low coefficient in the correlation between wear and minimum film thickness. On the contrary, it should be considered as a good correlation under all these uncertainties.

2.4 Wear modeling of artificial hip joints

Some studies [43-47] implemented Archard's wear model into the numerical method to describe the wear evolution of artificial hip joints with time and wear distribution. In this method, Equation (2.2) is usually used in the form of linear wear with respect to the contact stress σ_s, as shown in Equation (2.10).

$$U_{linear} = k\sigma_s L \tag{2.10}$$

The real geometry of the implants, the physiological loading and motions were adopted and finite element method (FEM) is used to calculate the local wear at each node in the contact based on the corresponding local contact stress and displacement at each time step by assuming a certain wear coefficient k. This kind of modeling has been used more extensively for MoP hip implants since MoP prostheses are still the most implanted hip prosthesis and the polymer cups undergo significant wear [8]. Results of the wear rates from the simulations are found rather close to the clinical data.

Liu et al. [46] and Uddin et al. [47] used this numerical method to predict wear rate and wear distribution of MoM artificial hip joints. By applying wear coefficients for the running-in and steady state period obtained from simulator or pin-on-disk tribometer experiments, they predicted reasonable wear evolutions of MoM artificial hip joints with time and the simulation showed the complexity of contact stress distribution on the worn surfaces.

The numerical modeling provides a useful method to simulate the evolution of wear as well as the wear distribution on the bearing surface. However, the modeling is currently still only based on Archard's theorem. Wear coefficient k is an input parameter in the modeling that needs to be obtained from hip joint simulator or tribometer experiments. Equation (2.2) is based on a simplified vision of the wear process. The limited number of operational parameters considered in Archard's formalism does not allow to explain the effect of other factors such as the clearance that play a crucial role on wear of MoM hip joints [42]. It also ignores the effect of electrochemical components on total wear and the relevance of hydrodynamic lubrication by the synovial fluid [8,23,30].

As described in section 2.2, wear accelerated corrosion models have been developed and such models were found to predict quite well the chemical wear in the tribocorrosion of CoCrMo alloys carried out in tribometers. Moreover, Mischler et al. [6] tentatively applied the wear accelerated corrosion model to the MoM contact conditions and found the model predicted wear rates close to the values reported in literature for MoM hip joints tested in simulators. According to this study, wear accelerated corrosion is likely to account for a significant fraction of the overall MoM degradation in clinical relevant conditions.

Only few attempts were made to model wear under mixed lubrication. As decribed in section 2.3, the effect of elastohydrodynamic lubricating films on wear of MoM implants was addressed by Dowson [22,23]. However, no model was developed to quantitatively describe the lubrication effect on wear except Dowson's empirical correlation between wear and hydrodynamic film thickness.

Mechanical wear, corrosion and lubrication constitute the main aspects influencing the wear performance of MoM artificial hip joints. But clearly, there is not mechanistic model developed including all these aspects to quantitatively describe the wear of MoM artificial hip joints. Dedicated models exist to describe each aspect. The tribocorrosion model combines mechanical wear and electrochemical corrosion and has been used to predict wear rate observed in tribometer experiments [30]. To apply it to MoM artificial hip joints and incorporating the lubrication effect to develop a composite wear model for MoM artificial hip joints constitutes the main objective of this study.

2.5 Thesis objective

The literature review has shown that tribocorrosion and lubrication are crucial phenomena determining wear of MoM artificial hip joints. Consequently, modeling wear of MoM artificial hip joints should consider both of these two aspects. On one hand, wear accelerated corrosion has been mechanistically investigated and based on that and Archard's approach, tribocorrosion models have been developed. Elastohydrodynamic lubrication has been well studied and wear modeling of the running-in and steady state wear based on hydrodynamic

film thickness has been attempted and an empirical correlation between them is developed. On the other hand, the interaction between tribocorrosion and lubrication has never been investigated so far.

So the objective of this thesis is first to develop a composite wear model for MoM artificial hip joints, which considers the interaction between tribocorrosion and lubrication. As a second step, the model will be adapted to more general cases of tribocorrosion.

This goal will be achieved by firstly studying the available literature on tribocorrosion and lubrication and the models reported therein. Then, existing quantitative approaches will be combined in a composite model, which will be compared to available experimental results related to MoM hip joint prostheses. Finally, dedicated laboratory experiments will be conducted in order to provide a base for exploring model generalization.

Chapter 3 Model for running-in wear of MoM artificial hip joints

Based on the existing tribocorrosion and fluid lubrication models, the aim of this chapter is to develop a composite model that combines these two aspects. For the modeling, the plastic deformation of the contacting asperities is considered as the wear mechanism in lubricated tribocorrosion conditions. The fluid lubrication influences the extent of the plastic deformation by changing the fraction of the effective normal load to the total applied normal load. A composite wear model can be developed by replacing the total normal load by the effective normal load in the tribocorrosion model.

The model will be then calibrated using a well-controlled tribocorrosion experimental study carried out in a tribometer. The applicability of the model to CoCr alloys of different carbide concentrations will be assessed.

3.1 Modeling

Figure 3.1 illustrates the physical concept underlying the present attempt to model tribocorrosion in mixed lubrication as found in artificial hip joints. Direct contact between the two solid surfaces (Figure 3.1a) occurs only locally at asperity junctions (Figure 3.1b) or contacts between asperity and flat part of the counter body (Figure 3.1c). This is the real contact area between the counterparts and such contacts are supposed to behave plastically. Thus, when the two bodies move with respect to each other, at the contact spots, mechanical wear and wear accelerated corrosion occur as a consequence of plastic deformation.
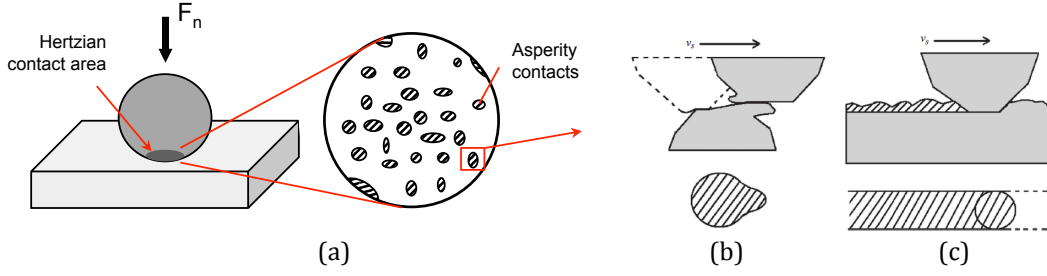
Figure 3.1 Schematics of the asperity contacts inside the nominal contact area (Dashed areas represent plastically deformed and then depassivated metal surface)

Mechanical wear can be described by the Archard's theorem relating the extent of wear to the real contact area established by plastic deformation at the contact spots. The sum of the contact areas of all spots A_{real} corresponds to the ratio between normal load F_n and surface hardness H and thus the wear rate can be described by Equation (3.1) that relates volumetric wear U_{mech} as a function of F_n, H and sliding distance L with k_m as proportionality factor:

$$U_{mech} = k_m \left(\frac{F_n}{H} \right) L \tag{3.1}$$

k_m is a proportionality factor which depends not only on material and deformation mechanisms (as the wear coefficient k does in Equation (2.3)) but also on the electrochemical conditions in tribocorrosion as shown by the different mechanical wear volumes obtained under cathodic and passive potentials (Figure 2.7a).

The wear rate can be defined by introducing in Equation (3.1) the average sliding velocity v_s according to Equation (3.2):

$$V_{mech} = k_m \left(\frac{F_n}{H} \right) v_s \tag{3.2}$$

In case of passive materials such as the CoCrMo alloys in body fluids, plastic deformation of asperities results in mechanical depassivation followed by repassivation once the depassivated surface contacts again the solution. The cyclic sequence of depassivation and repassivation leads to an enhancement of the corrosion rate (wear accelerated corrosion) that can be described using Equation (2.5). If the number of the contacting asperities is n_a, the average contacting area of each asperity $A_{i,ave}$ is A/n_a. When one part is sliding with

respect to the other, the depassivation rate of the surface is proportional to $v_s(A/n_a)^{0.5}$ which end up with the wear accelerated corrosion model described in [26] and [30]:

$$I_p = k_c Q_p v_s (F_n/H)^{0.5} \tag{3.3}$$

where, k_c is a proportionality factor depending on the fraction of the wear area becoming effectively depassivated and the number of the asperities.

Then, the chemical wear model can be obtained by combining the repassivation current model (Equation (3.3)) with Faraday's law:

$$V_{chem} = \frac{I_p M}{nF\rho} = \frac{k_c Q_p M v_s (F_n/H)^{0.5}}{nF\rho} \tag{3.4}$$

where, M is the atomic mass of the metal, n is oxidation valence, F is Faraday's constant (approximately 96,500 C/mol), and ρ is the density.

Equations (3.2) and (3.4) implicitly assume that the thickness of the hydrodynamic films is too small to provide any load bearing capacity and effective separation of the two contacting bodies. In the case of mixed lubricated contacts, as shown in Figure 3.2(a), the total normal force is carried not only by the contacting asperities but also by the hydrodynamic fluid film between the contacts. However, in this situation, only the load carried by the contacting asperities generates mechanical wear and wear accelerated corrosion. This fraction of the total normal force is called effective normal force F_{eff} and the extent of F_{eff} depends on one hand on the thickness of the hydrodynamic film and on the other hand on the surface roughness. It is clear that F_{eff} is the total normal load F_n in un-lubricated friction condition (Figure 3.2(b)) or equal to F_n if the fluid trapped inside the contact doesn't have any load capacity in boundary lubrication regime.

(a)   (b)
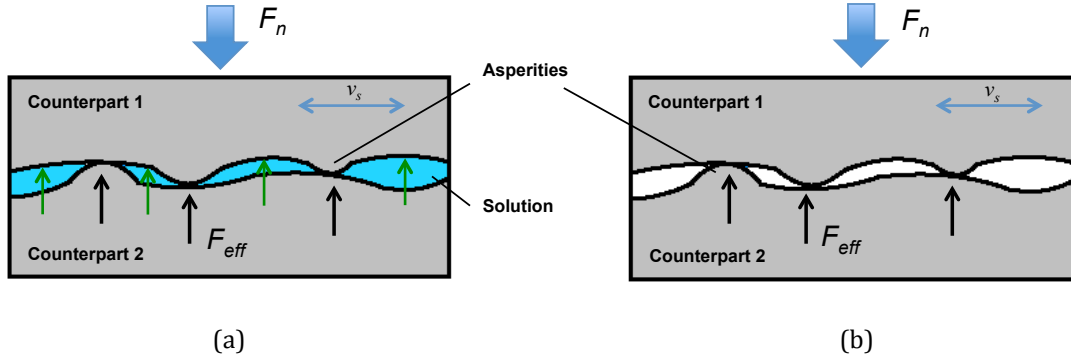
Figure 3.2 Schematics of the effective normal force in mixed lubricated (a) and un-lubricated (b) conditions

MoM hip joints operate mainly in mixed lubrication conditions and therefore part of the load is carried by the hydrodynamic fluid film and only a fraction of the total load generates wear. Dowson [23] identified an empirical correlation between a set of wear results obtained by testing a variety of CoCrMo MoM hip joints in simulators and the corresponding theoretical minimum hydrodynamic film thickness in the running-in period.

$$U_{running-in} = \frac{93.97}{(h_{min})^{1.49}} \qquad (3.5)$$

The empirical Equation 3.5 predicts lubricated wear being inversely proportional to the minimum hydrodynamic film thickness to the power of 1.49 for the situation of CoCrMo MoM hip joints characterized by specific mechanical alloy properties and polished surfaces with typical R_a values ranging from 0 to 50 nm. The wear reducing effect of hydrodynamic lubrication is ascribed to the reduction in load effectively carried by the contacting asperities [23]. Thus, the ratio between the load carried by asperity contacts (effective normal load F_{eff}) and the overall load applied to the contact (F_n) in mixed lubrication regime is inversely proportional to the film thickness at the power 1.49 as described by Equation (3.6).

$$F_{eff} = k_0 \frac{F_n}{(h_{min})^{1.49}} \qquad (3.6)$$

Introducing F_{eff} as the effective normal load responsible for wear and wear accelerated corrosion into Equations (3.2) and (3.4) yields a general equation for the tribocorrosion degradation in mixed lubrication regime:

$$V_{tot} = k_m \frac{k_0 F_n / h_{min}^{1.49}}{H} v_s + k_c \frac{Q_p M v_s}{nF\rho} \left(\frac{k_0 F_n / h_{min}^{1.49}}{H} \right)^{0.5} \tag{3.7}$$

An explicit composite model can be obtained by adding the minimum film thickness equation (Equation (2.7)):

$$V_{tot} = k_{mech} \frac{(E')^{0.6556}}{\eta^{0.9685}} \cdot \frac{(F_n)^{1.3129}(v_s)^{0.0315}}{(R')^{1.1473}H} + k_{chem} \frac{MQ_p(E')^{0.3278}}{nF\rho\eta^{0.4843}} \cdot \frac{(F_n)^{0.6565}(v_s)^{0.5158}}{(R')^{0.5737}H^{0.5}} \tag{3.8}$$

where, k_{mech} is the mechanical wear factor, $k_{mech} = k_m k_0/(2.8^{1.49})$, while k_{chem} is the chemical wear factor, $k_{chem} = k_c k_0^{0.5}/(2.8^{0.745})$.

3.2 Model calibration

A composite wear model for MoM artificial hip joints has been developed which combines tribocorrosion and lubrication aspects by introducing effective normal force to the tribocorrosion model. In order to use the model to predict the wear of MoM artificial hip joints, the factors k_{mech} and k_{chem} need to be calibrated.

Calibration of the model needs well-controlled experiments and appropriate measurement of the involved parameters. In particular, the characterization of the wear accelerated corrosion component requires the use of electrochemical techniques for measuring the corrosion rate during tests and controlling the prevailing electrode potential as one of the key factors affecting Q_p. While coupling electrochemical techniques with laboratory tribometers is currently a common operation [24], hip joint simulators do not provide routinely such measurements. The group at the University of Leeds is currently developing electrochemical set-ups to be applied to hip joint simulators.

Surface hardness is another import parameter since it directly affects both the mechanical and chemical wear. Increase of the outmost surface hardness from the bulk material has been widely found due to work hardening. Since the model is based on the plastic deformation of the surface asperities, the hardness of the outmost surface should be used, which means micro-hardness or nano-hardness is more representative to the surface hardness. However, for MoM artificial hip joints, only very few studies measured the hardness but mostly

using the macro-hardness.

Clearly, the lack of measurements of passivation charge density and surface micro-hardness in the simulator experiments induces the model impossible to be quantitatively calibrated using the MoM hip joint simulator results. For the time being, tribometer experiments appear as better appropriate methods for calibrating the model, in particular for determining k_{mech} and k_{chem} using tailored tribo-electrochemical experiments. So, the calibration of the model will be carried out using tribometer experimental results.

3.2.1 Determination of k_{mech} and k_{chem}

In ball-on-disk tribometer experiments, typically an inert ceramic ball (alumina) is rubbed against a metal plate immersed in the testing solution and kept under applied electrode potential using a potentiostat. During rubbing, the abrasive ball removes the passive oxide film from the metal surface, which results in larger corrosion rate that manifests itself in a higher current. At the end of rubbing, the metal passivates again and the current reaches again the pre-rubbing values. Out of the current enhancement, it is possible to determine using Faraday's law the chemical wear rate V_{chem}. The mechanical wear rate V_{mech} corresponds to the difference between the volume of the wear track on the disk divided by the rubbing duration and V_{chem}. The effective radius R' and the composite elastic modulus E' can be calculated by known geometrical and elastic properties. By knowing viscosity η, metal hardness H (ideally measured in the wear track after the experiments in order to take into account possible work hardening), normal force F_n, sliding velocity v_s and V_{mech}, one can calculate k_{mech} by the mathematical expression presented in Equation (3.8). Similarly, the k_{chem} value can be determined from the measured V_{chem}.

Guadalupe et al. [30] investigated the tribocorrosion of a biomedical high carbon CoCrMo alloy in 0.5 M sulfuric acid (H_2SO_4) with an inert alumina (Al_2O_3) ball sliding on the metal disk under different applied potentials and different loads. Details about the materials and experimental configuration can be found in [30]. The sliding was reciprocating with a dwell time of 0.25 s after each stroke in order to let the depassivated metal inside the wear track repassivate.

The total wear volumes were determined by multiplying the cross-section area taken perpendicularly to the sliding direction by the length of the wear track. The chemical wear volumes were determined by integrating the excess anodic current during rubbing and mechanical wear volumes were obtained by subtracting chemical wear volumes to the total wear volumes, respectively. The parameters used in the experiments are listed in Table 3.1.

Table 3.1 Tribocorrosion experimental parameters from [30]

Movement	Reciprocating sliding
Configuration	Ball (Al_2O_3, R=3 mm) on disk (CoCrMo alloy)
Normal forces/N	1.1, 5.8, 11.7, 17.5
Stroke length/mm	5
Frequency/Hz	1
Dwell time/s	0.25
Velocity/(mm/s)	20
Applied potentials/V_{SHE}	Passive: 0.254, 0.654, 1.054
Electrolyte (lubricant)	0.5 M H_2SO_4 solution
Testing time/s	1800

The passivation charge density was measured by independent electrochemical experiments for each of the investigated passive potentials using a potential step method. The sample was firstly cathodic cleaned at -1.5 V_{MSE} for 5 min and then the potential was switched to the desired passive potential. The current transients were recorded every 0.1 ms and the passivation charge density was calculated by integrating the current density from 0 to 0.5 s.

The hardness of the metal was measured using a Vickers micro hardness tester (Leitz) inside and outside the wear tracks. The applied load was 0.1 kg. Average values were calculated from three individual tests. The results revealed considerable work hardening due to friction and wear. Therefore, the hardness measured inside of the wear track was considered for calculation.

According to Equation (3.8), linear dependence of mechanical and chemical wear with the factors $F_n^{1.3129}/H$ and $Q_p F_n^{0.6565}/H^{0.5}$ are expected for the data from [30] and this is indeed observed in Figure 3.3, in particular for the chemical wear. Note that the experimental data are subject to some scattering partly related to uncertainties in the quantification of wear using profilometry and the

current [25,48].

(a)

(b)
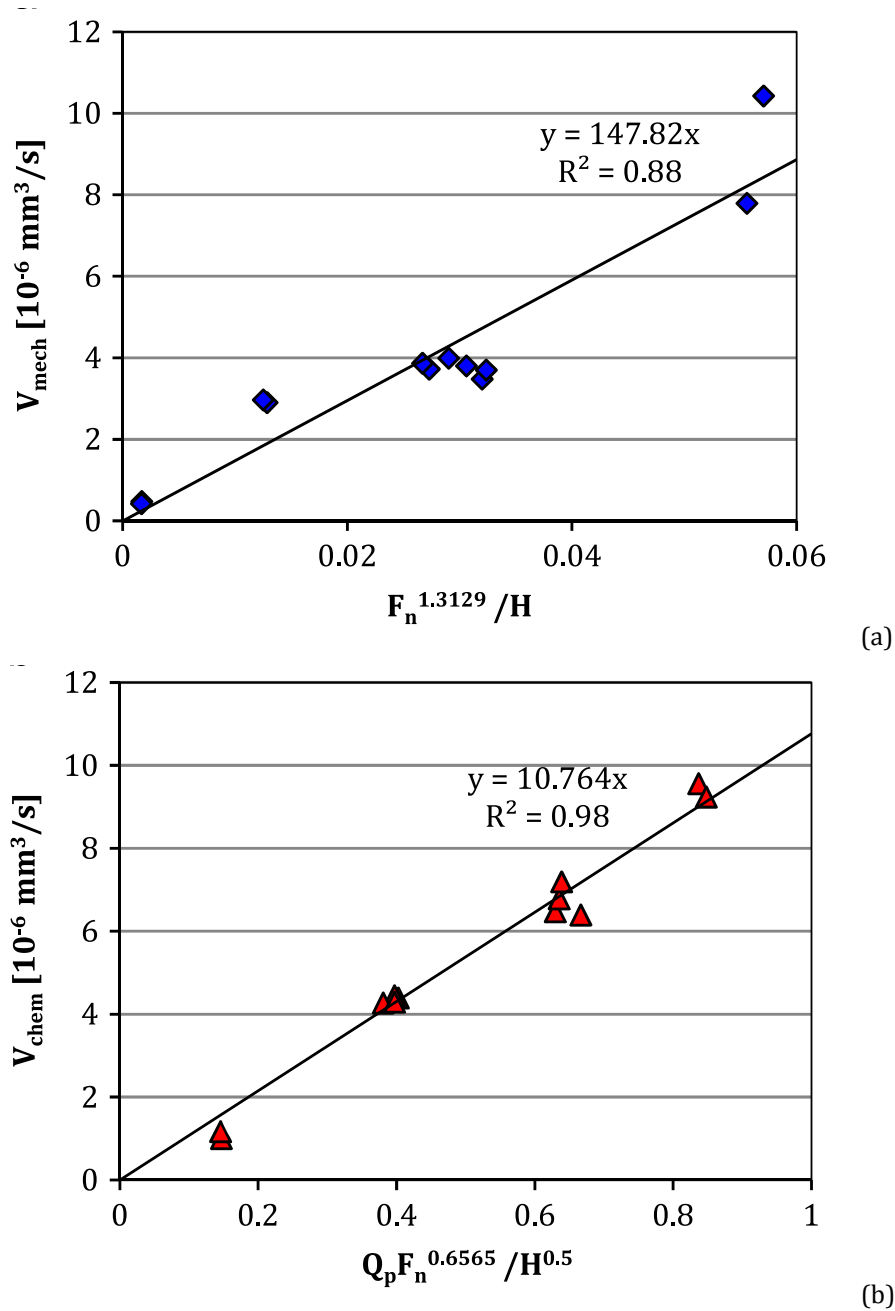
Figure 3.3 The correlation between mechanical (a) and chemical (b) wear rate extracted from [30] and the group of variables according to the composite model

The slopes of the correlation lines in Figure 3.3 allow one to extract the k_{mech} and k_{chem} values according to Equation (3.8) and the experimental parameters listed in Tables 3.1 and 3.2.

<div align="center">**Table 3.2** Constant values in the model calculation</div>

Materials	Al_2O_3: E= 350 GPa, v=0.22; CoCrMo: E= 248 GPa, v=0.3
0.5 M H_2SO_4 viscosity	$0.001\ Pa \cdot s$
Charge number (n)	2.37 (Co 2×63%, Cr 3×27% Mo 5×6%)
Molecular mass (M)	58.66 g/mol
Density (ρ)	8.33 g/cm³

By determining the proportionality factors for the mechanical wear rate k_{mech} and chemical wear rate k_{chem}, the composite model can thus be calibrated and described by Equation (3.9):

$$V_{tot} = 0.01363 \frac{(E')^{0.6556}}{\eta^{0.9685}} \cdot \frac{(F_n)^{1.3129}(v_s)^{0.0315}}{(R')^{1.1473}H}$$

$$+750.35 \frac{MQ_p(E')^{0.3278}}{nF\rho\eta^{0.4843}} \cdot \frac{(F_n)^{0.6565}(v_s)^{0.5158}}{(R')^{0.5737}H^{0.5}} \tag{3.9}$$

3.2.2 The material dependency of k_{mech} and k_{chem}

Strictly speaking, the model is calibrated for one type of CoCrMo alloys (high carbon content, wrought) and typical smooth surface of artificial hip joints and mirror polished tribometer samples (R_a: 0-50 nm), which is close to the assumption of perfect smooth surfaces in Hamrock-Dowson's theoretical minimum film thickness equation. For the using of the model, the factors k_{mech} and k_{chem} is system dependent and should be calibrated for each specific condition. Material is one of the factors influencing the values of k_{mech} and k_{chem}.

It should be noted that the presence of second hard phases such as carbides in several CoCr alloys, may also influence the plastic behavior of the metal and, by standing proud on the wear surface, influences the extent of metal asperity contacts [49], hence should also be considered as material factors influencing the wear of the metals.

To assess the applicability of the composite model to other CoCr alloys, tribocorrosion studies of three different CoCr alloys from the literature [50] will be used to compare with the model predictions.

Experimental description of the tribocorrosion studies from literature

Using the same tribometer and under the same experimental configurations as the ones described in the previous section, Guadalupe [50] did more tribocorrosion experiments for another two CoCr alloys. So, totally the tested three CoCr alloys (also known under the name of Stellites) were a Stellite 6 (S6) with 15% of carbides, a Stellite 21 (S21) with 5% of carbides and a Stellite 21 (LCS21) without carbides. The detailed compositions of the CoCr alloys are listed in Table 3.3.

Table 3.3 Nominal composition of CoCr alloys (S6, S21, LCS21) from [50]

Alloys	Weight percentage [wt. %]									
	Co	Cr	W	Mo	C	Ni	Fe	Si	Mn	B
CoCrW (S6)	Balance	27-32	4-6	-	0.9-1.4	3	3	2	1	-
CoCrMo (S21)	Balance	26-28	-	5-7	0.20-0.25	1	0.75	1	1	0.007
LC CoCrMo (LCS21)	Balance	28.8	-	5.68	0.01	0.32	0.24	-	-	-

The S6 alloy is composed of the traditional Co-Cr-W-C form and used in the nuclear industry for gripper latch arms [51]. It presents a hypoeutectic structure exhibiting a network of chromium rich carbides in the form of M_7C_3 and $M_{23}C_6$, the latter being the most commonly observed [52]. Depending on the manufacturing processes, it was also observed the formation of W-rich carbides [53].

The S21 alloys (CoCrMo alloys), commonly used in biomedical applications, are developed by replacing W with Mo in the composition of the S6 alloy. Its structure shows a Co-Cr matrix (with fcc and hcp phases) with dispersed (in grain boundaries as well as within the grains) Cr and Mo carbides. Replacement of W with Mo was observed to result in changes on the carbides morphology and increased volume fraction of carbides in the microstructure [54]. The main difference between the high carbon (>0.15 wt.%) and low carbon alloys is the presence of chromium carbides that on one hand increases hardness but on the other hand affects corrosion stability. The effect of carbides on wear is complex and depends on their nature, cohesion with the matrix, reactivity and distribution [55].

The experimental parameters of the S21 have been described in the previous section to calibrate the model. The applied loads for S6 were 5.8 N, 11.7

N and 17.5 N and the applied potential was 0 V_{MSE} only. The applied loads for LCS21 were 5.8 N and 11.7 N and the applied potential was 0 V_{MSE}. Other details of the parameters can be found in [50].

Correlations between wear rates and variables

The obtained mechanical wear rate (V_{mech}) values were plotted in Figure 3.4 versus the factors $(E')^{0.6556}F_n^{1.3129}/H$ (last part in the right side of Equation (3.10)) that contains all material and test specific variables. The correlation line of the S21 was plotted and the intercept was set as 0.

$$V_{mech} = k_{mech} \frac{(v_s)^{0.0315}}{\eta^{0.9685}(R')^{1.1473}} \cdot \frac{(E')^{0.6556}(F_n)^{1.3129}}{H} \tag{3.10}$$
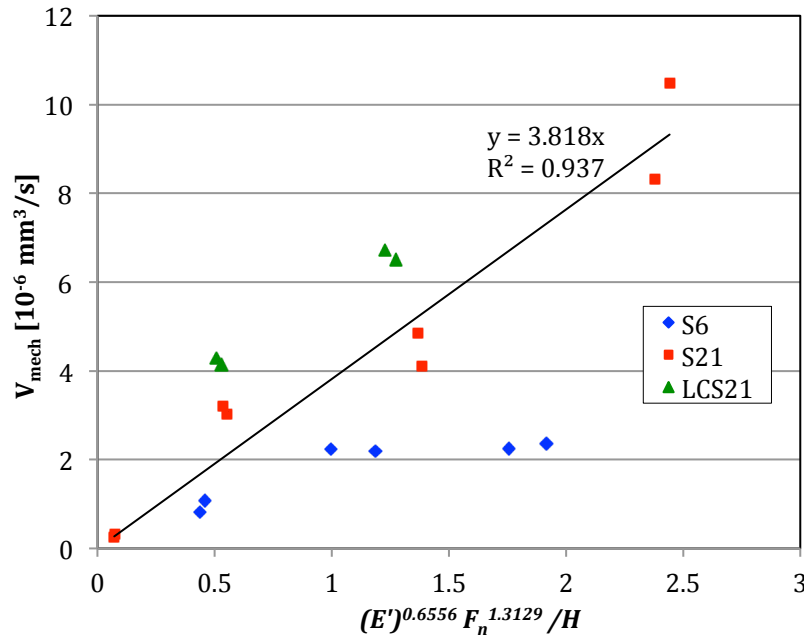
Figure 3.4 The correlation between mechanical wear rate and the experimental variables for different CoCr alloys

The correlation between the chemical wear rate and the factors $MQ_p(E')^{0.3278}F_n^{0.6565}/n\rho H^{0.5}$ (last part in the right side of Equation (3.11)) are shown in Figure 3.5.

$$V_{chem} = k_{chem} \frac{(v_s)^{0.5158}}{F\eta^{0.4843}(R')^{0.5737}} \cdot \frac{MQ_p(E')^{0.3278}(F_n)^{0.6565}}{n\rho H^{0.5}} \tag{3.11}$$
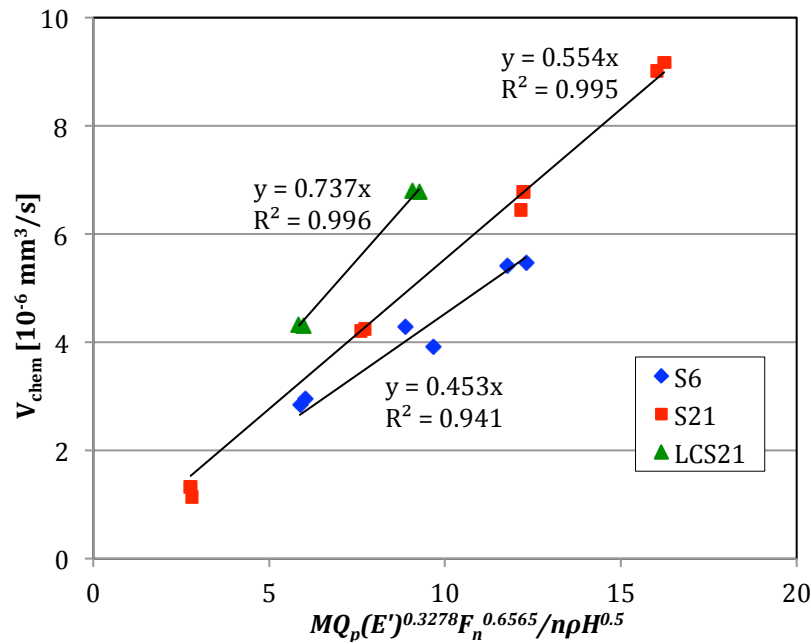
Figure 3.5 The correlation between chemical wear rate and the experimental variables for different CoCr alloys

According to the composite model, one would expect linear correlation between mechanical and chemical wear rates and the variable group. It can be seen from Figure 3.5 that all of the CoCr alloys showed good correlation between the chemical wear rate and variables from the tribocorrosion study, which is in agreement with the composite model. The three alloys exhibit different slopes and thus, according to Equation (3.11), different chemical wear proportionality factors k_{chem}.

For the mechanical wear, it can be seen that the scattering is larger than the chemical wear due to the method to determine mechanical wear (total wear divided by chemical wear), which accumulate the experimental errors from the total wear to the chemical wear. Figure 3.4 shows a good linear correlation in the case of S21. However, the correlation is less evident in the case of LCS21 alloy probably because of the limited number of available experimental data points.

The high carbide content S6 alloy seems not following the model predicted linear behavior but instead exhibiting a plateau with the increase of the applied normal load. The deviation of the experimental results from the model predictions is most likely related to the different wear mechanisms acting in the contacts that will be discussed later.

From these results, it can be seen that clearly the CoCr alloys with different carbide concentrations present different k_{mech} and k_{chem} values. The low carbon S21 showed highest slopes followed by the high carbon S21, which means under the same condition, the mechanical and chemical wear rates of low carbon S21 are the highest comparing to the other two alloys. Despite the non-linear correlation found in the mechanical wear rate, S6 showed the lowest mechanical and chemical wear rates. The above points clearly verify the material dependency of these two factors and thus these two factors should be calibrated for specific materials before applying the model to predict the wear rates.

3.3 Discussion

The proposed model is based on a simple mechanistic interpretation of tribocorrosion and lubrication. It combines the two aspects involved in the wear of MoM artificial hip joints and relates wear to material, mechanical, electrochemical and physical parameters. The proportionality factors k_{mech} and k_{chem} are system specific and require appropriate experimental calibration.

The present model suffers of some limitations linked to the empirical nature of Equation (3.5) that relates wear in the running-in period to the hydrodynamic film thickness. This equation is issued from a set of experimental wear investigations of CoCrMo MoM hip joints and is therefore specific to the conditions found there, in particular the surface roughness characterized by R_a values of typically a few ten nanometres, i.e. satisfying the condition for mixed lubrication for the typical hydrodynamic film thickness established in artificial hip joints. For smoother or rougher surfaces, the applicability of Dowson's equation needs to be verified. Indeed, Stemp et al. [56] observed that during tribocorrosion of stainless steel, the extent of mechanical and chemical wear was significantly affected by the roughness of the counterpart.

As another limitation, the model ignores time dependent effects. As a consequence of wear, the asperity height and thus the surface roughness are expected to steadily decrease with sliding time. This implies that a larger fraction of the load is progressively carried by the hydrodynamic film to the detriment of the load transmitted by asperities contacts. The wear rate should

correspondingly decrease with time. This is indeed observed in hip joint simulators where, after an initial high wear phase (running-in period), the wear rate becomes smaller and even negligible (steady state period). The build up of third bodies during rubbing also affects the load carried by asperities. In artificial hip joints, the formation of carbonaceous tribolayer [5] and the deposition of agglomerated proteins [57] have been reported. These phenomena are expected to reduce the asperity load and thus wear.

For quantitative predictions, the model requires calibration of the k_{mech} and k_{chem} factors as well as the input of specific parameters such as passivation charge density and surface hardness.

The passivation charge density is a crucial parameter affecting chemical wear. The correct input of the passivation charge density requires the knowledge of the electrode potential of the contacting metal, a value that need to be experimentally determined for each combination of metal and electrolyte as well as other critical parameters affecting the potential such as temperature and mass transport conditions in the fluid. Furthermore, the potential may change during tribocorrosion tests [6,30]. Chemical species present in the electrolyte may also modify the passivation charge density. For example, chelating agents such as lactic acid and phosphate ions were found to modify the passivation mechanisms and thus the passivation charge density of tungsten in acidic media [58]. Note also that the measurement of the passivation charge density is not trivial and the determined values may vary depending on the method used for measuring it [26]. So, the same method used for calibration should be used to determine the Q_p in the system under investigation.

During rubbing, metals usually undergo work hardening resulting in a hardness gradient from the surface to the bulk material [21]. The degree of hardening being difficult to predict, experimental determination of hardness is needed. The presence of the gradient implies that the measured hardness changes with indentation load. Thus, the same indentation load applied for calibration (0.1 kg) is recommended for measuring the micro hardness of the investigated wear surface.

The composite model was developed based on the wear mechanism of plastic deformation of the contacting asperities. In the present case (CoCrMo

alloys, aqueous solutions), the use of a simple laboratory tribo-electrochemical set-up consisting of a smooth alumina ball sliding against a polished CoCrMo flat surface appears as a suitable and simple method. Note that plastic deformation dominates the metal response to friction in the calibration system [30], which thus satisfy the underlying hypothesis of the model, i.e. plastic deformation at asperity contacts.

Systems involving other wear mechanisms may not be appropriate for calibration. This can be the reason causing the inconsistent mechanical wear rates of S6 in Figure 3.4 with the model predictions. Figure 3.6 shows SEM images taken in the center of the wear tracks on the three CoCr samples from [50]. Generally, all surfaces appear quite smooth along the rubbing direction (left to right) with some local structures such as debris, stripes and de-bonding.

The S21 and LCS21 clearly exhibit extensive plastic deformation, characterized by ploughing, smearing and formation of flake-like-tongues. This wear mechanism is also evidenced by the recrystallization process characterized by focused ion beam (FIB) cross section SEM images, as shown in Figure 3.7. The initial micro-grain structure of the S21 and LCS21 alloys is completely lost and replaced by a nano-grain refined surface zone (down to a depth of approximately 5 μm) below which the metal is highly deformed as indicated by extensive twinning. The most plausible wear mechanism of the S21 and LCS21 is cyclic strain accumulation (ratcheting) resulting in breaking of ridges extruded from the nanocrystalline layer. The composite wear model is based on the Archard's approach describing particle detachment as a consequence of plastic deformation. The mechanical wear behavior and the observed wear mechanisms are therefore consistent with the model predictions.
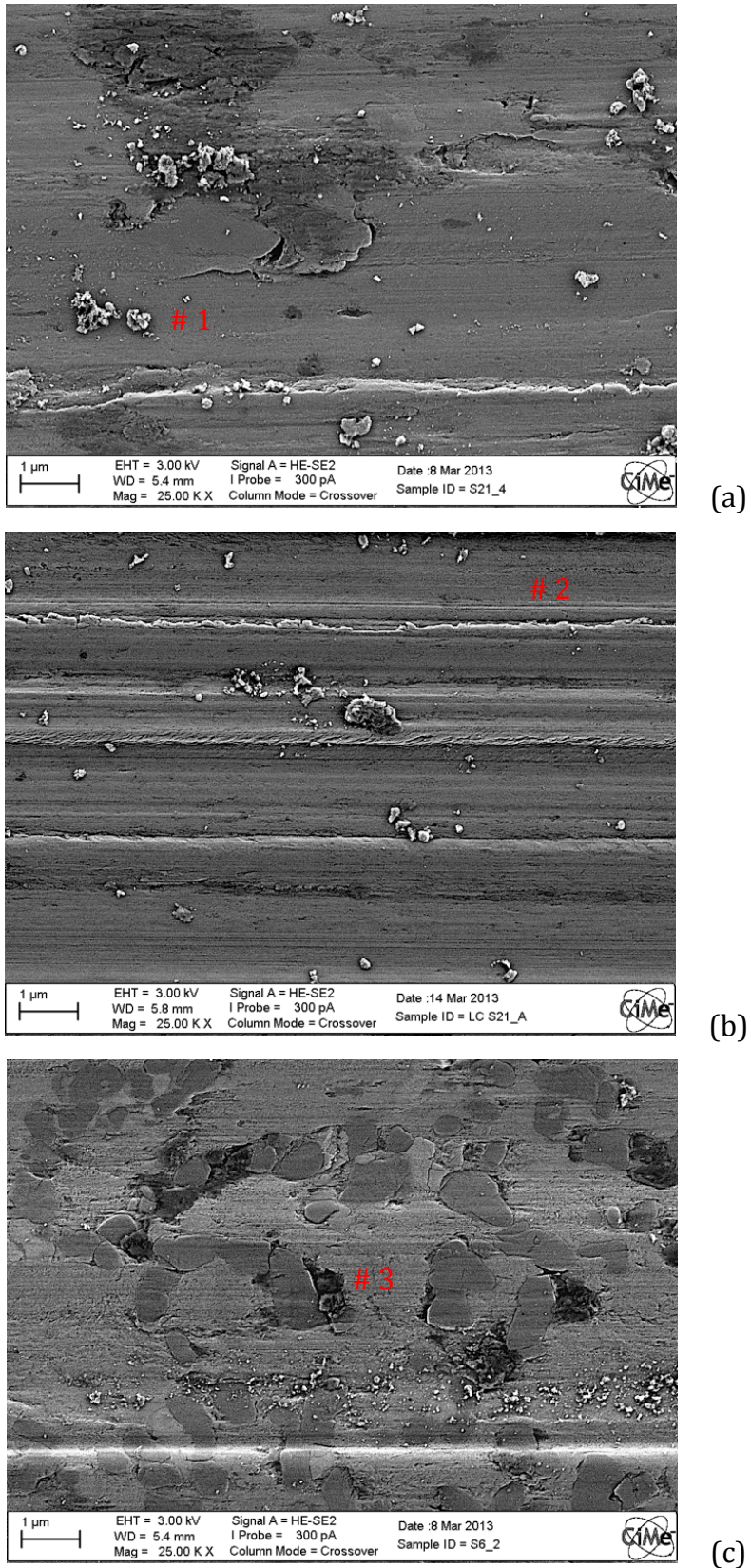
Figure 3.6 SEM image of the wear tracks at 0 V$_{MSE}$ and 11.7 N for: (a) S21 alloy, (b) LCS21 alloy, (c) S6 alloy. #1 agglomerated debris, #2 stripes, #3 carbide de-bonding. Images from [50].

<table>
<tr><td>(a)</td><td>(b)</td></tr>
</table>
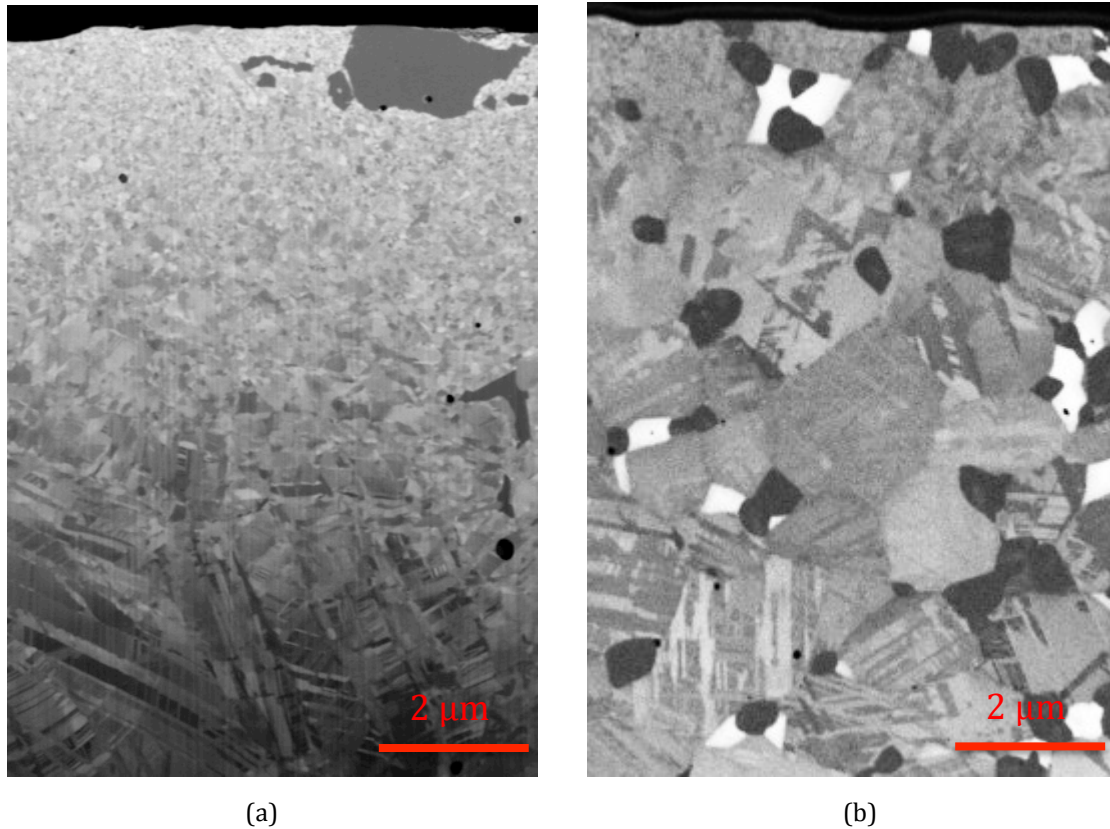
Figure 3.7 FIB transversal cross-section images from [50]: (a) S21 and (b) S6, cross sections are taken perpendicular to the rubbing direction

For S6, the carbides can be clearly identified through the darker color in the SEM images in Figure 3.6(c) and darker and white part in Figure 3.7(b). The carbides are apparently polished at the same height as the matrix. Some de-bonding of the carbides can locally be observed. The S6 exhibits a smooth worn surface without evident appearance of plastic flow. This is also confirmed by the subsurface deformation as shown in Figure 3.7(b). The accumulated strain in the S6 alloy is much smaller and the nano-grain refined layer is only 1 μm thick. Below this depth, the initial grain structure is broadly maintained, indicating less plastic strain. Most likely, the S6 carbides limit plastic deformation of the surrounding matrix by carrying out a significant part of the load. Consequently, the wear behavior of the carbides bearing alloy is supposed to be more complex as the mechanisms may differ between the hard ceramic reinforcements (brittle behavior) and the softer metal matrix (plastic behavior). Further, the two mechanisms may limit each other since the carbides appear in the worn surface at the same height as the surrounding matrix. According to this, wear may

proceed by repeated local sequences of wear of softer matrix followed by wear of the ceramic phase. This situation can hardly be described simply by the Archard's approach and thus the model does not apply.

3.4 Conclusion

Based on the plastic deformation of the contacting asperities, a composite wear model is developed, which combines mechanical wear, electrochemical corrosion and lubrication aspects, to quantitatively describe the degradation of passive metals.

The model is successfully calibrated for a CoCrMo alloy using a well-controlled tribocorrosion study carried out in a dedicated tribometer from the literature.

The material dependency of k_{mech} and k_{chem} is verified by the different slopes obtained from three CoCr alloys and the applicability of the model to different CoCr alloys is validated provided plastic deformation is the prevailing wear mechanism.

In general, the model is valid under the wear mechanism of plastic deformation of the contacting asperities, thus wear under other mechanisms may not follow the model.

Chapter 4   Comparison between model predictions and experimental results

In the previous chapter, a composite wear model for MoM artificial hip joints has been developed which combines tribocorrosion and lubrication aspects. The model could not be calibrated using MoM hip joint simulator results because passivation charge density and surface micro-hardness have not been reported in the simulator experimental studies. Tribometer experimental studies were found measured these values, thus a well-controlled tribometer experimental study of a CoCrMo alloy was used to calibrate the model.

The composite model involves a number of material, mechanical, electrochemical and physical parameters that are seldom fully reported in tribocorrosion studies. Clearly, the lack of the values for the essential parameters limits the applicability of the model. Especially, passivation charge density is often been omitted since independent electrochemical experiments are needed to measure the passivation charge density.

So, in this chapter, a systematic study of passivation charge density of a CoCrMo alloy will be carried out to check the dependency of passivation charge density on potential and solution. Then, the model will be used to predict the wear rates and compared with experimental results from two typical studies carried out in tribometer simulator conditions.

4.1 Determining passivation charge density

Passivation charge density (Q_p) is the charge needed to form the passive film from a unite bare metal surface or reform the passive film when the passive film is abraded. So, it represents the charge flow during the depassivation and repassivation. Q_p can be determined in independent potential step experiments where an electrode of the investigated metal is firstly polarized at a cathodic potential in order to remove any oxide film on the surface and afterwards rapidly polarized at the selected passive potential while recording the current transient.

Q_p corresponds to the integral of the current transient from the time 0 (application of the passive potential) up to the time corresponding to the time between two successive strokes in the tribocorrosion tests. Measuring passivation kinetics and charge densities is a heavy procedure that requires paying attention to electrode size, electrode configuration and electrolyte conductivity among other factors [26,59]. This method is based on two assumptions: firstly, the cathodic partial current should be negligible in order to make the measured current equal to the metal oxidation current. This is usually fulfilled for anodic polarization in the passive domain [29]. Secondly, the oxide film should be removed under the cathodic potential. This is not always fulfilled depending on materials, solutions and the time for cathodic cleaning. For example, Bardwell et al. [60,61] found that the oxide film of iron and iron-chromium alloys can be removed by cathodic polarization in acidic solutions but not so efficiently in neutral solutions.

For CoCrMo alloy, the passivation charge density was measured using the potential step method only in two studies. As introduced in the previous chapter, Guadalupe et al. [30] measured the passivation charge density of a high carbon CoCrMo alloy in 0.5 M H_2SO_4 solution at three different potentials. Hodgson et al. [62] studied the passive behavior of a low carbon CoCrMo alloy in buffered 0.14 M NaCl and measured the passivation charge density under two applied potentials. With these experimental data, the passivation charge densities at potentials other than these five values are still unknown. For this, a systematic passivation charge density measurement of a CoCrMo alloy in three different solutions was done in order to obtain passivation charge density at a wider range of applied potentials and in different solutions.

4.1.1 Experimental

The CoCrMo alloy (low carbon, the carbon content is approximately 0.05 wt.%) samples were cut from a bar into discs of 24 mm in diameter and with a thickness of 5 mm. Then the samples were polished in water using SiC emery papers (from Presi) from 500-mesh up to 4000-mesh. Final polishing was performed in order to get mirror-like surfaces using a diamond suspension

(from Presi), which is an ethanol-based solution with diamond particles (0.25 μm in diameter) inside. Finally, the polished samples were ultrasonically cleaned in ethanol and acetone for 5 minutes respectively and dried with oil free compressed air.

Then, the cleaned sample is fixed into a sample holder made of PMMA, as shown in Figure 4.1. Only a small circular area with 10 mm in diameter is left exposed to the solution and the other side of the sample is connected to a wire that is then connected to the potentiostat.
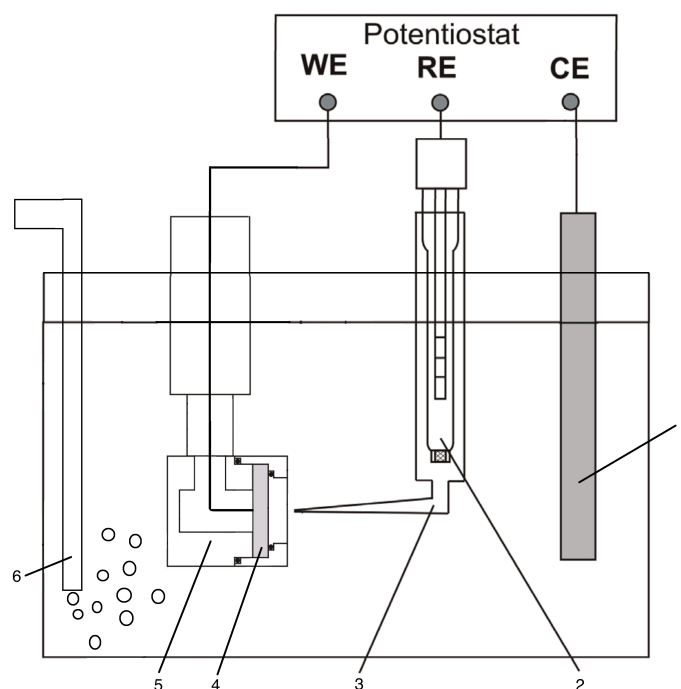
Figure 4.1 Schematic of the set-up for passivation charge measurement (1. counter electrode, 2. reference electrode, 3. Luggin capillary, 4. sample – working electrode, 5. sample holder, 6. Ar gas)

The working electrode is then placed in a sealed cell as shown in Figure 4.1 together with the counter electrode and reference electrode. The counter electrode is a platinum coil and the reference electrode is a standard mercury sulfate electrode (MSE) (0.654 V with respect to the potential of standard hydrogen electrode (SHE)) for H_2SO_4 solution and a standard Ag/AgCl (3M KCl) reference electrode (0.21 V with respect to SHE) for NaCl and calf serum solutions. The concentration for the H_2SO_4 and NaCl is 0.5 M and 9 g/L, respectively. The calf serum solution was prepared using commercial newborn

calf serum (from Thermo Fisher Scientific) and according to the specification, the protein content is 62 g/L. The pure calf serum was diluted using 9 g/L NaCl solution to get a final protein content of 30 g/L according to the ISO 14242-1. EDTA and Trometamol were added with a concentration of 0.2 g/L and 27 g/L respectively. Finally, the pH was adjusted using HCl to get a final pH of 7.6.

After the three-electrode cell is mounted and sealed, the solution was deaerated by passing Ar gas for 20 min. This is used to remove the dissolved oxygen in the solution in order to avoid the contribution of oxygen reaction to the excess anodic current. Then, the potentiostat was controlled by the LabVIEW software to apply a cathodic potential of -1.5 V_{MSE} for 1 minute and after that the potential was switched to a desired passive potential for 5 s. The imposed potential and the corresponding current values were measured at a frequency of 10 kHz i.e. every 0.1 ms. Throughout this procedure, the solution was deaerated by passing Ar gas. After each test, the sample was changed by a newly polished one to repeat the measurement. The tests were performed two times for each solution at each potential to check the reproducibility. Polarization curves in each solution were carried out in order to determine the passive domain and choose passive potentials for the passivation charge density measurements.

Once the current transient is obtained, the passivation charge density was calculated by integrating the current density from time 0 to 0.5 s. The time 0 is the switching point of the potential, which is also the jumping point of the current from negative to positive.

4.1.2 Current transient from the passivation measurement

Figure 4.2 shows the current transients (from time 0 to 0.5 s) from the potential step measurements in the 0.5 M H_2SO_4 solution at different applied passive potentials. The curves were found very similar to the one described in Figure 2.5(a). When the potential was switched from a cathodic potential to the passive potential, the measured current jumped from a negative value to a high positive value, which shows the oxidation of metal elements in the alloy. Then the current decreases quickly to a low value (less than 1 mA/cm²). This shows clearly the passivation of the investigated CoCrMo alloy.
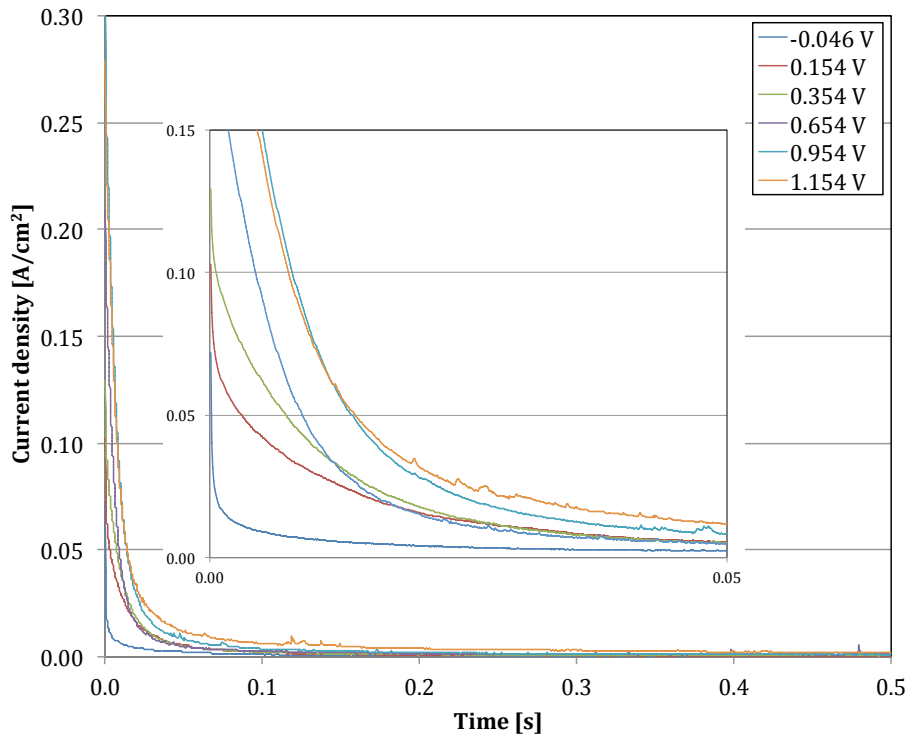
Figure 4.2 Current transients of the CoCrMo alloy from potential step tests in 0.5 M H_2SO_4 solution at different potentials (in linear scale, the plot in the middle is a partial enlargement of the transients from 0 to 0.05 s)

The current transient curves in logarithmic scale are shown in Figure 4.3. All the curves show clearly an initial plateau followed by a decreasing part, which corresponds well to the previous studies and the model developed by Jemmely et al. [59]. The initial plateau is due to the ohmic resistance of the electrolyte and the decreasing part is the growth of the passive film [59]. The average current in the plateau is clearly increasing with the increase of the applied potential. This is because in this part the oxidation of the metal is ohmic resistance dominated, thus at the same ohmic resistance of the electrolyte, the current is proportional to the applied potential.

49
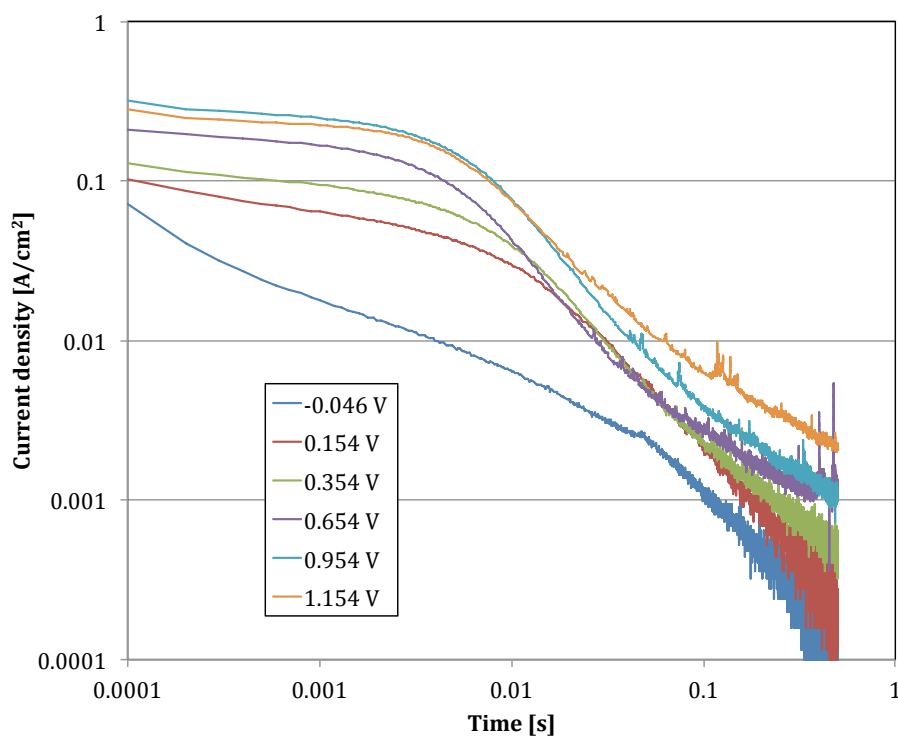
Figure 4.3 Current transients of the CoCrMo alloy from potential step tests in 0.5 M H_2SO_4 solution at different potentials (in logarithmic scale)

It is very interesting to see the difference between the current transient curves in different solutions at the same potential, as shown in Figure 4.4. Similar Plateaus and decreasing parts of the current were found for the three curves. However, differences in the details can be observed. Firstly, the current in the plateau is different, H_2SO_4 has the highest followed by calf serum and NaCl has the lowest current. As described previously, the current in the plateau is ohmic resistance dependent and the observed currents correspond very well to the conductivity of the solutions as measured using a conductivity meter (H_2SO_4: 191 mS/cm, NaCl: 14 mS/cm and calf serum: 28 mS/cm). Secondly, the duration of the plateau is slightly different for the three solutions. Higher current in the plateau tends to have shorter duration. Finally, the slope for the decreasing part is different. H_2SO_4 has the highest slope and NaCl has the lowest, calf serum being between them. This clearly shows the passivation rate for the three solutions is different. Again, higher current in the plateau tends to have bigger slope in the decreasing part.
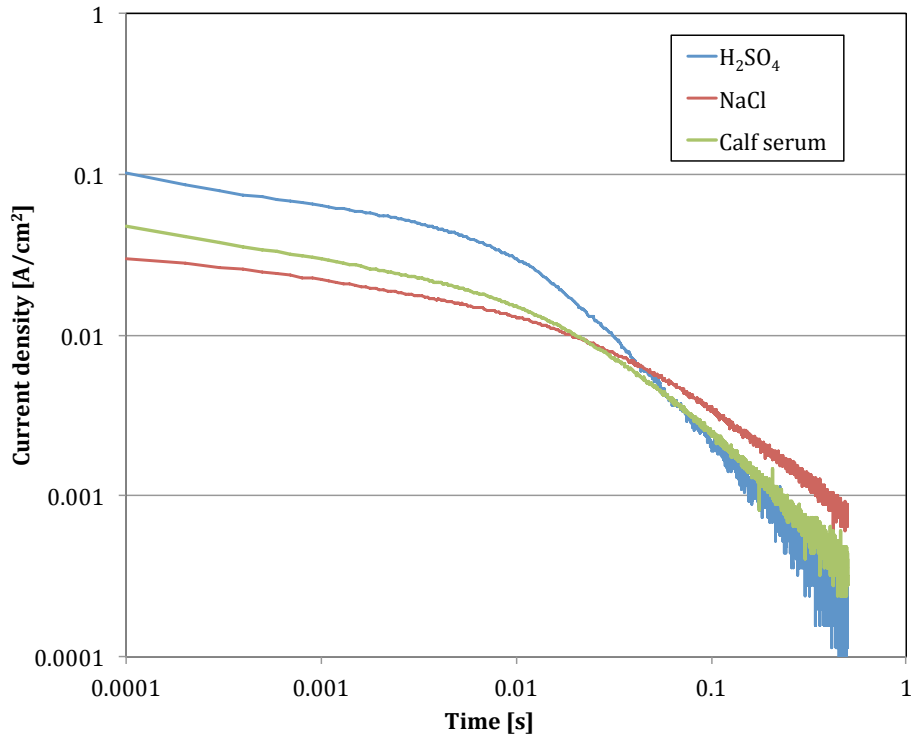
Figure 4.4 Current transients of the CoCrMo alloy in logarithmic scale from potential step tests in different solutions at similar potentials (-0.154 V_{SHE} for H_2SO_4 and -0.1 V_{SHE} for NaCl and calf serum)

4.1.3 The correlation between passivation charge density and applied potential

The result of the measured passivation charge densities in the three solutions is shown in Figure 4.5 together with the five data points from the literature [30] and [62]. In the current experiments, seven potentials were applied to a low carbon CoCrMo alloy in the 0.5 M H_2SO_4 solution and among them, -0.046 V_{SHE} is very close to the OCP of the polarization curve and 1.154 V_{SHE} is close to the transpassive domain. Surprisingly, a very good linear correlation is found between the passivation charge density in the 0.5 M H_2SO_4 solution except a large scattering at 1.154 V_{SHE} which is probably due to the unstable status of the generation and dissolution of the passive film near the transpassive domain. Two potentials were chosen for the NaCl and calf serum solutions respectively. It can be seen from Figure 4.5 that the eight data points (four from NaCl solution and four from calf serum solution) follow very well the correlation between the passivation charge density and applied potential

measured in the H_2SO_4 solution. Figure 4.5 also shows the results from [62] where also low carbon CoCrMo alloy was used correspond very well to the results observed from the current experimental result. The results from [30] where a high carbon CoCrMo alloy was used are close to the current results with one point following well the trend and the other two points a little higher. This indicates that high carbon CoCrMo alloys may have higher passivation charge density. However, measurement of passivation kinetics is sensitive to the set-up used. Therefore, more experimental results with the same set-up are needed in order to confirm the possible influence of carbon content on the passivation kinetics of CoCrMo alloys.
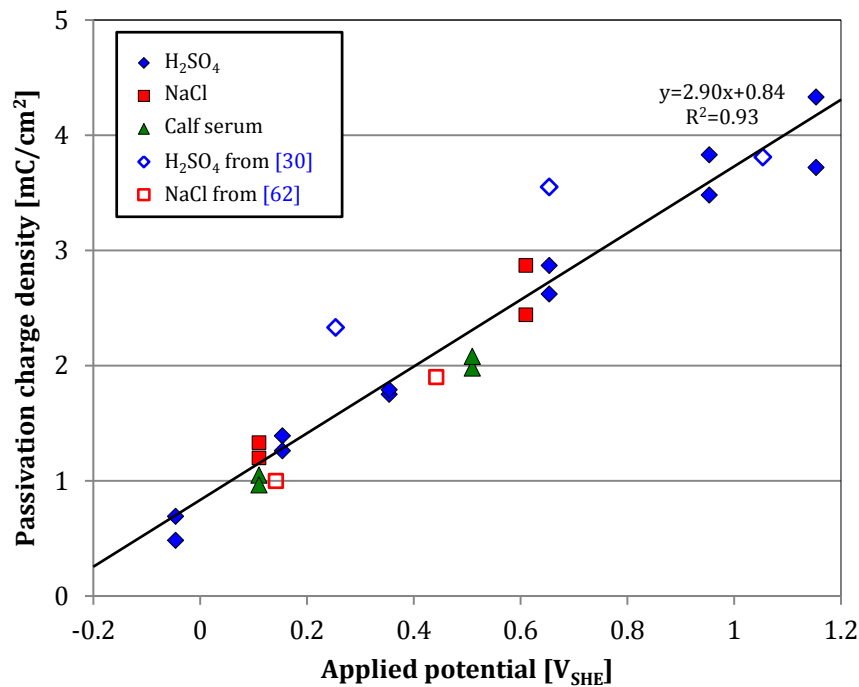
Figure 4.5 The correlation between passivation charge density of CoCrMo alloys and applied potential measured in three different solutions

A trend line for all the data points in Figure 4.5 is drawn which shows that, for CoCrMo alloys, the passivation charge density is highly dependent on the applied potential but not on the solutions at least for the three typical solutions considered in this study. Thus, Equation 4.1 can be obtained as a simple method to estimate the passivation charge density for CoCrMo alloys at any passive potential.

$$Q_p = 2.90E_{electrode} + 0.84 \qquad\qquad (4.1)$$

Based on this, Q_p for CoCrMo alloys can be extracted from this equation by knowing electrode potentials since measuring electrode potentials in simulators [27,28] or tribometers [24,26,29,30,59] is certainly much easier than carrying out potential step experiments.

4.2 Comparison of the wear

Igual Munoz et al. [34,63] studied tribocorrosion of a high carbon biomedical CoCrMo alloy using the same ball (Al_2O_3)-on-disk (CoCrMo alloy) configuration but applying a unidirectional sliding and in 0.14 M NaCl solution. Normal load (5 N) and sliding velocity (18.85 mm/s) were kept constant. Two different passive potentials (0.25 and 0.7 V_{SHE}) were applied and the CoCrMo alloy was subjected to different heat treatments in order to alter its microstructure.

The micro hardness of the CoCrMo alloy inside and outside the wear track was also measured but using a load of 0.5 kg and work hardening was also reported in these studies. The hardness inside the wear track is about 500 HV with only little difference for the different heat treatments. The passivation charge density was not measured in these two studies but can be approximated using Equation (4.1) since the applied potential is known. This yields 1.57 and 2.87 mC/cm^2 for potentials at 0.25 and 0.7 V_{SHE}, respectively. In this case, all the required parameters are available and thus Equation (3.9) can be used to predict the mechanical and chemical wear for the tribocorrosion system described in these studies and the model predictions can be compared to the experimental results, as shown in Figure 4.6.

Considering the approximation of the passivation charge density and the different heat treatments employed, the predicted mechanical, chemical and total wear values relatively well correspond to the two groups of experimental data. The model predicted values well lie inside the variation of the experimental results at 0.25 V_{SHE} considering the error bars. This verifies the calibration of the k_{chem} and k_{mech} values.
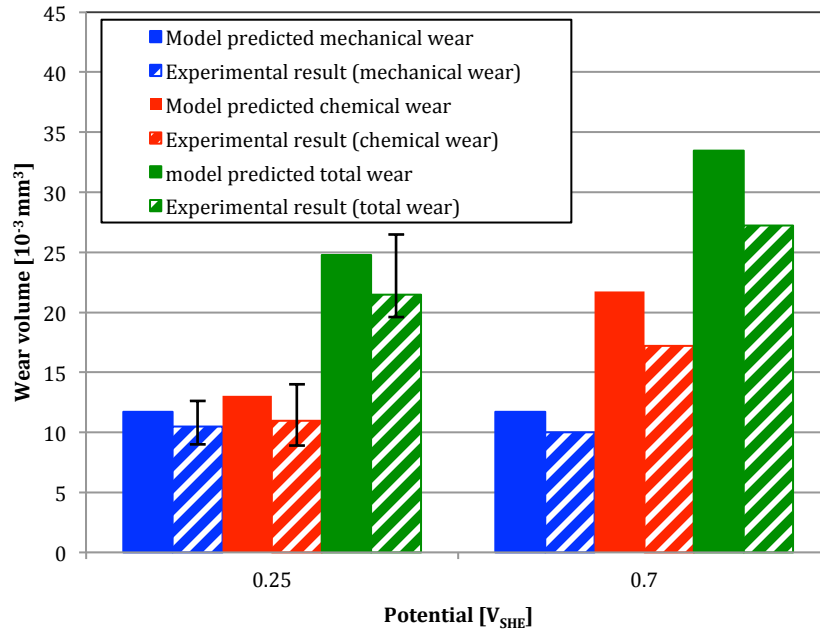
Figure 4.6 The comparison between model predicted wear and experimental data from [34] and [63]

The other comparison is to the simulator experimental results reported by Dowson [23], as shown in Figure 2.14. The instantaneous normal force and angular velocity in Figure 2.10 were applied to the model to calculate the instantaneous wear rate during one gait cycle. The wear volume in one second (or in one gait cycle at 1 Hz) can be obtained by integrating the instantaneous wear rate from 0 to 1 s.

In the literature, a few studies [27,28] reported the potential of CoCrMo alloys (established OCP before, during and after the testing) in simulator experiments ranging approximately from -0.3 to 0.2 V_{SHE}. Considering an average potential of -0.05 V_{SHE}, it yields the Q_p value of 0.70 mC/cm² according to Equation (4.1).

The representative time of the running-in period in simulator experiments is approximately 1 million cycles, which is estimated equivalent to 1 year of the artificial hip joints in human body according to [23]. Then, the running-in wear can be estimated by multiplying the wear volume in one second by 1 million. Predictions considering a typical head radius (18 mm) and several different clearances are shown in Figure 4.7 (blue dots and interpolating line) together with the experimental values reported by Dowson [23] (black dots).

Interestingly, the model predictions are very close to the experimental

data. It is not surprising that the prediction curve follows the fitting line from Dowson (black line in Figure 4.7) because the model is developed based on this wear-film thickness correlation. However, the model predicts quite precisely the real values of the experimental results. This also confirms the validity of the model for predicting the running-in wear of CoCrMo MoM artificial hip joints.
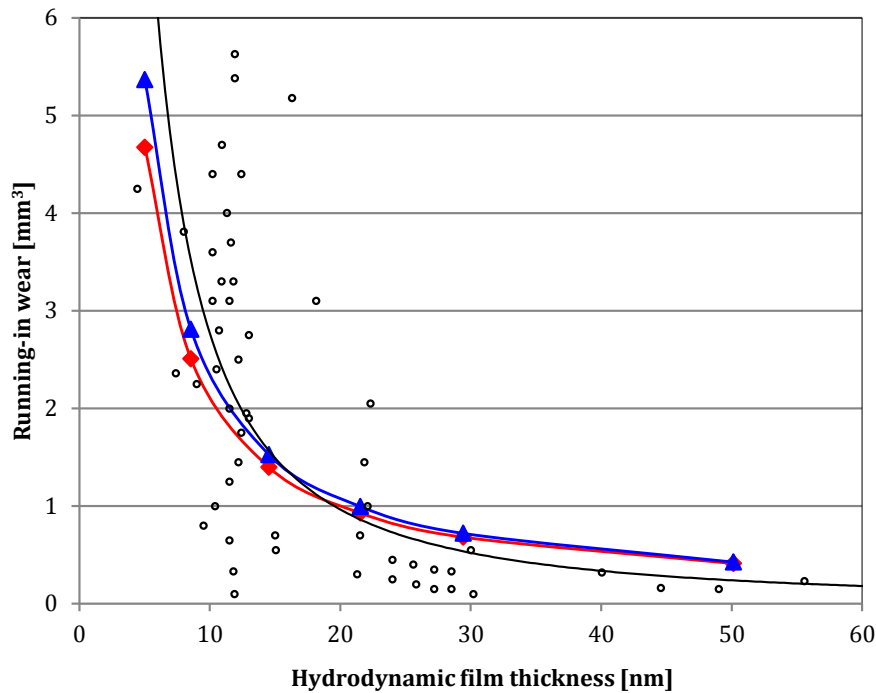
Figure 4.7 The experimental running-in wear results (black dots) with different film thicknesses and fitting line (black line) from [23] and model predicted values from integral of instantaneous wear rate (blue dots and interpolation) and using average load and velocity (red dots and interpolation) (R=18 mm, c_R=200 μm, 100 μm, 50 μm, 30 μm, 20 μm and 10 μm, successively)

In order to simplify the calculation, average normal load and velocity in one cycle are commonly used in the quantitative assessment of loading and wear of artificial hip joints. In order to verify the accuracy of this simplification, the average wear rates were calculated using Equation (3.9) by considering an average normal load of 1500 N and an average angular velocity of 1.5 rad/s based on the load and angular velocity curves from ISO 14242-1 (Figure 2.10). Calculated values are plotted in Figure 4.7 with red dots. It can be found that the calculated values using average normal load and angular velocity can still represent the experimental running-in wear with a sufficient precision. So, for

the calculations of the running-in wear rates of artificial hip joints, in order to reduce the mathematical work, average normal load and angular velocity can be systematically used.

4.3 Conclusion

The composite model involves a number of parameters that are seldom fully reported in tribocorrosion studies. The applicability of the model is limited by the lack of the information of the essential parameters. Among them, passivation charge density is a very important parameter in the model but often been omitted.

A good linear correlation was found between the passivation charge density and applied potential for CoCrMo alloys in three solutions (H_2SO_4, NaCl and calf serum).

This correlation shows that passivation charge density is highly dependent on the applied potential but little dependent on the solutions, at least for CoCrMo alloys.

When the passivation charge density was estimated based on this correlation, the model was found to predict well the wear rates observed in two tribometer experimental studies and the running-in wear obtained by Dowson.

Chapter 5 Model validation for MoM artificial hip joints

In this chapter, the validity of the composite model will be assessed by comparing the model predicted wear rates with experimental results concerning self-mated CoCrMo MoM hip joints as tested in hip joint simulators. For this, firstly a thorough literature review about the MoM simulator experimental studies were carried out and subsequently the parameters were extracted from the selected papers fulfilling the criteria and applied to the model to predict wear rates. Finally, the model predicted wear rates were compared with the experimental results from the papers.

5.1 Literature review

A literature review of simulator wear studies was carried out using the keywords "metal on metal", "simulator" and "hip" with timespan from 1995 to 2015. 353 publications were found in ISI Web of Science searched in May 2015. However, only a small fraction of these studies really carried out the simulator experiments. Even in the studies which carried out the simulator experiments, some didn't report the values of the essential parameters such as clearance and some only gave the final wear loss after the whole experiments instead of the evolution of the wear loss. So, these papers carried out simulator experiments were then further filtered under the criteria listed here:

- The metal for the head-cup articulation was self-mated CoCrMo alloys (biomedical standard).
- The head radius and clearance were clearly given.
- The load curve, motion type and frequency of the simulator experiments were described.
- Calf serum solutions were used as lubricant (usually with additives such as NaN_3 and EDTA).
- The evolution of wear loss (volumetric or gravimetric) with testing time

(cycles) was clearly given (this is necessary to calculate the wear rate and to determine the running-in period).

Only 19 papers were finally found to fulfill these criteria and the results were collected in order to compare with the model predicted values.

From the composite model described in Chapter 3, it is clear that the normal load and sliding velocity act as important parameters influencing the wear rate of implant materials. To simulate the hip joint's activity, basically normal walking, specific loading and movements should be applied to the simulators. In order to reproduce the complex loading and motion of hip joints, people divided the motion into three components: flexion-extension (FE) in the sagittal plane, abduction-adduction (AA) in the frontal plane and internal-external rotation (IE or IER) in the transverse plane, as shown in Figure 5.1. The total load can also be divided into three components along the axis. Since the W_y is much higher than W_x and W_z, normally only W_y is applied in the simulator experiments.
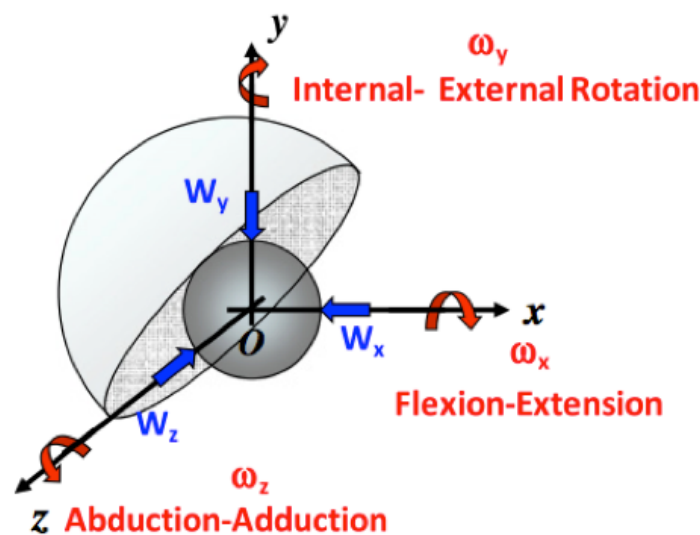
Figure 5.1 Loading and motion components of ball-in-socket hip joints [8]

The loading and movements of healthy hip joints in the walking gait have been measured by biomechanists featured by the widely used Paul's curve [64] for the loading. Johnston [65] measured the motion of hip joint in walking, which formed the basis of motion waveform design. Both of the load curve and motion

waveforms were measured in 1960s and then different hip joint simulators were designed and used to evaluate the wear properties of implant materials since 1970s [66]. However, in these simulator experiments, the load curve and motion waveforms were modified (mostly simplified) to adapt the simulator or reduce the complexity of the simulator motions. From 2000, the International Organizations for Standardization (ISO) developed an international standard (ISO14242) to suggest the specifications (load curve, motion waveform and wear loss measurement) of the simulator experiments in order to obtain comparable results from different simulator experiments. Figure 5.2 shows the load curve and motion waveforms from ISO14242-1. However, from the literature review, the standard was not well followed. Simplified or more complicated loading curves and motion waveforms were found, as shown in Figure 5.3 (a) and (b).

(a)

(b)
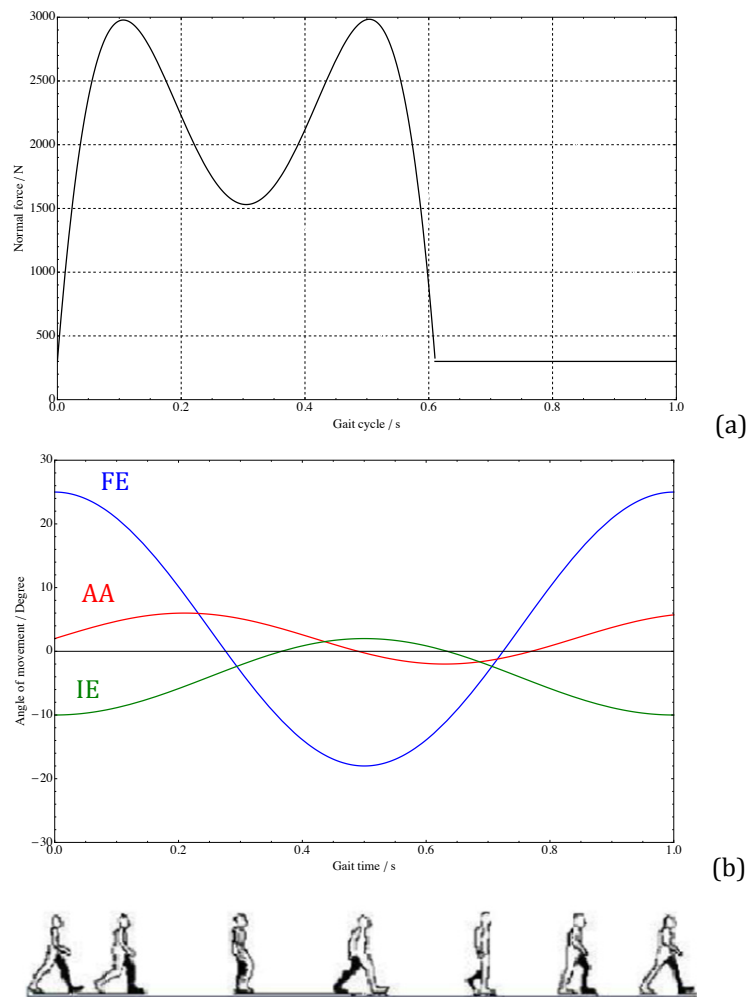
Figure 5.2 The load curve and motion waveforms of hip joint simulator according to ISO14242-1
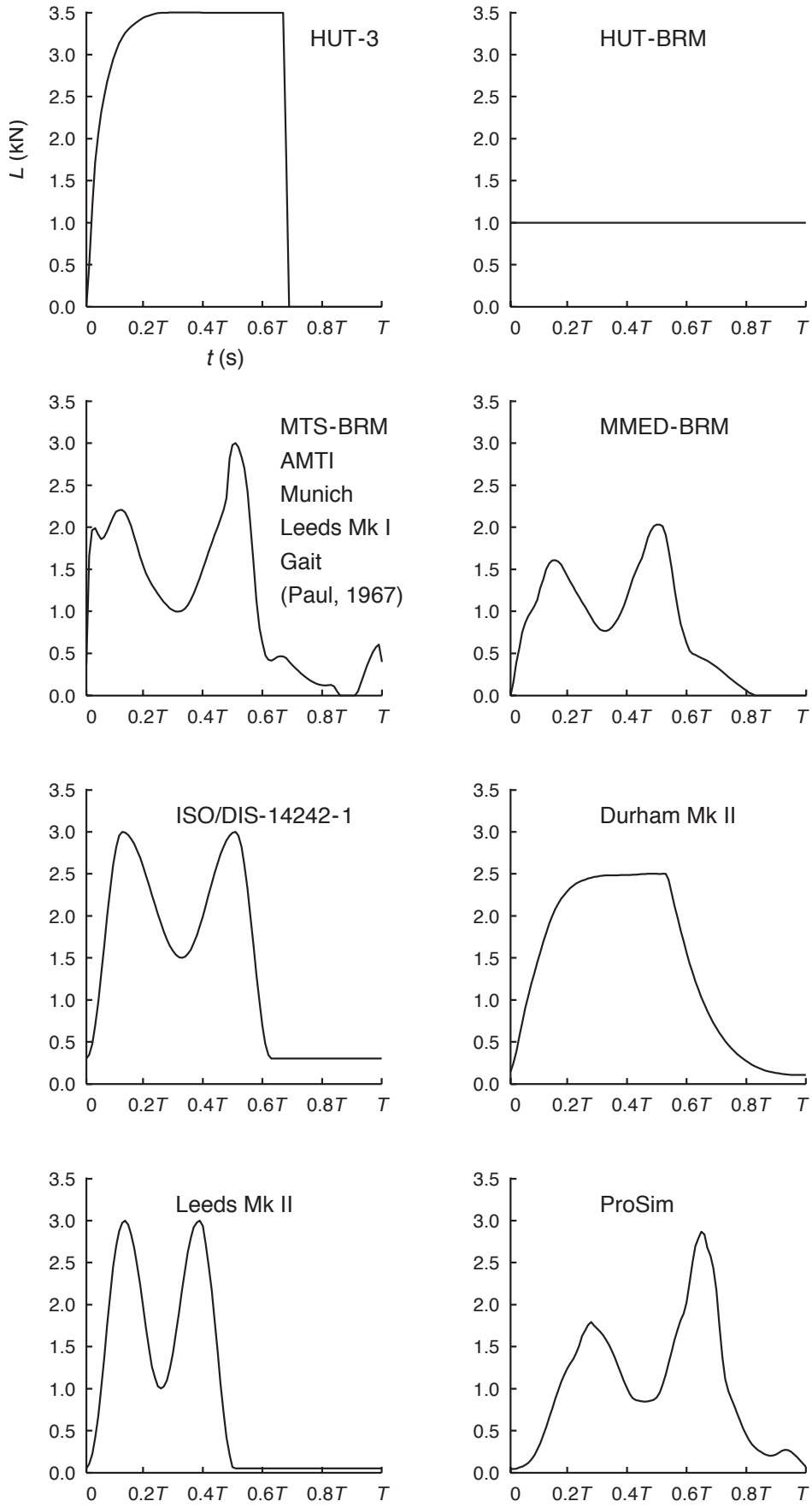
(a)
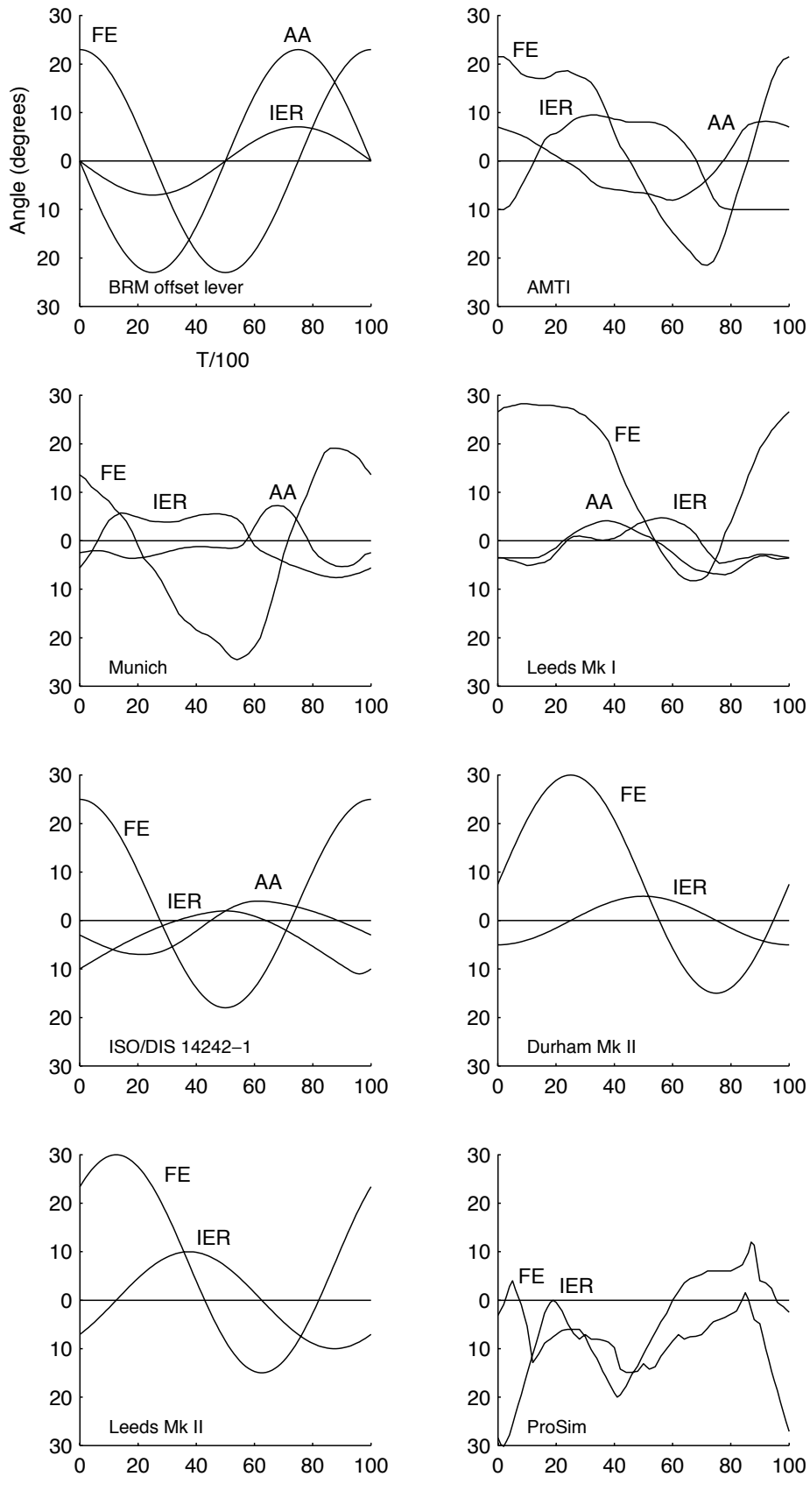
Figure 5.3 The loading curves (a) and motion waveforms (b) used in the existing hip joint simulators [67,68]

Calonius et al. [67,68] reviewed the existing simulator designs and found big differences in the loading curve and motion waveforms used in the existing simulators. As shown the different loading curves in Figure 5.3(a) and motion waveforms in Figure 5.3(b). They also studied the sliding tracks between the head and cup based on the motion of the simulators and from this, the length of the sliding track can be measured in one cycle. Saikko et al. [69] found that the wear of most acetabular cup materials are highly sensitive to the type of motions while less sensitive to the type of loadings, which may be the reason of large difference of wear rates observed in different simulators.

The selected papers in this thesis covered eight types of simulators with orbital (a special type of two axis motion), two axis or three axis motions, as summarized in Table 5.1. All of these motions result in multidirectional movements between the head and cup. Different twin-peak load curves were applied and even for the same type of curve, different maximum values were used in different studies. The average load was calculated by averaging the load curve in one cycle. The sliding velocity is not constant during a gait cycle except in the case of orbital motion. In order to extract the necessary input values for the model prediction, the sliding velocity was calculated by firstly determining for each specific simulator configuration the length of the sliding track given by Calonius et al. [67] and afterwards by multiplying the track length by the motion frequency. The results are shown in Table 5.2.

The effective radius of curvature R' was calculated from the given head radius R and radial clearance c_R using Equation 5.1:

$$\frac{1}{R'} = \frac{1}{R} - \frac{1}{R + c_R} \tag{5.1}$$

Average values for the charge number n, molecular mass M and alloy density ρ as taken from the literature related to biomedical CoCrMo alloys are 2.37, 58.66 g/mol and 8.3 g/cm^3, respectively.

Some other model parameters were not indicated in the considered publications. The application of the model requires thus taking some assumptions regarding missing factors. These assumptions are discussed in the following section.

Table 5.1 Summary of the experimental parameters extracted from the simulator wear studies

No.	Reference	CoCr Alloy[a]	R [mm]	c_R [mm]	Simulator name	Motion type	Load curve[b]	Load (N)	Frequency[c] (Hz)
1	Medley JB, 1998 [70]	LC wrought CoCrMo (ASTM F1537) / HC wrought CoCrMo (ASTM F1537)	14	0.053-0.054 / 0.0435-0.0485	MATCO	Orbital	Paul	176-2100	1.14
2	Chan FW, 1999 [71]	LC wrought CoCrMo (ASTM F1537) / HC wrought CoCrMo (ASTM F1537) / HC cast CoCrMo (F75)	14	0.0432-0.0508 / 0.0178-0.0381 / 0.0051-0.0432	MATCO	Orbital	Paul	0-2100	1.13
3	Pare P, 2003 [72]	HC wrought CoCrMo (ASTM F1537) / LC wrought CoCrMo (ASTM F1537)	14	0.0298-0.0585 / 0.0329-0.0335	MATCO	Orbital	Paul	0-2100	1.14
4	Catelas I, 2003 [73]	HC cast CoCrMo (ASTM F75) / HC wrought CoCrMo (ASTM F1537) / LC wrought CoCrMo (ASTM F1537)	14	0.0305 / 0.033-0.0381 / 0.0178-0.0229	MATCO	Orbital	Paul	0-3400	1.13
5	St John KR, 2004 [74]	HC wrought CoCrMo (ASTM F1537)	14	0.043	MTS	Orbital	Paul	0-3000	1
6	Bowsher JG, 2006 [75]	HC cast CoCrMo (ASTM F75)	20	0.104-0.144	MTS	Orbital	Paul	0-2450	1
7	Angadji A, 2008 [76]	HC cast CoCrMo (ASTM F75)	20	0.15	MTS	Orbital	Paul	0-2500	1
8	Bowsher JG, 2009 [77]	HC cast CoCrMo (BS 7252-4)	30	0.12-0.124	Shore-Western	Orbital	Paul	200-2200	1
9	Goldsmith AAJ, 2000[78]	HC wrought CoCrMo (ASTM F1537)	14 / 18	0.0563 / 0.071	Prosim	2 axis	Prosim	0-2870	1.08
10	Dowson D, 2004 [79]	HC wrought CoCrMo (ASTM F1537)	18	0.06-0.066	Prosim	2 axis	Prosim	300-3000	0.93
11	Dowson D, 2004 [80]	HC wrought CoCrMo (ASTM F1537)	14 / 18	0.0275-0.035 / 0.038-0.039	Prosim	2 axis	Prosim	300-3000	0.93
12	Leslie I, 2008 [81]	HC cast CoCrMo (ASTM F1537) / HC cast CoCrMo (ISO 5832)	27.25 / 19.25 / 27.25	0.0415-0.0645 / 0.0555 / 0.063	Prosim 2	2 axis	Prosim	280-3000	1
13	Li CX, 2011 [82]	HC cast CoCrMo (ASTM F75)	25	0.118-0.122	Prosim	2 axis	Prosim	300-3000	1
14	Hesketh J, 2013 [83]	HC wrought CoCrMo (ASTM F1537)	18	0.041-0.043	Prosim	2 axis	Prosim	150-3000	1
15	Yan Y, 2013 [84]	HC wrought CoCrMo	18	0.05	Prosim	2 axis	Prosim	280-3000	1
16	Al-Hajjar M, 2013 [85]	HC CoCrMo	14 / 18	0.02 / 0.0238	Leeds II	2 axis	Leeds II	0-3000	1
17	Scholes SC, 2001 [86]	LC wrought CoCrMo (ASTM F1537)	14	0.022-0.04	Durham	2 axis	Durham	0-3000	1
18	Firkins PJ, 2001 [87]	LC wrought CoCrMo (ASTM F1537) / HC wrought CoCrMo (ASTM F1537)	14 / 14	0.022 / 0.028	Leeds I	3 axis	Paul	0-2600	1
19	Kretzer JP, 2010 [88]	HC cast CoCrMo	23.5	0.046	Minibionix 858	3 axis	ISO14242-1	300-3000	1

[a] LC: low carbon, HC: high carbon.
[b] In absence of indication the minimum load was assumed to be 0 N.
[c] In absence of indication the frequency was assumed to be 1 Hz.

Table 5.2 Summary of calculated average normal load and sliding velocity for the simulator wear studies

No.	Reference	Average load (N)	Length of wear track (mm)	Sliding velocity (mm/s)
1	Medley JB,1998	891	2.46R[a]	2.8R
2	Chan FW,1999	792	2.46R	2.78R
3	Pare P,2003	792	2.46R	2.8R
4	Catelas I,2003	1269	2.46R	2.78R
5	St John KR,2004	1120	2.46R	2.46R
6	Bowsher JG,2006	914	2.46R	2.46R
7	Angadji A,2008	933	2.46R	2.46R
8	Bowsher JG,2009	946	2.46R	2.46R
9	Goldsmith AAJ,2000	994	1.65R	1.78R
10	Dowson D,2004	1209	1.57R	1.46R
11	Dowson D,2004	1209	1.57R	1.46R
12	Leslie I,2008	1196	1.57R	1.57R
13	Li CX,2011	1209	1.57R	1.57R
14	Hesketh J,2013	1110	1.57R	1.57R
15	Yan Y,2013	1196	1.57R	1.57R
16	Al-Hajjar M,2013	894	1.57R	1.57R
17	Scholes SC,2001	1039	1.59R	1.59R
18	Firkins PJ,2001	970	1.41R	1.41R
19	Kretzer JP,2010	1457	1.58R	1.58R

[a] R: head radius.

5.2 Assumed values for unreported parameters

The model involves material, mechanical, electrochemical and lubrication related parameters and two proportionality factors. Unfortunately, these parameters are rarely exhaustively indicated in the literature. Specific parameters and the clarification are listed in the following part.

Elastic parameter E': This composite parameter is described by Equation (5.2):

$$\frac{2}{E'} = \frac{(1-v_1^2)}{E_1} + \frac{(1-v_2^2)}{E_2}$$

(5.2)

The Young's modulus E and Poisson's ratio v varies in principle with composition and microstructure of the specific CoCrMo alloy. The literature reported Young's modulus lying typically in a range from 210 to 250 GPa. Thus for the calculation, an average value of 230 GPa was considered. As in the case of many metals, the Poisson's ratio is usually approximated to the value of 0.3.

Viscosity η: The environment of the artificial hip joints in human body is

synovial fluid and, as simulated solution, calf serum has been widely used in simulator tests. Both of these two solutions are non-Newtonian fluid, which means the viscosity varies at different shear rates. However, it is commonly assumed that these two fluids have a constant viscosity since the shear rate is high in MoM artificial hip joints when walking [23]. Normally, the calf serum is been diluted to get the same protein content (25% as recommended by the ISO 14242-1 standard) as synovial fluid. This yields a viscosity of 0.9 mPa·s, a value very close to that of water [23]. Note that however in some studies listed in Table 5.1 [70-74] undiluted calf serum was used. This likely implies a different viscosity. In absence of measured viscosities, in the following, a value of 0.9 mPa·s was used for calculations.

Hardness _H_: the model assumes that wear is proportional to the extent of plastic deformation of surface asperities. Thus, the hardness of the outermost surface layers of the metal should be considered for model calculations. Indeed, the hardness of the surface may differ from that of the bulk because, under the effect of friction, the surfaces work hardened. This is typically the case of CoCrMo alloys in tribocorrosion conditions where the surface micro-hardness was reported to increase up to 50% during rubbing depending on test conditions [30]. Thus, the micro-hardness or nano-hardness of wearing surfaces should be measured in order to predict the wear behavior. Among the papers listed in Table 5.1, no one reported either micro- or nano-hardness of the worn surface. Macro-hardness of a self-mated high carbon CoCrMo contact surfaces was measured by St. John et al. [74] using Rockwell C methods after simulator tests. However, macro-hardness yields values average over a large indentation depth (approximately 0.2 mm for HRC values around 40) that are not necessarily representative for the hardness at asperity scale (normally below 1 μm).

In absence of representative data, in the present chapter we assumed a constant hardness of 400 HV corresponding to the bulk hardness of most of the biomedical CoCrMo alloys. Doing this, we neglect work hardening effects and, as a consequence, the model predictions likely overestimate wear.

Passivation charge density Q_p: The passivation charge density is an electrochemical parameter introduced in tribocorrosion modeling by Mischler et al. [26] in 1998. It corresponds to the charge density needed to passivate a unit

bare metal surface, i.e. a surface not covered by the passive film. The methods to measure passivation charge densities have been reviewed in [26]. The passivation charge density depends on metal, electrolyte and electrode potential. Indeed, the electrode potential determines the thickness of the formed passive films and thus the amount of metal that needs to be oxidized to form it [26,62].

In the literature, no studies measured the passivation charge density of CoCrMo alloy in calf serum. Only few data are available on the passivation charge density of biomedical CoCrMo alloys in sulfuric acid and in sodium chloride solutions [30,62]. In section 4.1, the passivation charge density of a CoCrMo alloy was measured in three solutions (0.5 M sulfuric acid, 9 g/L sodium chloride and calf serum solutions) and a quite good linear correlation was found between the passivation charge density and applied potential (Figure 4.5). So, the evolution of the passivation charge density for CoCrMo alloys with the electrode potential can be approximated by the following empirical linear correlation:

$$Q_p = 2.90 E_{electrode} + 0.84 \qquad (5.3)$$

where, the electrode potential $E_{electrode}$ is expressed in Volt with respect to standard hydrogen electrode (V_{SHE}). Note that Equation (5.3) is valid only in the passive domain [33], i.e. for potentials above the passivation potential and below the transpassive potential.

The electrode potential of CoCrMo alloys (established OCP before, during and after the testing) in simulators was only measured in a few studies [27,28,83,84] that reported values ranging approximately from -0.3 to 0.2 V_{SHE}. Accordingly, Equation (5.3) yields Q_p values of 0 to 1.42 mC/cm². In the following, an average passivation charge density of 0.70 mC/cm², corresponding to an average potential of -0.05 V_{SHE}, is considered for calculations. Considering the above electrode potential range reported in literature, assuming a constant average passivation charge density may yield errors of up to 100% in the prediction of chemical wear.

Proportionality factors k_{mech} and k_{chem}: These two factors should be calibrated for each studied metal or alloy. The calibration of these two factors requires well-designed and controlled tribocorrosion experiments with every critical parameter correctly measured (e.g. the passivation charge density and

micro surface hardness inside the wear track) and mechanical and chemical wear contribution clearly identified. Tribo-electrochemical techniques [24,89] are particularly well suited for these experiments.

As described in section 3.2, out of the experiments carried out by Guadalupe et al. [30], the k_{mech} and k_{chem} of 0.1363 and 750.35 were obtained [90] and used for calibration. These factors are in principle specific for the CoCrMo alloy studied in [30]. Indeed, under identical tribocorrosion conditions, different CoCrMo alloys can yield different wear rates. For example, Casaban et al. [63] studied the tribocorrosion of a high carbon CoCrMo alloy in body simulated solutions (NaCl, NaCl+BSA (bovine serum albumin), BS (bovine serum)) in a laboratory tribometer and observed that depending on the heat treatment applied before test, the wear rate changed by approximately 50%. Dowson [79] observed a similar scattering in wear when testing different high and low carbon, cast and wrought CoCrMo alloy combinations in a hip joint simulator. Furthermore, in section 3.2, for the three CoCr alloys, a variation of approximately ±50% for the k_{mech} and k_{chem} from the values obtained from S21 alloy were found. Thus, we can assume that applying the calibration parameters k_{mech} and k_{chem} obtained from the data from [30] to other CoCrMo alloys may introduce an error of approximately 50%.

5.3 Comparison between model predicted wear rates and wear rates measured in simulators

The experimental total wear rate was obtained by dividing the total wear volume measured after the simulator test with the testing time. This value was compared to the model predicted value calculated using the data given in the literature and, in case of absence of indication, the assumed values discussed in the section 5.2 were used. The experimental total wear rates are plotted in Figure 5.4 as a function of the corresponding model predicted values.
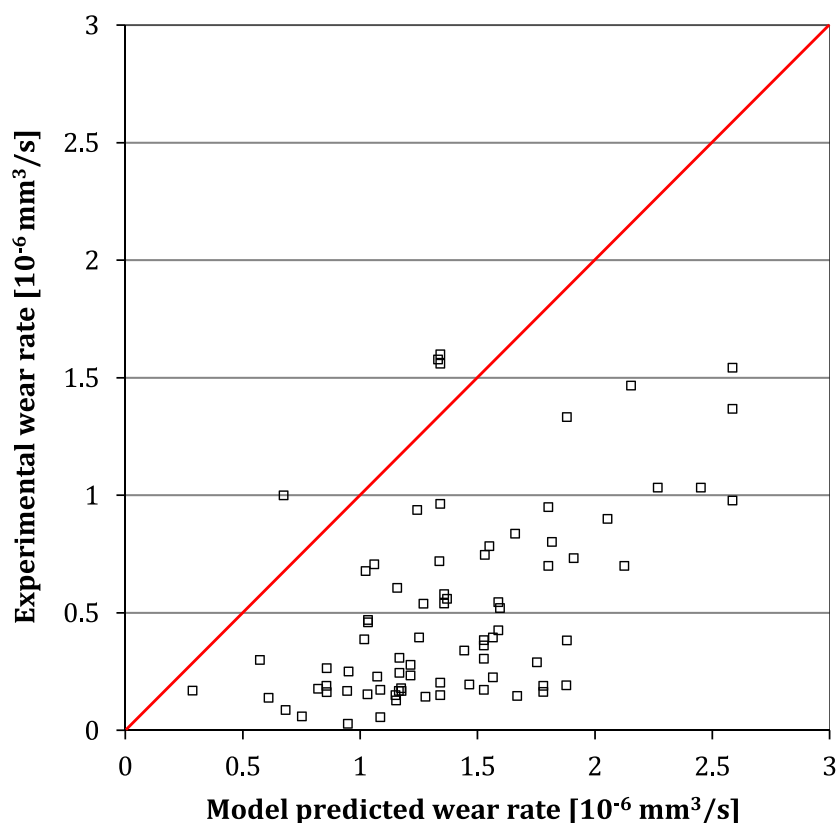
Figure 5.4 Correlation between experimental total wear rates and model predicted running-in wear rates (the solid line has slope 1)

It can be seen that more than 95% of the dots lie in Figure 5.4 below the slope 1 line which means most of the experimental wear rates are lower than the model predicted ones. This is not surprising since the model is based on the Dowson's empirical correlation between wear and hydrodynamic film thickness for the running-in period only. However, the running-in period is usually characterized by high wear rate compared to the subsequent steady state period. Thus, the model gives an upper limit of the wear rate in case the system remains in the running-in period during the whole test. Fig. 5.4 is consequent with this vision as most of the experimental results are lower than the predicted ones and none of them exceeds significantly the predicted values.

In order to get a more precise assessment of the model, the predictions were compared to the running-in wear rates extracted from the literature. There is no consistent method to determine the running-in period due to the fact that the wear rate of MoM hip joints changes during test duration. MoM hip joints usually show an initial high wear rate period followed by a low wear rate steady

state period. However, other wear evolutions are also observed in simulator studies. Bowsher et al. [77] described different types of wear evolutions. These trends can be summarized by three limiting cases shown schematically in Figure 5.5. In this figure, the trend 'a' corresponds to the usual wear evolution mentioned above. Curves 'b' and 'c' show "abnormal" wear evolutions characterized by the absence of a clear steady state period (curve 'b') or by repeated transitions to temporary steady state periods (curve 'c'). Unfortunately, the mechanisms controlling wear transitions in hip joint simulators are not yet understood. In the present study, running-in wear rates were extracted only from results following the trend 'a' of Figure 5.5.
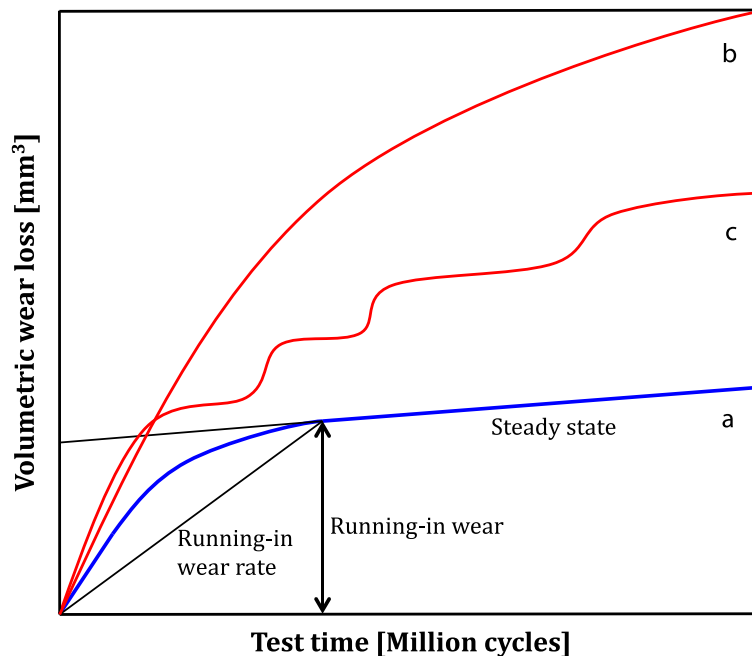
Figure 5.5 Different types of wear curves of MoM hip joints observed in simulator tests

For this, the experimental wear values measured in the steady state part of the plot wear versus time were interpolated using linear regression. The running-in time was defined as the time at which the experimental wear curve for the first time crosses the interpolation line as illustrated in Figure 5.5, curve 'a'. The running-in time determined in this way varies depending on studies from 0.3 million seconds (0.3 million cycles at 1 Hz) to 2 million seconds (2 million cycles at 1 Hz). This range is in reasonable agreement with the average running-in time usually assumed to be 1 million cycles [23]. The running-in wear rate of

the simulator wear studies was determined by dividing the wear volume at the running-in time by the corresponding time. The obtained experimental running-in wear rates are in the range of 0.2 to 3 ×10^{-6} mm^3/s (or 0.2 to 3 mm^3/million cycles at 1 Hz). This range corresponds well with average wear rates of CoCrMo MoM articulation reported in literature.

Figure 5.6 shows the comparison between the model predicted values and the running-in wear values extracted from the simulator wear studies. Despite the scattering due to uncertainties from the experimental parameters as discussed above, Figure 5.6 shows a surprisingly good correlation between model predictions and experimental values. Indeed, the data points are well aligned to the line of slope 1, indicating reasonably good match between the two sets of data (experimental and theoretical). Further, the calculations were made assuming a constant average passivation charge density and constant material specific factors such as k_{mech} and k_{chem}. However, different types of alloys were tested in the simulators at different electrochemical conditions, which determine Q_p values (Equation (5.3)), but were neither controlled nor generally reported.

Based on the deviation of the two constant factors k_{mech} and k_{chem} and passivation charge density Q_p, the deviation of the model prediction can be roughly determined. Considering the estimated scattering in k_{mech} and k_{chem} of ±50% and a scattering of ±100% in passivation charge density and assuming the mechanical and chemical wear rates contribute approximately equally to the total wear rate, the sum of the two deviations leads to an uncertainty of ±75% in the total wear rate. This uncertainty range was drawn in Figure 5.6 with two dashed lines. It can be seen that most of the experimental results lie within the uncertainty limits. On one hand, this supports the validity of the model for predicting wear of MoM artificial hip joints in simulators. On the other hand, it clearly shows the need for a better control of simulator experiments, including a control of the electrochemical condition and the determination of the tribocorrosion properties of the investigated CoCrMo alloys.
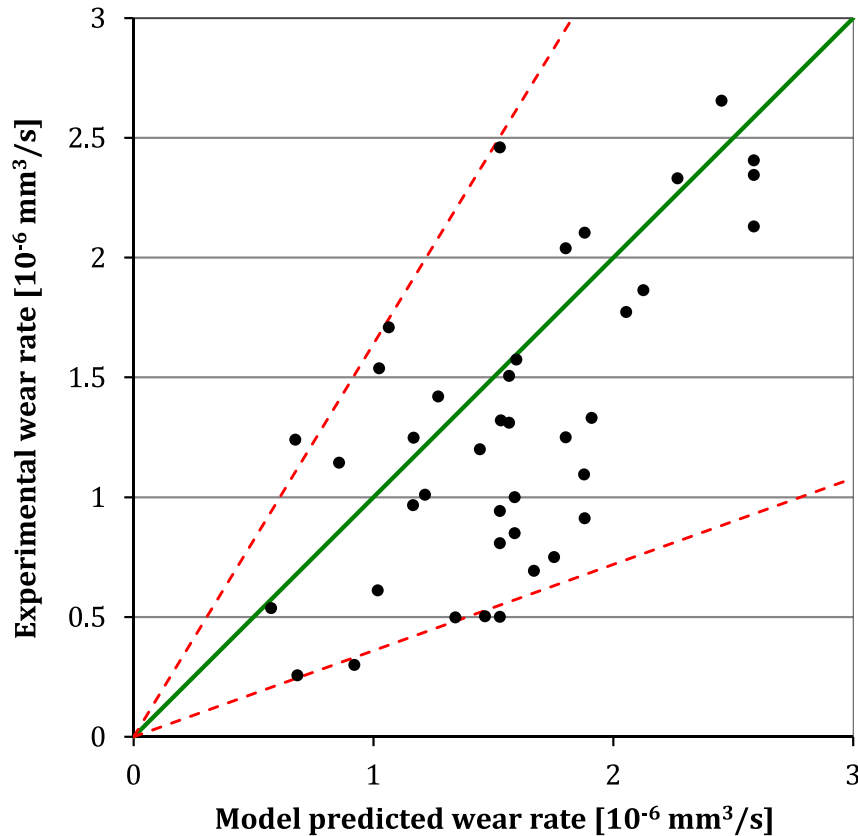
Figure 5.6 Correlation between experimental results and model predicted values of the running-in wear rates (The solid line has slope 1. Dashed lines represent expected uncertainty limits due to the various tested alloys and electrochemical conditions.)

5.4 Discussion

Predictions from the composite model for quantitatively assessing the wear of MoM hip joints were compared to published experimental data from hip joint simulators. The applicability of the model was limited by a number of crucial parameters that were not controlled or reported in most of the considered studies. In the composite model, k_{mech} and k_{chem} factors are material dependent and require calibration based on the material specific parameters such as passivation charge density Q_p and surface micro-hardness H.

The values of k_{mech} and k_{chem} were calibrated from a laboratory tribocorrosion study of a CoCrMo alloy carried out using tribometer. However, these values do not take into account the large variations (up to 50%) in tribocorrosion resistance observed among different CoCrMo alloys.

The passivation charge density Q_p of CoCrMo alloys, largely determined by

the electrode potential, depends in a complex way on the chemical properties of the alloys and of the environment as well as on mechanical loading of the surface. The electrode potential in simulator experiments was reported in a few publications only [27,28,83,84], which indicated that the electrode potential in simulator experiments could fluctuate in a wider range. This variation results in a corresponding uncertainty in Q_p and therefore in model predictions.

Further uncertainties are associated to possible work hardening effects influencing the micro-hardness of the material. Taking into account these uncertainties, a very good correlation was found between experimental results and model predictions. This indicates that the model constitutes a powerful tool to predict MoM hip joint wear rates provided adequate calibration and determination of key parameters are carried out. Dedicated simulator experiments performed under controlled electrochemical conditions with well-characterized alloy properties could definitively confirm the applicability of the model to MoM artificial hip joints.

The model offers the opportunity to predict the in-vivo wear rate of implants for individual patients. The loading and kinematics experienced by the implants can be measured using biomechanical approaches [91-93] or instrumented prostheses [94]. These methods give a more accurate picture of the loadings and movements than the simplified, standardized values usually applied in simulators.

Recently, Igual et al. [95] developed a method to measure electrochemical properties of metals such as CoCrMo alloys in synovial fluids directly extracted from patients pre or post total knee arthroplasty (TKA). This study revealed that the electrode potential of a biomedical low carbon CoCrMo alloy in human synovial fluids varies depending on patients between 0.09 and 0.35 V_{SHE}, i.e. a narrower range of higher values than reported for simulators operated in calf serum solutions. This may indicate that chemical wear is underestimated in the prediction of the simulator wear studies.

Viscosity of the synovial fluid is another key parameter for the present wear model. This factor varies also depending on patients and their health state [96]. Viscosity of patients could be measured from synovial liquids extracted with the same procedure as used for electrochemical studies [95].

For the model prediction, the hardness of the CoCrMo alloys before implantation has to be considered as the value cannot be measured in vivo to take into account possible work hardening effects occurring during service. Hardness measurements on explants and their registration in databases could help in assessing the relevance of work hardening of hip implants.

Once the proportionality parameters of the specific alloy considered have been determined in laboratory according to the procedure mentioned above, the model constitutes a simple method to predict the running-in wear rates of MoM artificial hip joint of individual patients.

5.5 Conclusion

In this chapter, a thorough literature review was carried out to collect the MoM hip joint simulator wear studies. The wear rates extracted from the selected nineteen studies were compared to the predictions from the composite wear model. The results lead to the following conclusions:

(1) When considering the total wear rates, the model predictions correspond to the upper limits of the reported experimental observations. This is in agreement with the fact that the model predicts running-in wear rate, which are larger than the steady state wear rate usually observed in simulators after typical running-in durations of approximately one millions cycles. Thus, the model can be used to estimate the maximum wear of CoCrMo MoM hip joints as a function of well-defined material, mechanical, electrochemical and lubrication related parameters.

(2) Comparison of model predictions with running-in wear rates extracted from the considered papers shows a good correlation despite the uncertainties on several model parameters that are not reported or measured in the simulator wear studies. The scattering range of several parameters could be estimated on the base of published work. Considering this range, the vast majority of the experimental results fall inside the expected scattering limits of the model predictions.

The above points validate the model for predicting simulator wear rates of MoM hip joints. The model also offers the possibility to predict the in-vivo wear

rates of implants for individual patients when specific parameters are determined with existing dedicated experimental techniques.

Chapter 6   The usefulness of the model for artificial hip joints

The model can be used to predict the instantaneous wear rate of MoM artificial hip joints and evaluate the influence of the involved material, mechanical, electrochemical and lubrication related parameters, which is very useful in instructing patients' activity, giving suggestions about how to optimize the design of hip implants and finding compatible hip implants according to the condition of individual patient.

6.1 Instantaneous wear rate during one gait cycle

Tribometers operate usually under constant normal load and velocity and thus the wear rate should not vary during one stroke. In order to mimic the loading and movement of natural hip joints, simulators adopt fluctuant normal load and velocity, as shown in Figure 6.1(a). Thus, variations of the wear rate are expected to occur during a gait cycle. The composite model allows estimating these variations during a single gait cycle once the values of the involved parameters are provided.

As an example, for a simulator experiment of MoM hip joints, a self-mated CoCrMo contact is considered and the values of the material dependent parameters used for calculation are: E=248 GPa, v=0.3, n=2.37, M=58.66 g/mol, ρ=8.3 g/cm^3. Sliding velocity is calculated by multiplying the radius of the head by flexion-extension angular velocity given by the ISO standard 14242-1:2012. A surface hardness of 400 HV for CoCrMo alloys and a fluid viscosity of 0.9 mPa·s for calf serum are assumed. The composite radius can be calculated using the head radius and clearance. Details of the calculation are described in section 3.2. An average passivation charge density of 0.70 mC/cm^2 were used. The wear rate predicted by the model under these conditions during a gait cycle is illustrated in Figure 6.1(b) as calculated according to Equation (3.9).
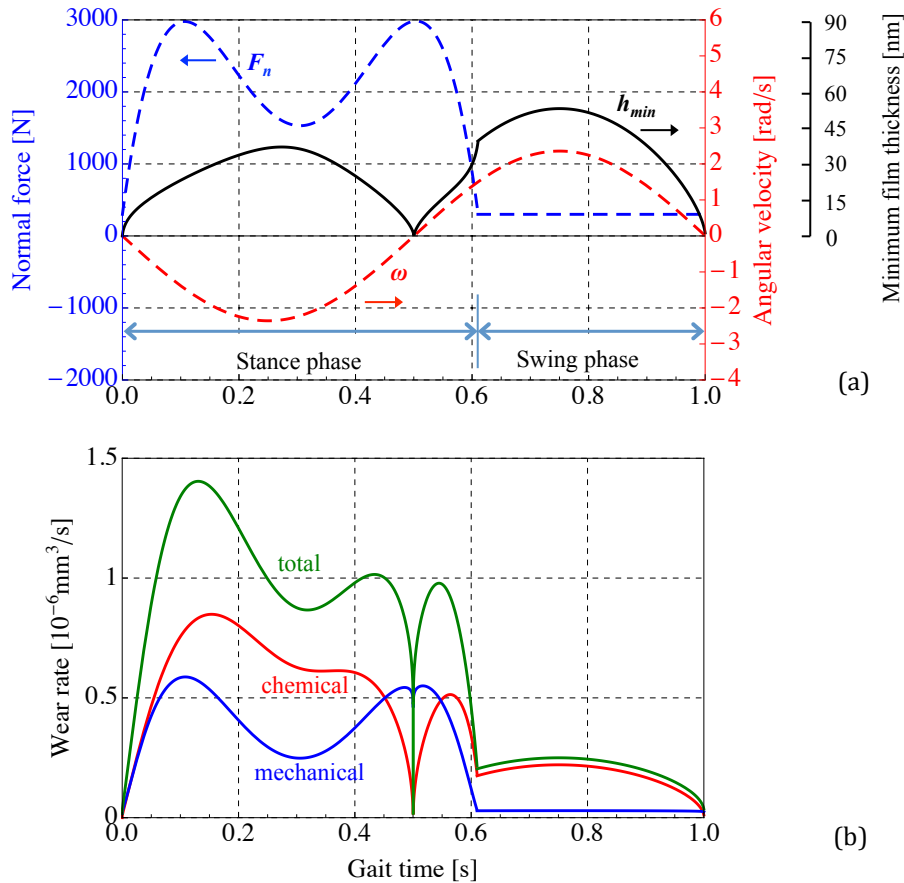
Figure 6.1 Evolution with time of normal force (dashed blue line), flexion-extension angular velocity (dashed red line) according to ISO 14242-1:2012 and calculated minimum film thickness (solid black line) in figure (a) and calculated mechanical (blue line), chemical (red line) and total (green line) wear rates in figure (b) (CoCrMo alloy, R=18 mm, c_R=30 μm)

From Figure 6.1(b), it can be seen that generally both mechanical and chemical wear contribute significantly to the overall wear. The evolution of mechanical wear with time follows the twin-peak shape of the normal force as expected from Archard's law while the chemical wear rather depends on the instantaneous combination of velocity and normal force. The gait cycle can be divided into two phases shown in Figure 6.1(a). The stance phase is when the corresponding leg is bearing featured with high normal force. Clearly, in this phase, both of the mechanical and chemical wear are high. In the swing phase, the normal force is low while angular velocity is high, thus the lubrication effect is very pronounced and significantly reduces both mechanical and chemical wear. In this case, the mechanical wear is very low due to the low normal force. However, this small mechanical wear is big enough to remove the passive film

which is only several nanometers thick and then, due to the wear accelerated corrosion, the chemical wear is relatively high, dominating the total wear in the swing phase. This can be clearly demonstrated in Figure 2.8. Assuming the potential doesn't change and thus passivation charge density is constant, passive film will be generated with the same thickness after each stroke and the fraction of chemical wear to the total wear will be very high when the wear depth is small. The integrated wear volume in the stance and swing phase is about 0.7 and 0.08 mm^3, respectively. The model shows that wear is mainly concentrated in the stance phase, while during the swing phase, the wear is much lower but still not negligible due to chemical wear.

6.2 Evaluating the effect of the parameters

The composite model allows assessing the role of the involved parameters on the running-in wear rate. This is of great importance to the geometrical design of the artificial hip joints, to the selection of the materials and to the guidance of the patient's activity after hip joint replacement. For this, the variation of the mechanical, chemical and total wear rates were calculated as a function of the typical parameters.

For MoM hip joints, the materials used for the head and cup articulation are CoCr or CoCrMo alloys (mostly). So the material parameters like Young's modulus E, Poisson's ratio v, composite oxidation valence n, atomic mass M and density ρ only have a very small range to vary. Faraday's constant F doesn't change. The other parameters normally vary and can have a large variation depending on the conditions. Head radius and clearance are designable parameters and different values have been used in MoM hip joints. It has been clearly shown that the normal force and angular velocity have a large variation in one gait cycle in Figure 6.1(a). Also, depending on the physical conditions and the activity of the patients, the amplitude of normal force and angular velocity can be larger or smaller which means the average normal force and angular velocity will be different. Work hardening has been widely found in tribocorrosion studies carried out in tribometers. Micro surface hardness was not commonly measured for the samples from simulator or explants, but the cross-sections of these

samples show the plastic deformation underneath the contacting surfaces of the head and cup [21,97], which probably cause work hardening. Depending on the patients and their health state, the viscosity of the synovial fluid has been found to vary in a certain range [96]. The passivation charge density depends on the potential that has been shown also to vary in a large range in simulator experiments [27,28].

To evaluate the influence of a specific parameter, default values were given to the other parameters for calculation, as shown in Table 6.1.

Table 6.1 Default values for the wear rate predictions for MoM hip joints

Parameter	Value
Materials	CoCrMo alloys
E and v	E= 248 GPa, v=0.3
Charge number (n)	2.37 (Co 2×63%, Cr 3×27% Mo 5×6%)
Molecular mass (M)	58.66 g/mol
Density (ρ)	8.3 g/cm^3
Faraday's constant (F)	96500 C/mol
Head radius (R)	18 mm
Radial clearance (c_R)	30 μm
Average normal force (F_n)	1500 N
Average angular velocity (v_s)	1.5 rad/s
Surface hardness (H)	400 HV
Viscosity (25% calf serum) (η)	0.9 mPa·s
Passivation charge density (Q_p)	0.70 mC/cm^2

Figure 6.2 shows the variation of mechanical, chemical and total wear rates with the increase of head radius and radial clearance. In general, larger head radius or smaller clearance gives lower wear rate essentially because both parameters lead to larger effective radius. Interestingly, mechanical wear decreases steadily with increasing head radius, while this is not the case for chemical wear that, according to the model, is much less affected by the head radius. A transition radius exists that below it, mechanical wear is much higher than chemical wear, while chemical wear is dominating when the head radius is large than this transition value. As a consequence, below approximately 20 mm, the increase of the head radius greatly decrease the wear rate of MoM hip joints, thus head radius as large as possible in this range should be used. However,

above 20 mm radius, the total wear is dominated by chemical wear and thus increasing the head radius does not imply significant reduction in wear despite the enhanced hydrodynamic lubrication effect. This model prediction agrees well with literature reports [42], which found that large head radius doesn't necessarily provide much lower wear. Using large head radius usually induces big geometrical size of the implant that increases the weight and fixing complexity of the artificial hip joints. Therefore, from this prediction, too large head radius is not recommended since the benefits are not significant.
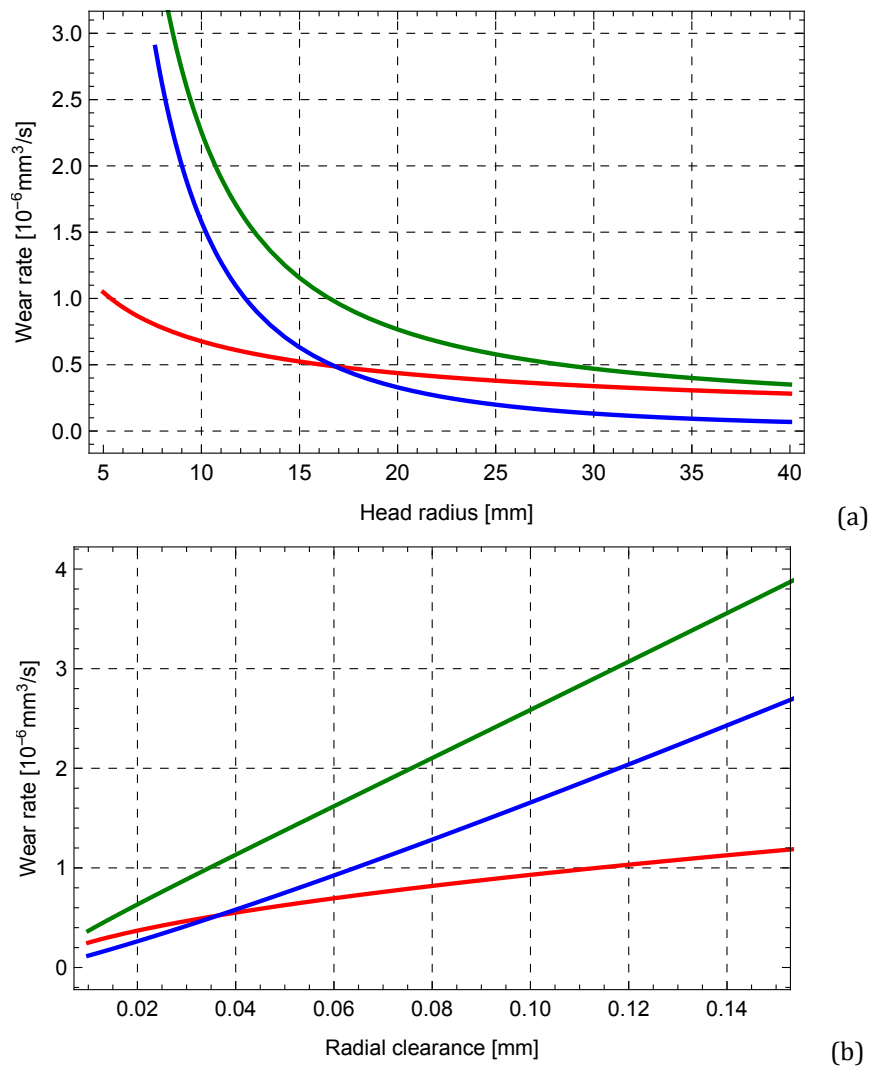

(a)

(b)

Figure 6.2 The variation of mechanical (blue line), chemical (red line) and total (green line) wear rate with head radius (a) and radial clearance (b) under hip joint simulator condition

As shown in Figure 6.2(b), smaller clearance reduces the wear rate dramatically, which corresponds to the former studies [42,71]. There is also a

transition value that mechanical wear and chemical wear alternatively dominate the total wear. Note that this transition for the head radius and clearance should vary with the change of the other relevant parameters such as normal force, angular velocity and passivation charge density.

From these predictions, it is clear that increasing the head radius and decreasing the clearance results in lower wear, which provide useful suggestions for the geometrical designing of artificial hip joints. It should also be noted that in the direction of decreasing the wear by large head radius and small clearance, the total wear is dominated by chemical wear, which shows the necessity to well understand and control the electrochemical conditions of MoM artificial hip joints in order to further reduce the wear by suppressing the chemical wear.
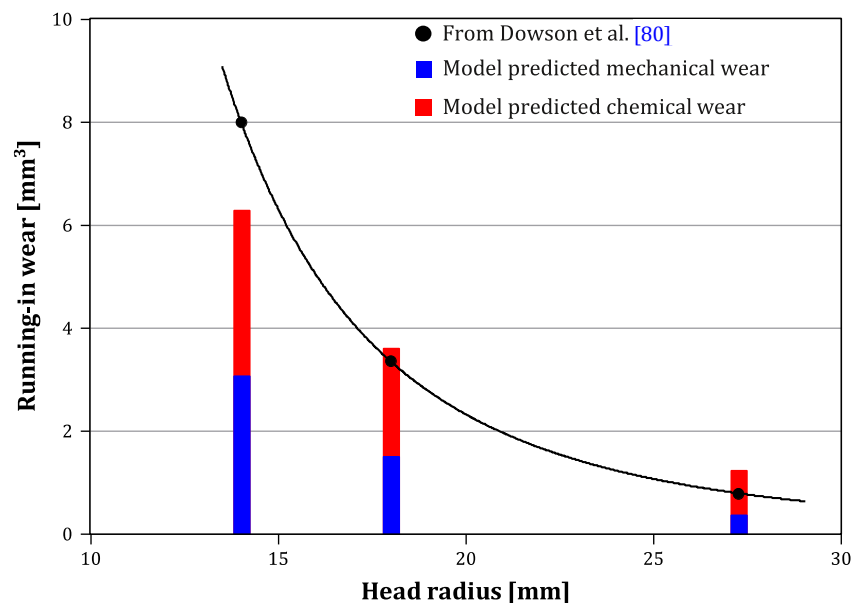
Figure 6.3 Experimental and model predicted running-in wear with the increase of head radius

Many studies demonstrate that using large head radius and small clearance can reduce the wear of MoM hip joints in simulators. As shown in Figure 6.3, Dowson et al. [80] measured under identical simulator conditions the running-in wear of MoM articulations with different head radius but very similar clearance. The model predictions (also shown in Figure 6.3) not only give the same trend between the running-in wear and head radius, but also match quite well the experimental absolute values. Using the model to predict the mechanical and chemical wear at each head radius, the model shows that the ratio between

chemical wear and mechanical wear increases with the increase of head radius from 1.1 at 14 mm to 1.4 at 18 mm and to 2.3 at 27.25 mm. Also, it can be seen from Figure 6.3 that chemical wear is relatively less affected by the head radius than mechanical wear and chemical wear dominates at large head radius.

Rieker et al. [42] carefully studied the simulator tested wear of a set of high carbon CoCrMo MoM articulations characterized by different head radii and clearances. They could observe, despite some result scattering, a certain proportionality between simulator running-in wear and clearance, as shown in Figure 6.4. The model was used to predict the running-in wear according to the experimental parameters in this study and the result is also shown in Figure 6.4.
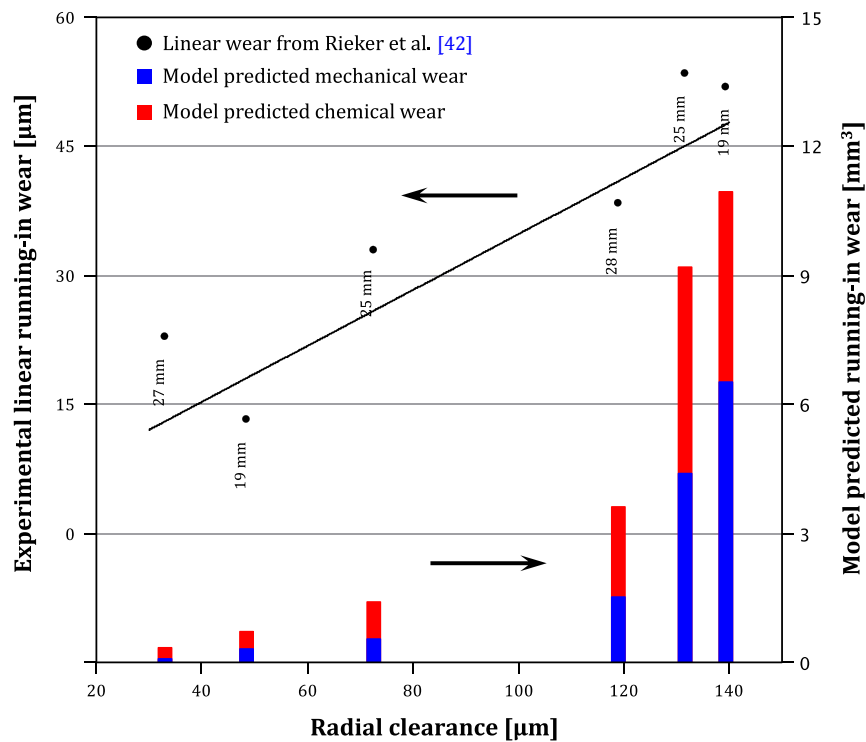
Figure 6.4 Experimental and model predicted running-in wear with the increase of radial clearance (values near the dots are the corresponding head radius)

Note that the wear was quantified by measuring the maximum linear wear in [42] while the model predicts volumetric wear values. Formulas have been proposed to relate linear wear with volumetric wear geometrically as reviewed by Ilchmann et al. [98]. These formulas consider uniform wear of the acetabular cup and offer the methods to estimate the volumetric wear from the penetration of the head into the cup obtained from radiographs. According to another study

[99], the ratio between the maximum linear wear in μm and wear volume in mm³ is approximately 6 in the case of high carbon CoCrMo MoM hip joints tested in simulators. However, this ratio calculated using the formulas in [98] is much smaller (0.2 to 1.5) since average linear wear is considered in these formulas. As shown in Figure 6.4, both the experimental and predicted values show comparable absolute wear values considering a ratio of 6 between the maximum linear wear in μm and wear volume in mm³ and a trend of higher running-in wear at larger clearances. No clear trend in the ratio between chemical to mechanical wear and clearance can be found in Figure 6.4. However, considering articulations of radius ranging from 25 to 28 mm which can be assumed similar head radius, one can observe that this ratio is 2.7, 1.5, 1.4 and 1.1 for radial clearances of 32.8, 72.4, 119 and 131 μm, respectively, i.e. chemical wear is more pronounced when clearance is smaller and chemical wear dominates the total wear at smaller clearance.

Figure 6.5 The variation of mechanical (blue line), chemical (red line) and total (green line) wear rate with normal force under hip joint simulator condition

Figure 6.5 shows the influence of normal force on the wear rate under simulator relevant conditions. It can be seen that both the mechanical and chemical wear rates increase with the increase of normal force, which can be explained by the larger contact pressure resulting in more severe plastic deformation of contacting asperities and reduction of hydrodynamic film

thickness. Interestingly, mechanical and chemical wear contribute in similar proportions to the overall wear. Note that the proportion varies with load, with chemical wear prevailing mainly at lower loads. However, for the total wear, above approximately 500 N, it varies nearly linearly with the normal load.

Figure 6.6 shows that velocity has little effect on the mechanical wear but great influence on the chemical wear. High velocity increases the hydrodynamic film thickness, alleviating the plastic deformation of the asperities, but it also increases the sliding distance per unit time, increasing the amount of material degradation. In the case of mechanical wear, these two effects compensate each other while in the case of chemical wear, lubrication can only compensate part of the increasing depassivation rate caused by the raising velocity, inducing larger chemical wear at higher velocity.

(b)

Figure 6.6 The variation of mechanical (blue line), chemical (red line) and total (green line) wear rate with angular velocity under hip joint simulator condition

The difference of surface hardness of the CoCrMo alloys can be due to the microstructures, carbon contents and heat treatments. Work hardening has been reported dramatically increasing the surface hardness of CoCrMo alloys, up to 50% depending on the different conditions in tribometer tribocorrosion studies. Figure 6.7 gives the effect of surface hardness on the wear rate of MoM hip joints, which shows that with the increase of surface hardness, both of mechanical and chemical wear decrease, however, the influence is less significant than the other parameters considering a surface hardness ranging from 300 to 900 HV.
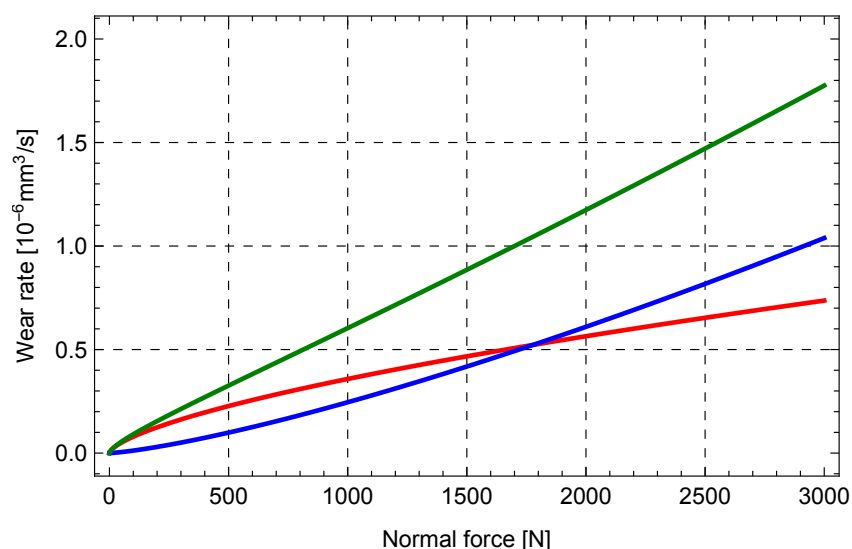
Figure 6.7 The variation of mechanical (blue line), chemical (red line) and total (green line) wear rate with surface hardness under hip joint simulator condition

Viscosity and passivation charge density are patients' health state and physical condition dependent. The effects of these two parameters are shown in Figure 6.8 and Figure 6.9.

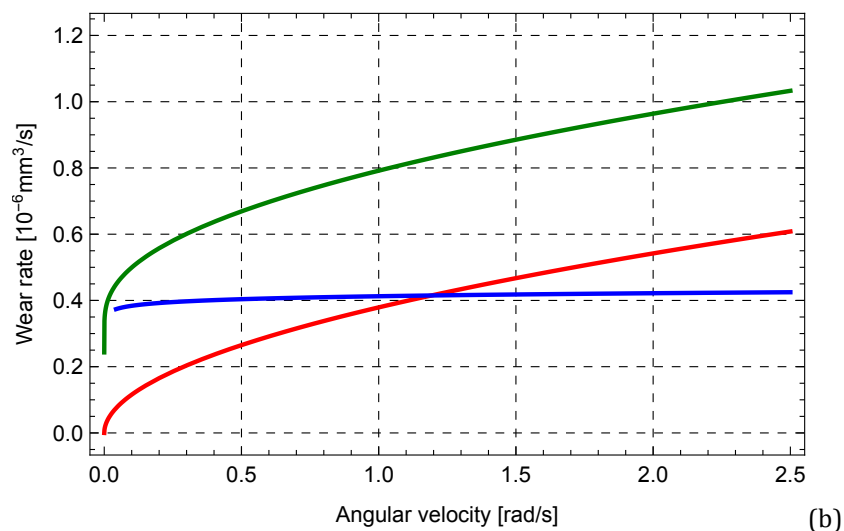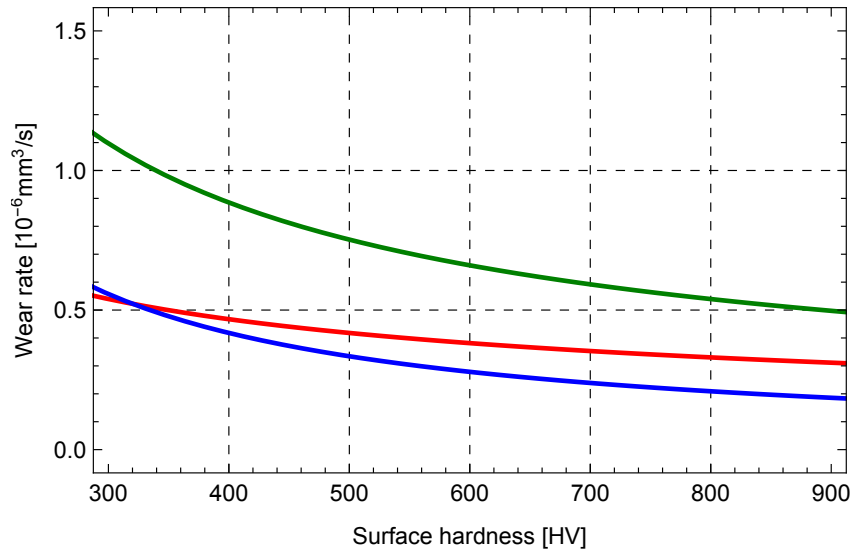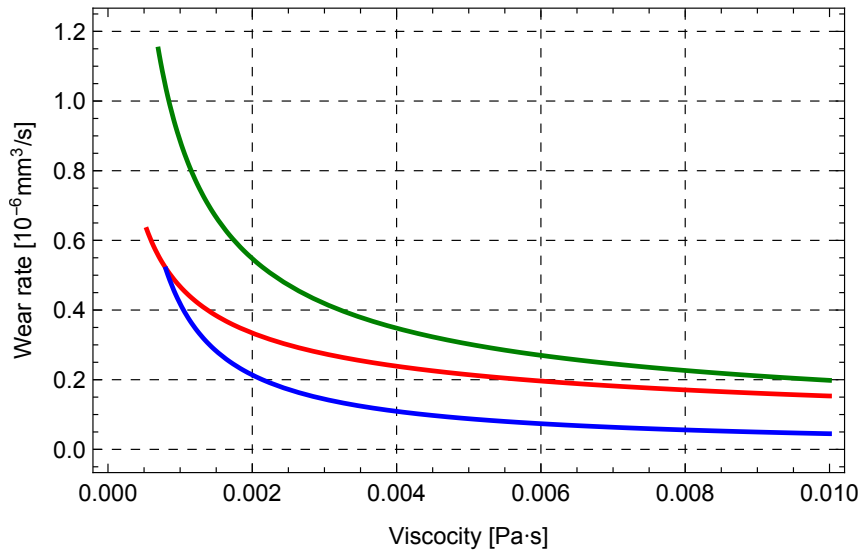**Figure 6.8** The variation of mechanical (blue line), chemical (red line) and total (green line) wear rate with viscosity under hip joint simulator condition
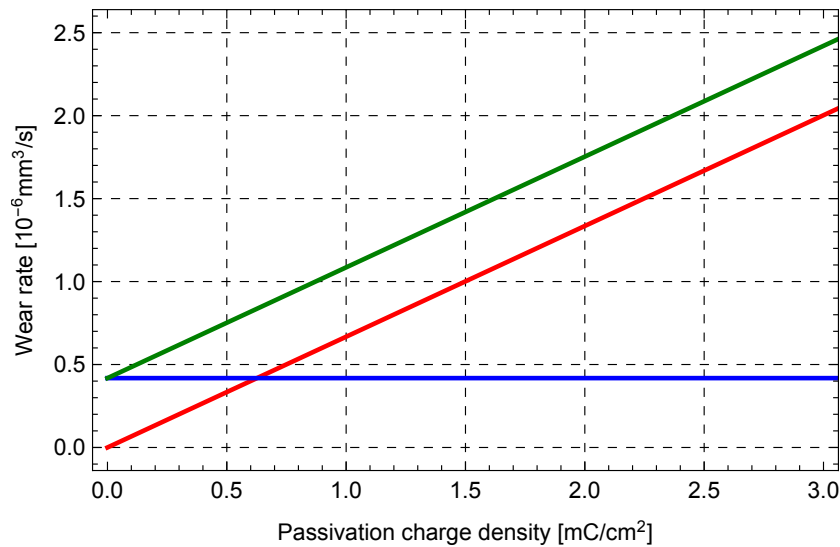
Figure 6.9 The variation of mechanical (blue line), chemical (red line) and total (green line) wear rate with passivation charge density under hip joint simulator condition

As can be seen in Figure 6.8, increasing the viscosity effectively reduces both of the mechanical and chemical wear due to the improvement of lubrication. Passivation charge density only affects chemical wear and according to the model, chemical wear is linearly proportional to the passivation charge density, as shown in Figure 6.9. Thus, when the passivation charge density is small (in this case, lower than 0.6 mC/cm^2), the chemical wear is less pronounced than mechanical wear. However, when the passivation charge density is higher, mechanical wear is much smaller than chemical wear.

It should be noted that normal force, angular velocity, viscosity, passivation charge density are all patient dependent parameters. The values of these parameters are not designable in artificial hip joints such as the head radius and clearance. However, the model can be used to provide suggestions to the selection of the hip implants and to the maintenance of the implants. For example, for the patients who are over weight, the wear rate of MoM hip joint is relatively high comparing to normal weight people. Thus, the lifetime of the artificial hip joint can be limited. Smaller clearance can be considered to reduce the contact pressure. It should be well considered before the surgery and after implantation, it is recommended to avoid running or starting and stopping walking suddenly in order to reduce wear from extra loading. As another example, the patients who are relatively sensitive to implants and the environmental conditions of implants are not recommended to receive MoM hip

implants since more inflammation could occur around the implants. Inflammation has been found to influence the electrochemical state of the implants [95], which causes the increase of the passivation charge density, significantly accelerating the chemical wear of the MoM hip joints. In this case, if the patients receive hip implants, they may have to be relied on anti-inflammation drugs.

6.3   Wear rate predictions for different material couplings

CoCrMo alloys can be used in hip joints as self-mated articulations (MoM joints) or in contact with polymer cup such as UHMWPE (MoP joints) or ceramics such as alumina (CoM joints). The model was therefore applied to such contacts in order to evaluate the degradation of the CoCrMo alloys in different material couplings. Note that in the case of MoP joints, wear of the UHMWPE is much larger than that of the metal and determines the lifetime of the implant, while the wear and corrosion of the metals is usually not the key problem. Even the applicability of Dowson's empirical correlation for MoP condition is not yet been checked, the concept of Dowson's correlation that the lubricating film reducing the extent of plastic deformation of the materials and thus wear is valid. Here it is just aimed to have a comparable idea about the amount of wear of the metal in different articulations.

The default values of the parameters concerning the CoCrMo alloys and calf serum solution mentioned in the previous section were used for calculation in combination with Young's moduli of 1 GPa and 350 GPa and Poisson's ratios of 0.4 and 0.22 for UHMWPE and alumina, respectively. The calculated mechanical, chemical and total wear rates are listed in Table 6.2.

Table 6.2 Wear rates of CoCrMo alloy in artificial hip joints with different material couplings
(R=18 mm, c_R=30 μm)

Material coupling	Wear rate of the CoCrMo alloy [mm³/Million cycle]		
	Mechanical	Chemical	Total
MoP	0.011	0.106	0.117
MoM	0.239	0.503	0.742
CoM	0.262	0.526	0.788

Not surprisingly, the model predicts lower wear rates of CoCrMo alloy for the MoP articulation due to the lower contact pressure and the higher hydrodynamic fluid film (Equation (2.7)). For the same reason, wear appears slightly more elevated in CoM comparing to MoM. Interestingly, in the MoP contact, chemical wear dominates (90% of) the overall wear, while its contribution is less (67%) in MoM and CoM contacts.

The estimated wear of CoCrMo alloy in the MoP contact constitutes most likely an upper limit. Indeed, due to the large compliance of the polymer, the contact pressure is eliminated because of the increase of contact area. Then, the local pressure on asperities may become very small and, depending on local contact pressure, lower than the critical threshold needed for plastic deformation of the CoCrMo alloy. Diomidis et al. [17] reported the existence of such a threshold for Ti alloys at approximately 20 MPa. Metal asperities loaded below the critical threshold are not expected to further contribute to wear and depassivation. In this case, the number of the asperities loaded above the critical threshold may decrease, resulting in less plastic deformation of the contacting asperities. However, the model does not contemplate a critical pressure threshold and therefore likely overestimates wear of the CoCrMo alloy in the MoP contact.

6.4 Conclusion

(1) The model provides a very useful method to predict the instantaneous wear rates of MoM artificial hip joints featured by varying normal load and sliding velocity during one gait cycle.

(2) The model predicted accurately the effect of head radius and radial clearance on the wear as measured in literature. The model shows that wear accelerated corrosion (chemical wear) dominates metal degradation of MoM hip joints at larger head radii and smaller clearances.

(3) The model offers the possibility to evaluate the effect of all the involved parameters, which give very useful tutorial suggestions about how to select the materials and optimize the designs in order to reduce wear.

(4) The model also allows predicting the wear of CoCrMo alloys used in the

MoP and CoM type artificial hip joints.

(5) According to the model, both mechanical and chemical wear significantly contribute to artificial hip joint degradation. Thus, predictions based on only one mechanism likely lead to erroneous conclusions. This is for example the case of head radius that has a significant effect on mechanical wear while little affects chemical wear. The other example is that the model predicts wear of MoM hip joints occurring also during the swing phase of a single gait cycle and this is because of the large contribution of chemical wear.

Chapter 7   Describing the effective normal force as a function of surface topography

In the previous chapters, a composite model was developed based on the tribocorrosion model and integrating the lubrication effect, which predicts well the tribometer and hip joint simulator experimental results for CoCrMo alloys. However, the applicability of the composite model to various lubricated tribocorroison conditions and materials is limited by the empirical nature of Dowson's correlation. To overcome this limitation, mechanistic modeling will be attempted in this chapter based on the fraction of the asperity contact area (real contact area) to the total contact area, which determine the fraction of effective normal force to total normal force.

The calibration and validation of the model will need dedicated experimental results. So, this chapter will start from a systematic tribocorrosion experimental study in different lubrication conditions.

7.1   Tribocorrosion experiments in H_2SO_4 – glycerol mixed solutions of different viscosities

Tribocorrosion experiments of a CoCrMo alloy were carried out in a tribometer using ball-on-disk reciprocating configuration. To obtain a higher hydrodynamic film thickness in mixed lubrication regime in order to increase the lubrication effect, an effective way is increasing the viscosity of the aqueous solution. The method used in this study is mixing H_2SO_4 aqueous solution with glycerol which has a very high viscosity (three orders of magnitude higher than that of water). Then, the viscosity of the mixed solutions can be modified by changing the concentration of the glycerol in the mixed solution in order to obtain a large range of hydrodynamic film thickness.

7.1.1 Experimental

Materials and solutions

The same CoCrMo alloy described in [30] was used in these experiments. This is a HC (high carbon) CoCrMo alloy and the composition fulfills the requirement of standards for hip implants (ASTM F1537 or F75). The microstructure of the alloy has also been described in [30]. The grain size of the metallic phase varies from 1 to 10 μm and the carbides have a large size distribution from sub-micrometers up to 5 μm. The volume fraction of the carbides is approximately 10%. The Young's modulus and Poisson's ratio are 248 GPa and 0.3 respectively according to the manufacturer.

The CoCrMo alloy samples were cut from a bar into disks of 24 mm in diameter and with a thickness of 5 mm. Then, the samples were polished and ultrasonically cleaned using the same method described in section 4.1.1.

For the ball-on-disk configuration, the counterpart for the CoCrMo alloy disk is an alumina ball with a diameter of 6 mm. According to the supplier (from SWIP AG Brugg), the purity of Al_2O_3 is 99.8 % and the surface roughness (R_a) is maximum 0.02 μm. The Young's modulus and Poisson's ratio are 350 GPa and 0.22, respectively.

The solutions used acting as both electrolyte and lubricant were mixture of 0.5 M H_2SO_4 solution and glycerol with volume percentage of the glycerol at 0%, 40%, 60%, 80% and 95%. 0.5 M H_2SO_4 solution was firstly prepared using a 95-97% pure H_2SO_4 (from Merck) diluted using distilled water and then mixed with anhydrous glycerol (from Sigma) at different volume fractions. The viscosity of the solutions was measured at room temperature (22±1°C) using a viscometer (Model RI:1:L from Rheology International Shannon, Ireland).

Tribocorrosion tests

The tribocorrosion experiments were carried out in a home made tribometer, which has been used and described in tribocorrosion studies for many times [26,29,31,58,100]. Figure 7.1 shows the main components of the tribometer. The CoCrMo alloy disk acting as working electrode is fixed by the cell made of PMMA. In the middle of the cell, a hole with a smaller diameter (18 mm

in these tests) than that of the samples is made in order to let a certain area of the topside of the sample expose to the solution. The bottom side of the sample is attached to a copper disk connected to the working electrode wire from the potentiostat. The alumina ball is fixed to a steel pin and a polymer cap was used to insulate the steel pin from the solution. Then the pin is fixed to the driving arm that transfers the linear movements generated by the linear motor (from ETEL SA) to the alumina ball. The load can be applied on the driving arm right above the pin and then the real load applied to the metal disk is measured using a force meter in order to obtain the total weight including the driving arm and the pin. It can be seen that, in the cell, the samples including the metal disk and the alumina ball are well electrically insulated from other metallic parts to avoid galvanic coupling.
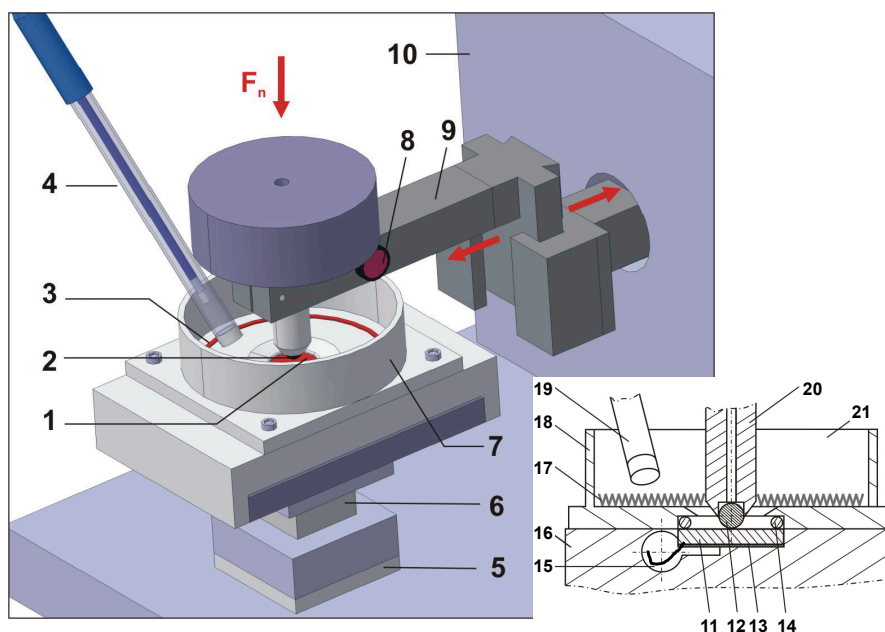
Figure 7.1 Schematic of the tribometer incorporated with electrochemical set-ups
(1. metal sample-working electrode, 2. alumina ball, 3. counter electrode, 4. reference electrode, 5. electrical insulating block, 6. three-axe force transducer, 7. PMMA cell, 8. laser, 9. driving arm, 10. linear motor, 11. metal sample-working electrode, 12. alumina ball, 13. copper contact plate, 14. O-ring, 15. connecting wire between working electrode and potentiostat, 16. cell bottom part, 17. counter electrode, 18. PMMA cell, 19. reference electrode, 20. ball holder, 21. electrolyte) [58]

A three-electrode system is mounted to the cell in order to apply and measure the potential and current. The disk sample works as working electrode

and a circular coil made of platinum is put around the round disk sample inside the cell as counter electrode. Then a reference electrode which is a standard mercury sulfate electrode (MSE) with a standard potential of 0.654 V with respect to the standard hydrogen electrode (SHE) is placed close to the sample on one side of the moving arm. The three electrodes are connected to a Wenking LB 95 L laboratory potentiostat (from Bank. GmbH).

There are mainly three couples of signals need to be measured. The first couple is the normal force and frictional force measured by the three-axe transducer (Kistler 9251A, two of the three axes are connected for measuring normal force and frictional force) and then the signals are transmitted to a data acquisition card (PCIE 6351 from National Instruments) in the computer. The second couple is the displacements in X direction (sliding direction) and in Z direction (normal direction) measured by the movement of the laser mounted in the arm. Then, the signals are also transmitted to the data acquisition card. The displacements in the X and Z direction represent the stroke length and the indentation of the ball, respectively. The third couple of the signals are the applied electrode potential and current measured by the potentiostat. These two signals are transmitted from the potentiostat to the data acquisition card, too. The data acquisition card is connected to a computer and the LabVIEW software is installed in the computer to do experimental control and simultaneous recording of the signals. The frequency of the data acquisition is 1 kHz, which means the measurement of the values for the normal force, frictional force, X direction displacement, Z direction indentation, applied potential and measured current was done every 1 ms. Meanwhile, the instant values of normal force, frictional force, Z direction indentation and applied potential in the middle of the stroke and the average value during one cycle of the current as well as the calculated X direction displacement were obtained to give the average values of these parameters every cycle during the whole test.

In this study, the reciprocating movement of the ball was realized by sending a signal from the computer to the motor controller and then to the motor. The sliding distance was 5 mm and the frequency of the rubbing was 1 Hz with a dwell time of 0.25 s after each stroke, which means the sliding velocity is 20 mm/s. The applied load was 5.6 N and the potential applied during the

tribocorrosion tests was 0 V_{MSE} which lies in the passive domain of the CoCrMo alloy for all the considered solutions.

The mounted samples were firstly cathodic cleaned at -1.5 V_{MSE} for 1 minute and then stayed at OCP for 5 minutes before applying the passive potential. Then the passive potential was applied to passivate the sample and after 5 minutes, the reciprocating sliding was activated for 30 minutes with the passive potential applied. After sliding, the sample was kept at the passive potential for another 5 minutes and then cleaned with ethanol and acetone for 5 minutes, respectively. Every test was performed twice in order to check the reproducibility.

Electrochemical measurements

Polarization behavior was checked before the passivation charge density measurements and the potential applied in the tribocorrosion tests (0 V_{MSE}) was well located in the passive domain for all the solutions.

Both of the polarization behavior and passivation charge density measurements were done using the same method described in section 4.1. However, the exposed area of the samples is bigger, 18 mm in diameter, which results in 2.54 cm^2.

Characterization of worn surfaces

The 2D topography of wear tracks was observed under optical microscope (Leitz). A non-contact white light interferometer (GBS smartWLI) was used to characterize the 3D topography of the wear tracks, as shown in Figure 7.2. According to the manufacturer, the interferometer has a vertical resolution of 0.1 nm and lateral resolution of 1.3 μm. The area for each measurement is 1 mm × 0.7 mm.
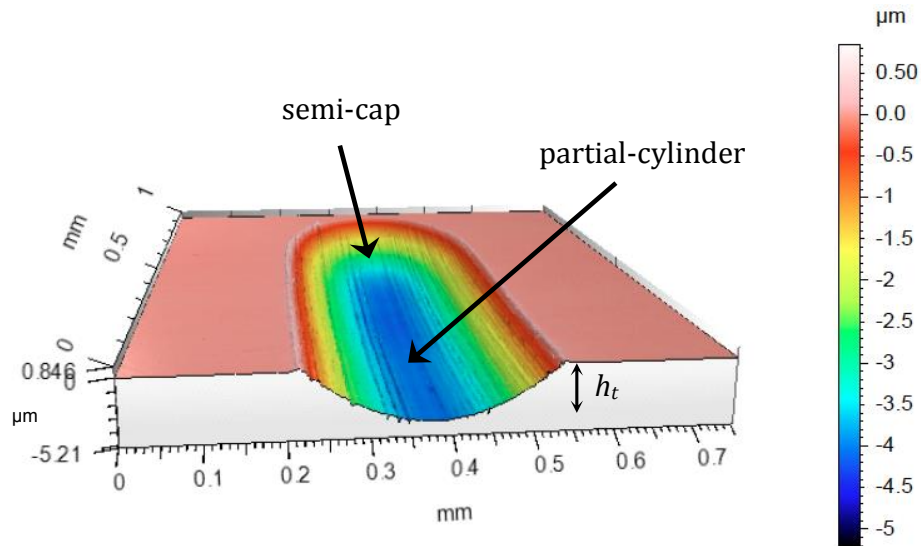
Figure 7.2 3D topography of the wear track

From the 3D topography, cross sections of the wear track perpendicular to the sliding direction on each sample can be obtained. The area of the wear track calculated from the cross section profile was calculated by subtracting the area below the baseline with the area above the baseline (set at the height of the non-rubbed surface). In this way only the material effectively removed from the sample was considered as wear. Five cross section profiles were measured from the wear track. The average value of the wear track areas from five profiles was used to multiply the length of the wear track (5 mm) in order to obtain the volume of the wear track (partial-cylinder part, as shown in Figure 7.2). In this case, the volume of the semi-caps at both ends of the wear track is not yet included. To calculate this volume, it is assumed that the two semi-caps are in perfect geometrical shape. The volume of the cap can be calculated using Equation (7.1):

$$U_{cap} = \frac{\pi}{3}(3R - h_t) \cdot h_t^{\,2} \tag{7.1}$$

where, R is the radius of the cap, in this case, it corresponds to the radius of the alumina ball (3 mm). h_t is the height of the cap which is the maximum depth of the wear track in the cross-section profile, as shown in Figure 7.2. The total wear volume is the sum of the partial-cylinder part and a whole cap.

Line profiles of the wear track can be obtained based on the 3D topography,

94

as shown an example in Figure 7.3. Three line profiles along the sliding direction and three line profiles perpendicular to the sliding direction were obtained. The length of the profiles along the sliding direction is fixed at 0.5 mm for all the samples. The length for the profiles perpendicular to the sliding direction is limited by the width of the wear track and was set a little smaller than the width of each specific wear track.

Then, the obtained line profiles were filtered using a certain cut-off length in order to remove the waviness and obtain the real profile for the asperity contacts. Due to the lateral resolution of the instrument which is 1.3 µm, the smallest cut-off length can be applied is 10 µm.
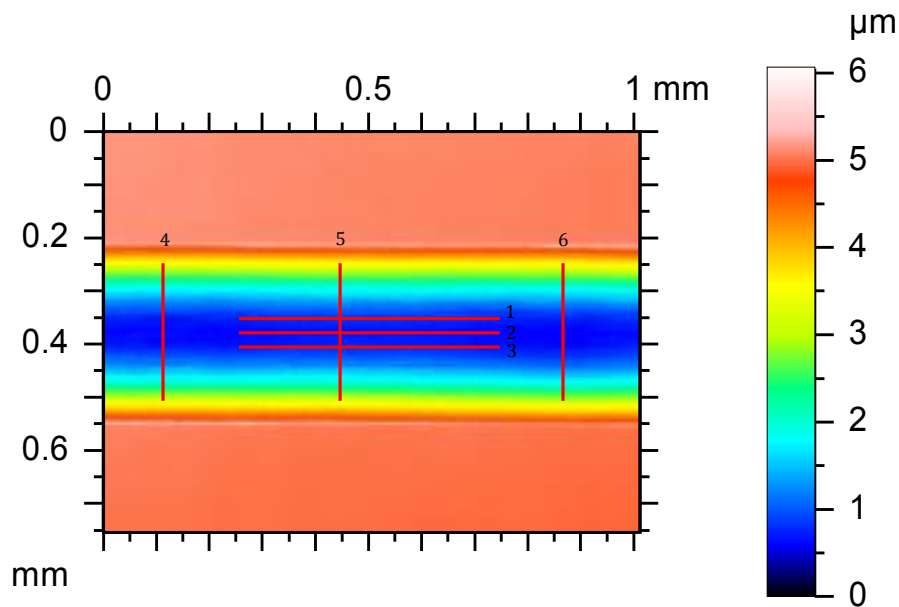
Figure 7.3 Extracting line profiles from the 3D topography of the wear track (sliding direction: left to right)

Micro-hardness was measured using a Vickers micro-hardness tester (Leitz) inside and outside the wear tracks. Average values were calculated from five individual tests. The applied load was 0.1 kg and the dwell time was 15 s.

7.1.2 Friction and wear results

Table 7.1 summarizes the friction, wear and surface hardness results measured or calculated from the experimental results. The coefficient of friction

(CoF) is the average of the values allover the rubbing time. Chemical wear is obtained by applying the integral of the excess anodic current during rubbing into Faraday's law.

Table 7.1 Summary of the results extracted from the tribocorrosion tests

Glycerol content [vol. %]	CoF	U_{track} $[10^{-3} mm^3]$	U_{chem} $[10^{-3} mm^3]$	U_{mech} $[10^{-3} mm^3]$	Hardness Inside [HV]	Hardness Outside [HV]
0	0.26 ± 0.01	4.67 ± 0.24	3.32	1.34	712 ± 21	475 ± 12
	0.30 ± 0.02	4.72 ± 0.15	3.32	1.40	745 ± 17	490 ± 8
40	0.29 ± 0.02	2.45± 0.05	1.61	0.84	678 ± 17	500 ± 6
	0.27 ± 0.02	2.64 ± 0.05	1.71	0.94	700 ± 23	492 ± 19
60	0.25 ± 0.01	1.10 ± 0.06	0.80	0.30	607 ± 21	494 ± 4
	0.24 ± 0.02	1.01 ± 0.07	0.74	0.27	638 ± 23	482 ± 22
80	0.16 ± 0.03	0.43 ± 0.03	0.31	0.12	613 ± 17	480 ± 7
	0.15 ± 0.02	0.48 ± 0.07	0.37	0.12	624 ± 21	489 ± 11
95	0.09 ± 0.01	0.05 ± 0.02	0.04	0.01	520± 19	468± 14
	0.11 ± 0.02	0.08 ± 0.01	0.06	0.02	559 ± 16	488 ± 16

In general, the coefficient of friction, anodic current and wear are reducing with the increase of the glycerol content, which shows the influence of lubrication. Figure 7.4 shows the variation of the friction coefficient and anodic current during the tests and optical microscope images of the wear surfaces after the tests. All of the tests showed clear depassivation at the onset of the sliding featured by the abrupt increase of the current and clear repassivation when the sliding stopped with the sudden decrease of the current. In 0.5 M H_2SO_4 solution where no glycerol was mixed, there is a relatively large fluctuation (between 0.25 and 0.35) of the friction coefficient (Figure 7.4(a)). This can be due to the severe plastic deformation of the CoCrMo alloy since the lubrication effect in this case is very small. Many fine scratches can be found on the wear surface along the sliding direction in Figure 7.4(b), which is probably from the abrasive wear from the asperities of the alumina ball or hard transfers of the metal to the alumina ball such as the carbides. However, it can also be seen that the areas between the scratches and even the inner surface of the scratches are relatively smooth.

(a)

(b)

(c)

(d)

(e)

(f)

(g)

(h)

(i)   (j)
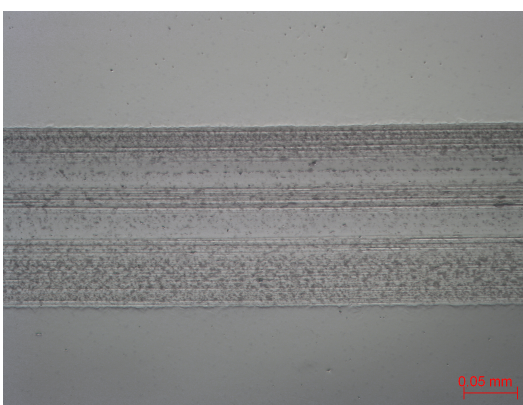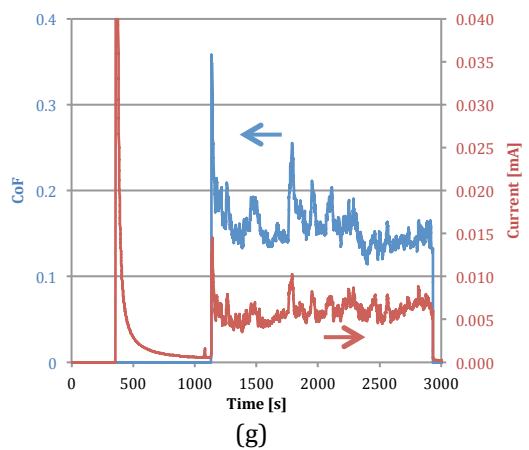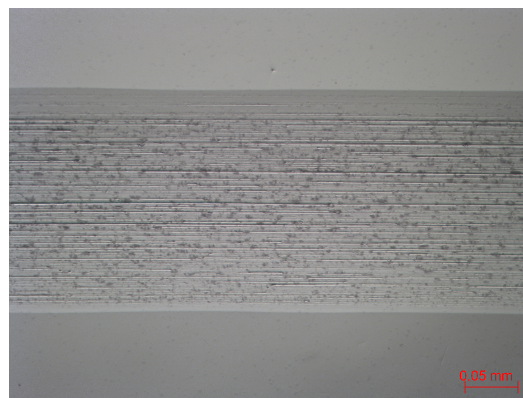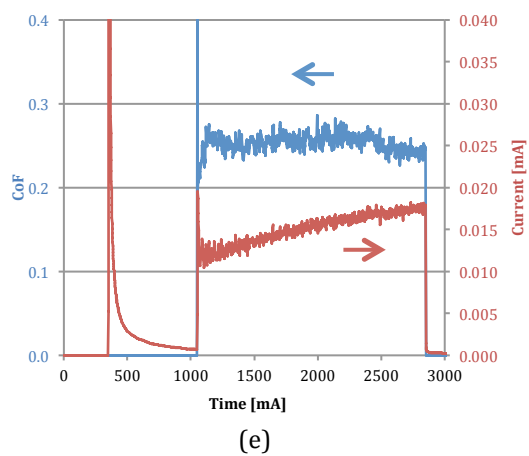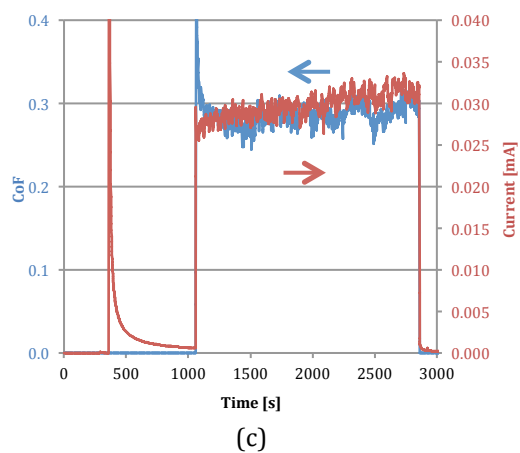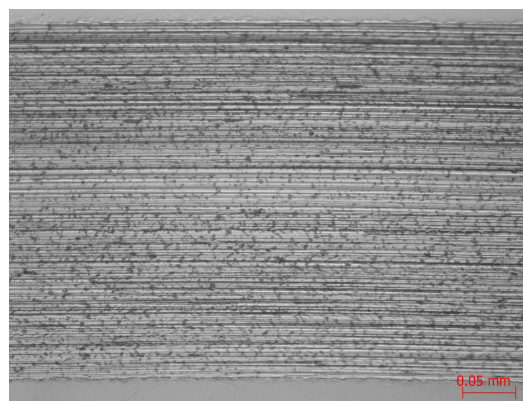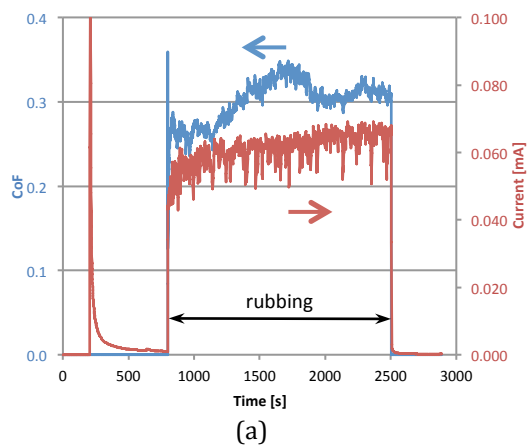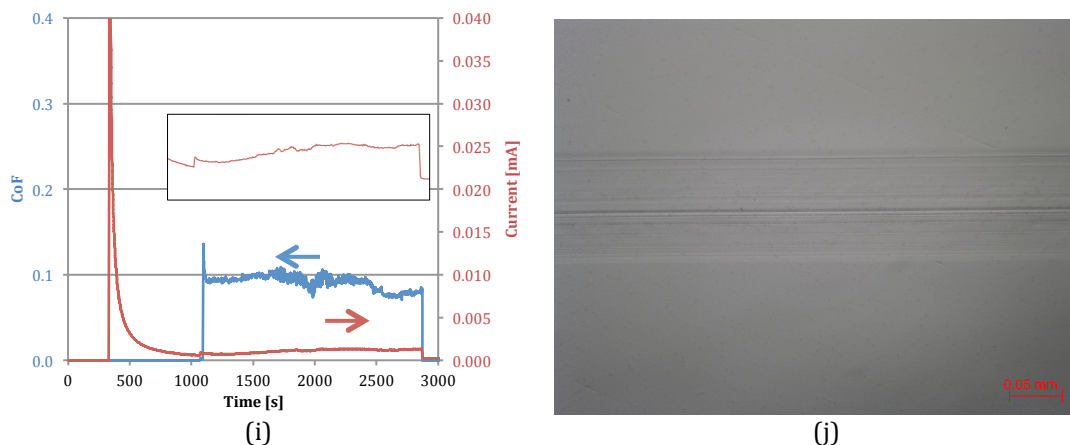
Figure 7.4 Coefficient of friction, anodic current and corresponding wear surface of the experiments in 0.5 M H_2SO_4 solutions with different glycerol contents

(a & b – 0 vol.% , c & d – 40 vol.%, e & f – 60vol.%, g & h – 80 vol.%, i & j – 95 vol.%)

The friction coefficients in solutions with 40% and 60% glycerol are more stable than that in H_2SO_4 solution without glycerol and much less scratches can be found in the wear track, which means the fraction of the smooth surfaces between the scratches is increasing.

Interestingly, when the glycerol content increases to 80%, the friction coefficient obtained is very low (around 1.5, only half of the one in H_2SO_4 solution without glycerol) but with big variation. Also, the current is fluctuating and follows quite well the variation of the friction coefficient. The reason for this variation is not clear. It can be due to the instability of the small fraction of contact undertaken by the contacting asperities. In sliding, the contacts pass from one asperity to another, inducing unstable friction between the counterparts. But it is found that the friction coefficient in solution with 95% glycerol is stable again, in which solution it is supposed to have even less fraction of asperity contacts than that with 80% glycerol. Another possibility is that the fluctuation of the friction is from the influence of the passive film generated on the surface of the CoCrMo alloy. When the wear is high, the friction is from the substrate since the passive film is very thin comparing to the thickness of the material removal. Then, the hydrodynamic film thickness is increasing with the increase of the glycerol concentration. As a result, wear is reduced that the material removal in one stroke can be very small. When the thickness of the removed material is close to the thickness of the passive film, the friction can be

98

influenced since in this condition the friction is from both the passive film and the substrate metal. This can be indicated by the small mechanical wear with 80 vol.% glycerol but negligible mechanical wear with 95 vol.% glycerol, which means the sliding probably only removes the passive layer at 95 vol.% glycerol content. So, when the material removal in one stroke is equal or less than the passive layer when the wear is small, the friction is mainly from the passive layer, which can also be quite stable. This is a plausible mechanism to explain the fluctuation of the friction coefficient. However, further studies are needed to verify this mechanism.

What is also interesting is the very low friction coefficient and very smooth wear surface found in the solution with 95% glycerol, as shown in Figure 7.4(i) and (j), which justify the effect of lubrication in reducing the plastic deformation of the CoCrMo alloy.

7.1.3 Passivation charge density

Figure 7.5 shows the current transients (from time 0 to 0.5 s) from the potential step measurements in the H_2SO_4 solutions with different glycerol contents. Except the one with 95% glycerol content, all the other curves show clearly an initial plateau followed by a decreasing part. The current in the plateau is clearly decreased with the increase of the glycerol content while the duration of the plateau is getting longer. It can be seen that the current already decreases to a very low value in the solutions with 0 vol.%, 40 vol.% and 60 vol.% glycerol content while still a relatively high value with 80 vol.% glycerol content and the current is just slightly decreased with 95 vol.% glycerol content.

It is as expected that the current values in the initial plateau part are reduced significantly, which is due to the dramatic increase of the resistance of the solution with the increase of the glycerol content. To check the resistance of the solutions, the conductivity κ of the solutions was measured using the CDM 210 conductivity meter (from MeterLab). Then, the conductivity can be converted to resistance. The results are shown in Table 7.2.
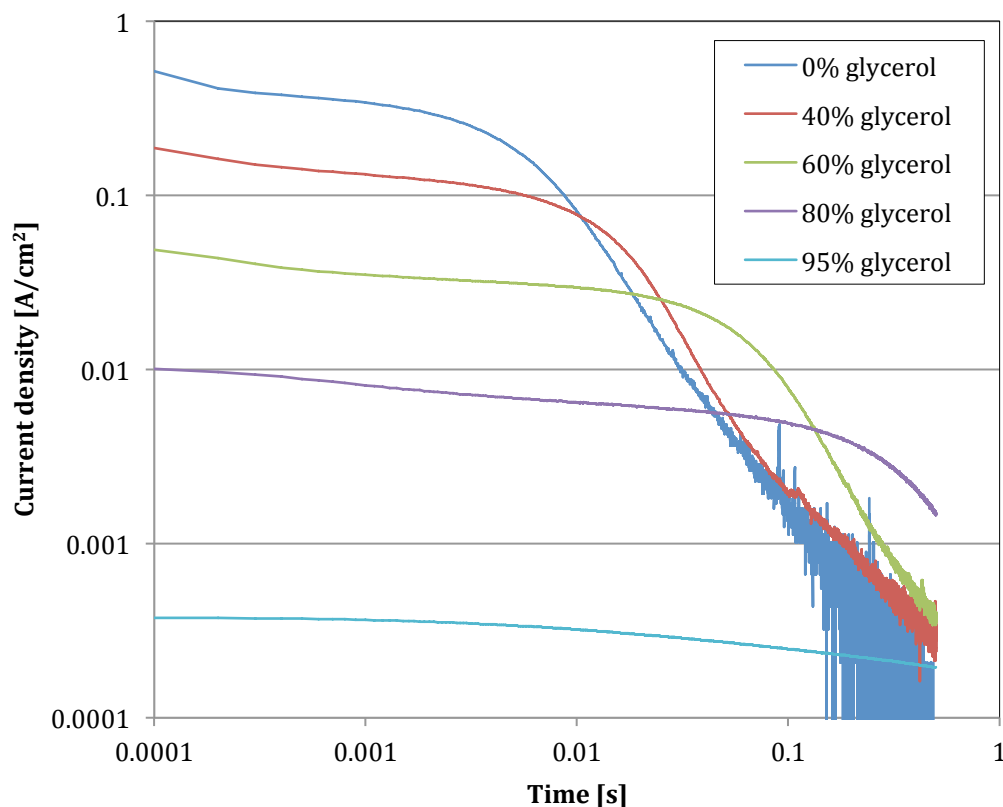
Figure 7.5 Current transients of the CoCrMo alloy from potential step tests in 0.5 M H_2SO_4 solutions with different glycerol contents (in logarithmic scale)

Table 7.2 Resistance of the H_2SO_4 – glycerol solutions

Solution		Resistance From	Resistance from
0.5 M H_2SO_4	Glycerol	CDM [$\Omega \cdot cm$]	impedance [Ω]
100 vol.%	0 vol.%	5±0.6	0.3±0.5
60 vol.%	40 vol.%	26±1.2	1.3±2.1
40 vol.%	60 vol.%	98±4.9	5.5±5.3
20 vol.%	80 vol.%	980±82	45±27
5 vol.%	95 vol.%	20000±1520	1050±493

Since the ohmic resistance of the solution between the working and reference electrode is reported highly dependent on the geometrical parameters such as the shape, area and distance between the working and reference electrode [26,59], the ohmic resistance of the solutions was also measured by electrochemical impedance using the Autolab PGSTAT 30 potentiostat with the same configuration used for the tribocorrosion experiments without alumina ball on the sample disk. The result is also shown in Table 7.2.

From Table 7.2, it can be seen that the resistance of the solution increased more than three orders of magnitude from H_2SO_4 solution without glycerol to 95 vol.% glycerol – H_2SO_4 solution, which correspond to the change of the plateau current in the current transients as shown in Figure 7.5.

In the reciprocating tribocorrosion experiments, the rubbing ball leaves behind a certain area of depassivated metal and this part of metal will be repassivated afterwards. It is clear that in each stroke the time left for the metal to be repassivated is different depending on the position of the depassivated area in the stroke. Considering a dwell time of 0.25 s at the end of each stroke, in one cycle, the average time for a certain depassivated spot to be repassivated is 0.5 s. So, the passivation charge density of the investigated CoCrMo alloy was calculated by integrating the current density from time 0 to 0.5 s for each solution, as shown the result in Table 7.3. The passivation charge density just decreases slightly from 0 vol.% to 40 vol.% glycerol content while decreases dramatically when the glycerol content is further increased.

Table 7.3 Passivation charge density for each solution calculated from the current transient

Solution		Passivation charge density [mC/cm²]
0.5 M H_2SO_4	**Glycerol**	
100 vol.%	0 vol.%	3.25±0.18
60 vol.%	40 vol.%	2.72±0.36
40 vol.%	60 vol.%	2.31±0.34
20 vol.%	80 vol.%	1.75±0.21
5 vol.%	95 vol.%	0.11±0.04

From this passivation study, it can be concluded that resistance of the solution is another factor other than applied potential which affects the passivation charge density of CoCrMo alloys. In the passivation charge density measurement in section 4.1, the resistance of the H_2SO_4, NaCl and calf serum solutions was also found different (5, 71, 36 Ω·cm, respectively) but close, at least in the same order of magnitude. No clear difference in the passivation charge density was found in these three solutions, as shown in Figure 4.5. This indicates that the influence of solution resistance on passivation charge density of CoCrMo alloys is little provided small difference in the resistance (at least

same order of magnitude). When there is a big difference in the resistance of the solutions (several orders of magnitude), passivation charge density can be significantly affected.

7.1.4 Viscosity of the solutions

In order to calculate the hydrodynamic film thickness, the viscosity of the solutions should be determined at different glycerol contents. The result is shown in Table 7.4, measured at room temperature (22±1 °C).

Table 7.4 Measured viscosity of the solutions

Solution		Measured viscosity
0.5 M H_2SO_4	Glycerol	[mPa·s]
100 vol.%	0 vol.%	1.16±0.41
60 vol.%	40 vol.%	4.98±0.63
40 vol.%	60 vol.%	14.82±1.76
20 vol.%	80 vol.%	80.5±6.4
5 vol.%	95 vol.%	511.4±19.2

It can be seen from Table 7.4 that the viscosity of the solution varies more than two orders of magnitude when different percentages of glycerol is mixed with the H_2SO_4 solution.

Actually, the viscosity of glycerol/water solutions at any concentration and at temperatures from 0 to 100 °C have been well studied [101,102]. The measured viscosities of the solutions in Table 7.4 correspond well to the literature values, which indicate that H_2SO_4 has little effect to the viscosity of the glycerol/water solution at this concentration (0.5 M).

7.1.5 Comparing the experimental results to model predictions

The experimental results were firstly compared to Dowson's correlation. The minimum hydrodynamic film thickness was calculated according to the Hamrock-Dowson Equation (2.7). Figure 7.6 shows the variation of the total wear rate and average coefficient of friction with the calculated minimum hydrodynamic film thickness.
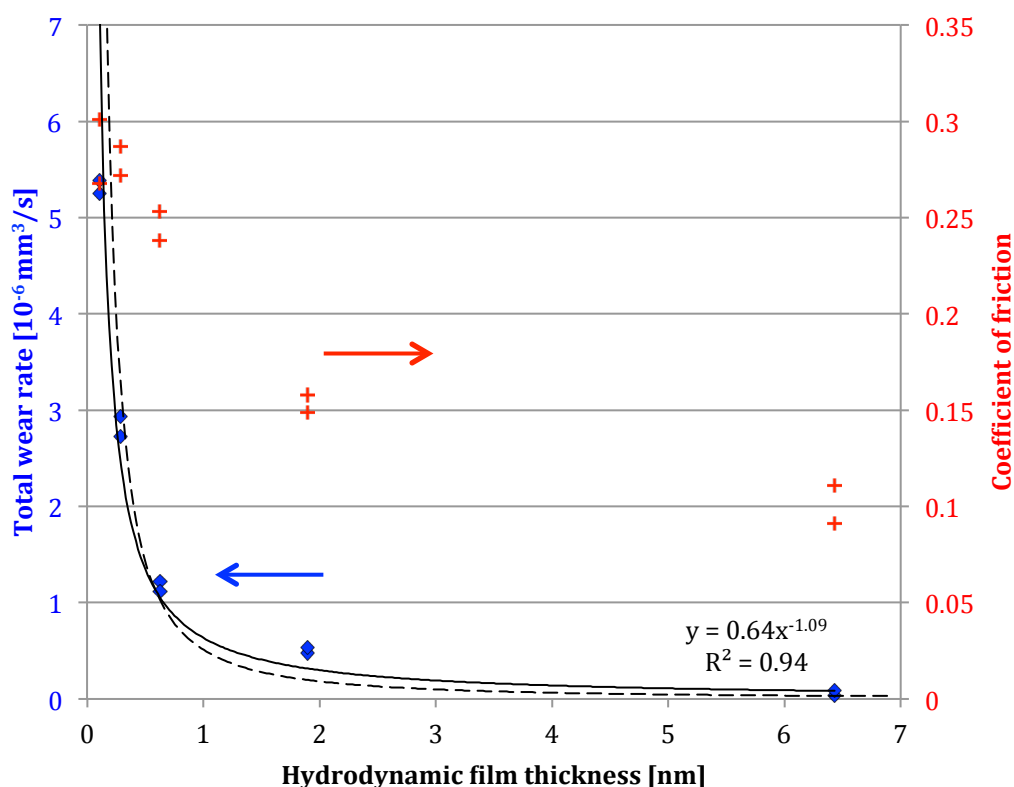
Figure 7.6 Experimental wear rate and coefficient of friction at different hydrodynamic film thickness (the solid line is the correlation of the wear rates obtained in these experiments and the dashed line is from Dowson's correlation)

It can be seen from Figure 7.6 that a hydrodynamic film thickness ranging from 0.1 nm to 6.4 nm had been achieved. Clearly, with the increase of the hydrodynamic film thickness by more than one order of magnitude, the coefficient of friction was reduced effectively from around 0.3 to 0.1. The gradual decrease of the friction coefficient, according to the Stribeck curve (Figure 2.9), indicates that mixed lubrication regime is prevailing in these tribocorrosion experiments.

Two tests were performed for each solution, which showed good reproducibility. As indicated by Dowson's correlation (Equation (2.9)), a power-type correlation was tried between the wear rates and the minimum hydrodynamic film thickness, as shown the solid line in Figure 7.6, and very good correlation was found. Different from Dowson's equation that shows the wear is inversely proportional to the minimum film thickness at a power of 1.49, the current experimental results show a lower power which is 1.09. The correlation with power 1.49 is also plotted in Figure 7.6 using dashed line. It can be seen that

the two correlation lines are quite close. Based on this, Dowson's correlation between wear and minimum hydrodynamic film thickness can also be confirmed for tribometer conditions.

It should be noted that Dowson's correlation was derived from simulator experimental results, which has large scattering due to the variety of the experimental conditions but covers a larger range of hydrodynamic film thickness (0 – 130 nm) [23]. The current experimental results were obtained under identical tribometer experimental conditions, which has much less scattering but covers a small range of hydrodynamic film thickness (0.1–6.4 nm). Surprisingly, very similar correlation was found between these two sets of data.

The experimental results can also be compared to the predictions made using the model developed in Chapter 3. The values used in the model prediction are shown in Table 7.5. Passivation charge density and viscosity of the five solutions have been measured and shown in Table 7.3 and 7.4. The micro-hardness and the wear volume can be extracted from Table 7.1 and the wear rates can be calculated by dividing the wear volume by the sliding time.

Table 7.5 Values for the parameters in the tribocorrosion tests

Parameter	Value
Materials	CoCrMo alloy (disc) and Al_2O_3 (ball)
E and v	E_1= 248 GPa, v_1=0.3, E_2= 350 GPa, v_2=0.22
Charge number (n)	2.37 (Co 2×63%, Cr 3×27% Mo 5×6%)
Molecular mass (M)	58.66 g/mol
Density (ρ)	8.33 g/cm^3
Faraday's constant (F)	96500 C/mol
Ball radius (R)	3 mm
Normal force (F_n)	5.6 N
Stroke length	5 mm
Frequency	1 Hz
Dwell time	0.25 s
Total testing time	1800 s
Sliding velocity (v_s)	20 mm/s

Figure 7.7 shows the results of the model predicted and experimental mechanical, chemical and total wear rates. It can be seen that generally the

model predicts relatively well the experimental results. The chemical wear rates are well predicted by the model. However, the error for the mechanical wear prediction is bigger. This can be due to the difference between the two correlations in Figure 7.6. The model used Dowson's correlation and due to this difference it is not surprising to find certain variation between the model predictions and experimental results. According to the model, mechanical wear is more influenced by this variation, since in the model the lubrication effect (power for the h_{min}) is much higher on mechanical wear (1.49) than on chemical wear (0.745), as shown in Equation (3.9). This can explain the bigger error for the mechanical wear than the chemical wear in Figure 7.7.
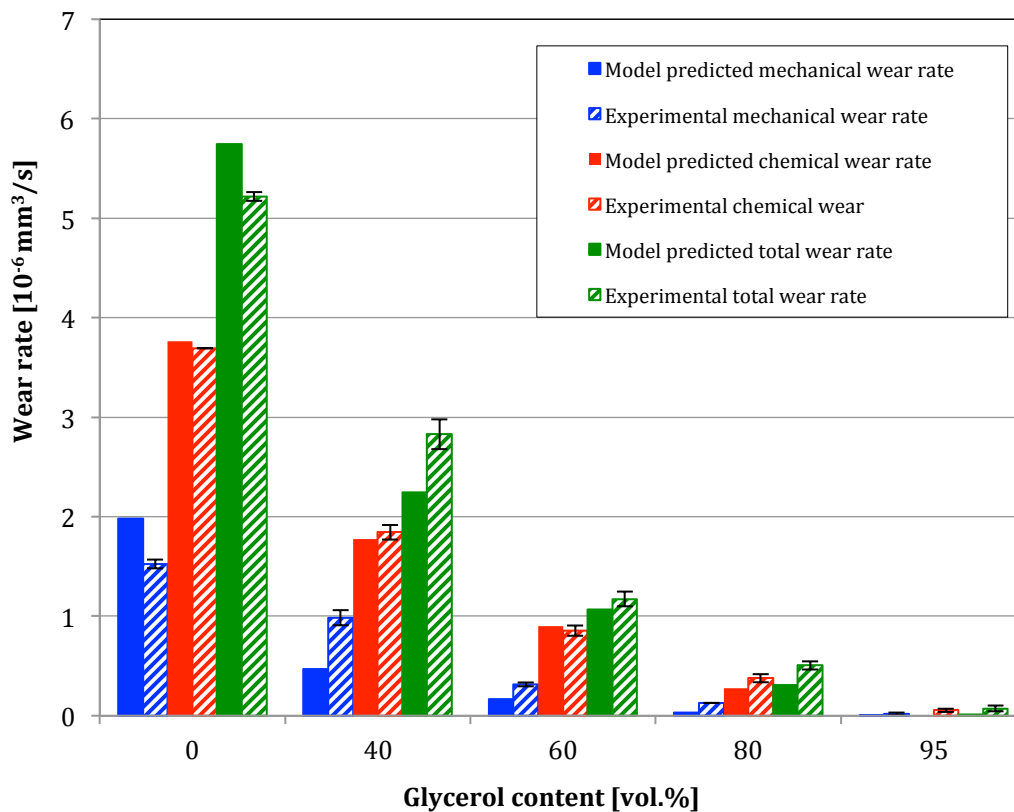

Figure 7.7 Comparison between model predicted and experimental mechanical, chemical and total wear rates at different glycerol contents

7.2   The effective normal force with respect to topography

In mixed lubrication regime, the total normal load applied to the contact is

carried by both the contacting asperities and lubricant between the asperity junctions, while only the load carried by the contacting asperities, which is called effective normal load or effective normal force (F_{eff}), causes plastic deformation of the counterparts and consequently induces wear. In other words, only the real contact area of the asperities is under plastic deformation and contributes to wear. So, the determination of the real contact area in mixed lubrication regime facilitates the way to determine effective normal force and consequently wear.

7.2.1 Real contact surface in mixed lubrication regime

During wear, the surface topography in the contact area is modified due to the plastic deformation of the materials. As an example shown in Figure 7.8, the CoCrMo alloy disk rubbed by an alumina ball shows many scratches and hills along the sliding direction. This is mainly due to the asperities or valleys on the counterpart alumina ball that is much harder than the CoCrMo alloy. It is easy to imagine that the hard alumina has little wear and the metal disk will be plastically deformed and copy the topography of the alumina ball surface in the wear track. For example, the asperities on the ball will scratch the alloy to form valleys on the disk and the valleys on the ball cause less wear of the disk to form hills. So, the wear surface will be generally conformal to the ball surface especially in the image plane perpendicular to the sliding direction. This explains why it is often observed that the line roughness perpendicular to the sliding direction is high but along the sliding direction the roughness is very small, as shown an example in Figure 7.8.

It should also be noted that in Figure 7.8, except the general topography (scratches, hills and flats), there is another finer topography locally on the surfaces of the scratches, hills and flats. If the two counterparts are getting conformal by creating asperity – scratch and valley – hill couplings, clearly the finer topography other than the conformal one is the asperities topography, which determines the real contact area. As a result, apparently it is not a correct way to take a wear surface profile from Figure 7.8 and intersect using a flat counterpart to determine the real contact surface.
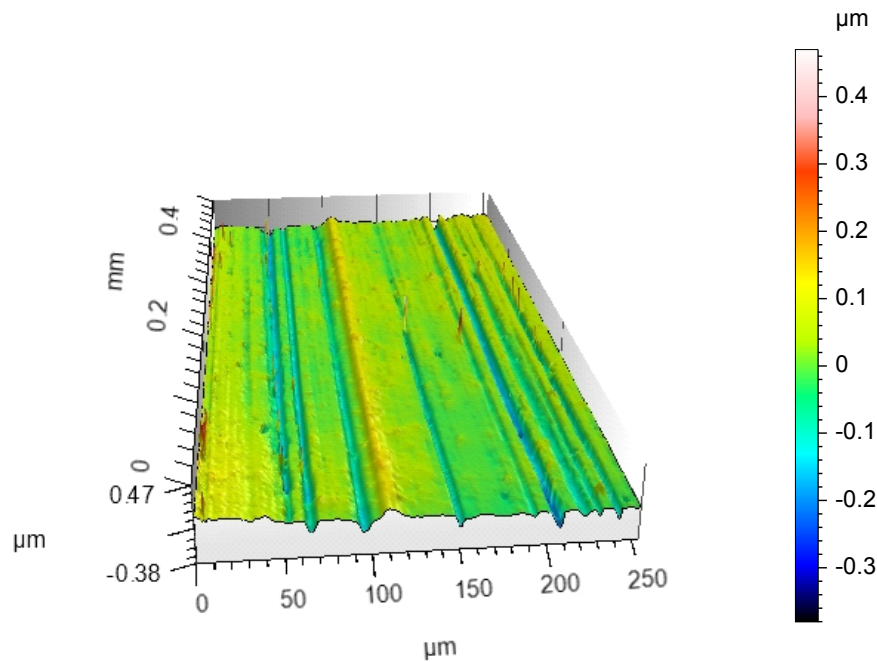
Figure 7.8 3D topography of a typical sliding wear surface (sliding direction: back to front)

Figure 7.9(a) shows a schematic of the contact between two counterparts taken perpendicular to the sliding direction. As described before, generally there are the conformal surfaces of the two counterparts and on these conformal surfaces, there are local asperities that are contacting, plastically deforming and generating wear.

Clearly, to obtain the real contact, the total contact in Figure 7.9(a) should be split into the conformal surfaces and the local asperity contact, as shown in Figure 7.9(b) and (c). After splitting, the conformal surfaces do not directly result in real contact but affect the extent of real contact by the separation of the two surfaces, which can be described by the hydrodynamic film thickness h in Figure 7.9(b). The local asperity contacts directly determine the real contact area, as shown in Figure 7.9(c). So, the real contact area depends on two factors: the surface profile of the local asperities and the separation between the two conformal surfaces.
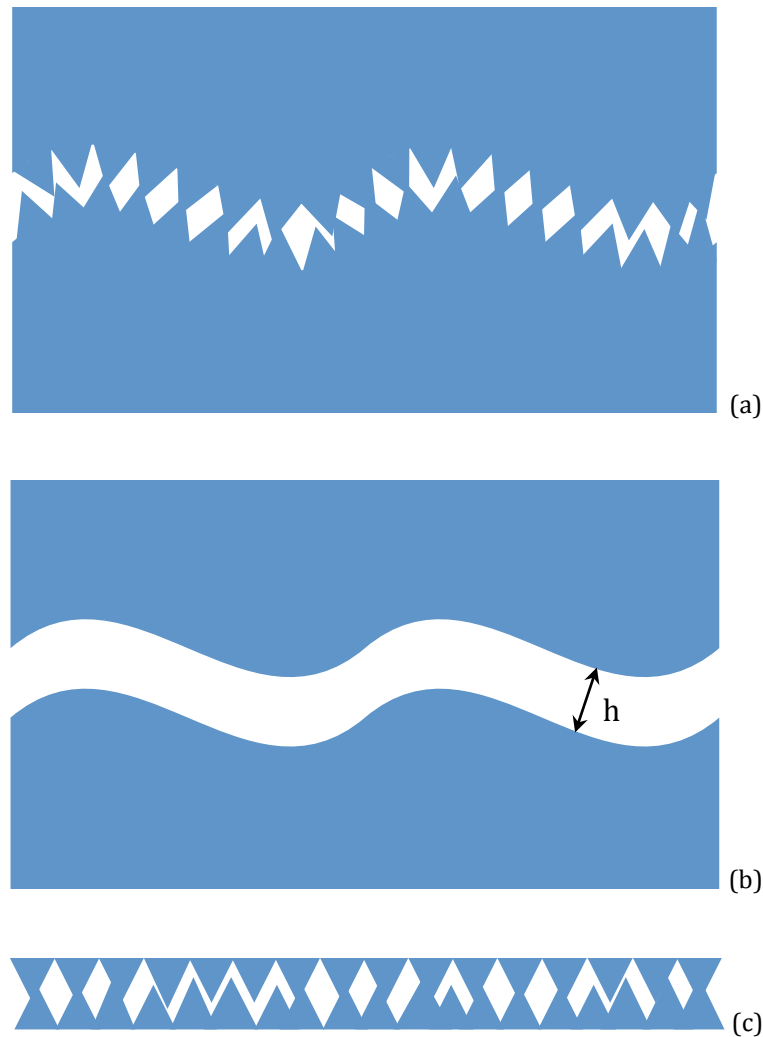
Figure 7.9 Schematics of the typical contact during wear taken perpendicular to the sliding direction (sliding direction: back to front): (a) total contact, (b) conformal surfaces without local asperities, (c) local asperity contacts without conformal surfaces

7.2.2 Effective normal force

Based on the contacting mechanism described in the previous section, in the asperity contacts (Figure 7.9c), the total normal force F_n applied to the total area is the sum of asperity contacts and lubricant occupied areas. The effective normal force F_{eff} is carried by the asperity contact (real contact area) and the difference between these two forces (F_n - F_{eff}) is the force carried by the lubricant. In the following, the topography (profile) of the asperity contacts (Figure7.9c) will be considered in order to determine the fraction of effective normal force to the total normal force in mixed lubricated condition.

Figure 7.10(a) shows a typical asperity profile. The lowest surface point is

set as 0 and the highest surface point is a, which means the variation of the surface profile is a. The real contacting level z is between 0 and a. There is no asperity contact (hydrodynamic lubrication) when z is higher than a, there is no lubricant in the contact when z is 0 (un-lubrication).
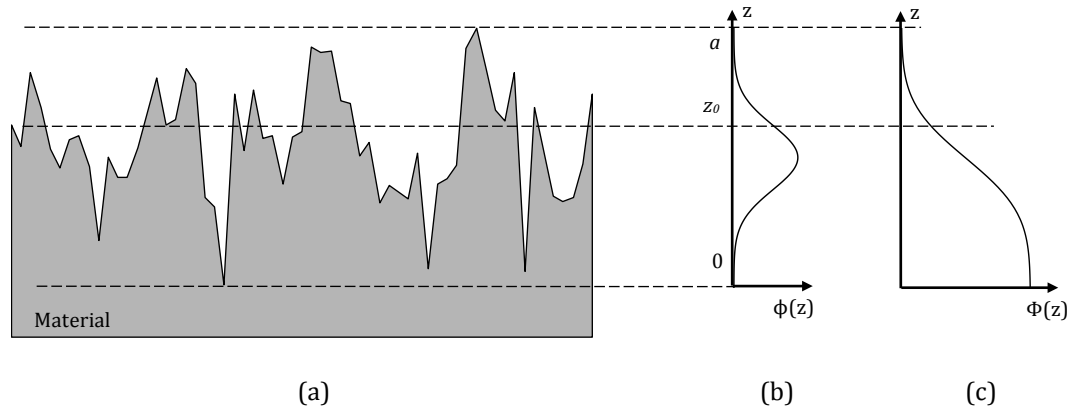
Figure 7.10 Schematics of a typical asperity profile (a), the probability curve (b) and the cumulative probability curve (c)

Figure 7.10 (b) and (c) show the probability curve and the cumulative probability curve from this distribution and from Figure 7.10(c), the fraction of the asperities contact area (real contact area) to the total contact area can be extracted from this curve (also called Abbott – Firestone curve) at a certain contacting level, e.g. z_0 in Figure 7.10.

Imagining a rigid smooth flat is sliding on the rough surface shown in Figure 7.10(a), due to the lubrication effect from the lubricant among the asperity conjunctions, the real contact between the flat and the rough surface is at level z_0. The asperities higher than level z_0 will be deformed in order to reach this level. In mixed lubricated contacts, the total effective normal force is the sum of many local effective forces from each of the contacting island (contacting asperity). If the contacting asperities are only under plastic deformation, the local effective normal force here is the force needed to plastically deform the initial asperity into a small flat area. The average stress allover these local asperity contacts corresponds to the plastic yield or hardness of the material. Thus, the total effective normal force is linearly proportional to the real contact area of asperities, the proportionality being the hardness of the material, as shown in Equation (7.2).

$$F_{eff} = HA_{real} \tag{7.2}$$

In lubricated condition, the effective normal force F_{eff} can only be equal or smaller than the total normal force F_n. From Equation (7.2), it can be seen that the effective normal force increases with the increase of the real asperity contact area. When the effective normal force reaches the total normal force, the real contact area here is defined as A_n, as shown in Equation (7.3). After that, the effective normal force doesn't increase any more.

$$F_n = HA_n \tag{7.3}$$

The real contact area can be determined from the Abbott – Firestone curve (cumulative probability curve) $\Phi(z)$, depending on the real contacting level z, as shown in Figure 7.11. When the separation is a, there is no asperity contact and with the decrease of the separation, the real contact area increases, thus the F_{eff} is increasing until the separation reaches z_n at which point the F_{eff} reaches F_n. From this point on, if the separation is smaller, all of the total normal load will be carried by the asperities. So, in mixed lubrication, the h should be added to this point (z_n) in order to get the real contacting level, as shown in Figure 7.11.
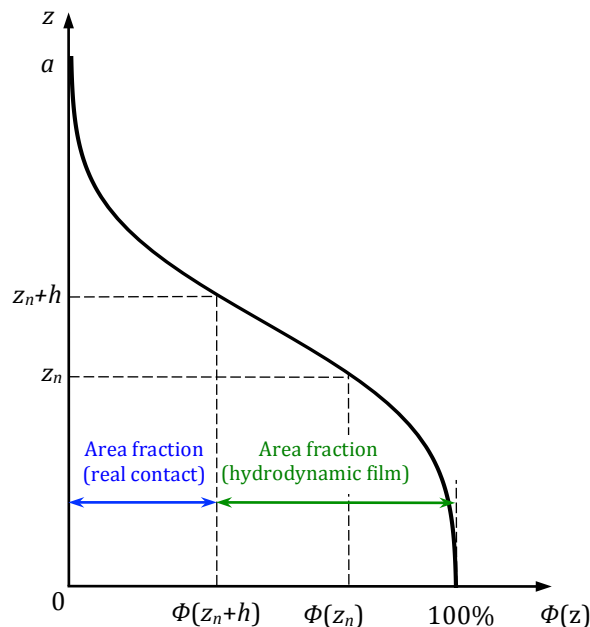
Figure 7.11 Determination of the fraction of the real contact area to the total area based on the Abbott – Firestone curve of the asperity profile

In Figure 7.11, when the separation z is 0, the total contact area A_{tot} equals to the Hertzian contact area as shown in Equation (7.4):

$$A_{tot} = \pi \left(\frac{3F_n R'}{4E'} \right)^{2/3} \tag{7.4}$$

Comparing A_n and A_{tot}, there are two possibilities: (1) When $A_n < A_{tot}$, the effective normal force reaches the total normal force before the real contact level reaches $z = 0$ in Figure 7.11. (2) When $A_n = A_{tot}$, the effective normal force reaches the total normal force exactly when the real contact level reaches $z = 0$.

From Figure 7.11, the real contact area and the contact area when F_{eff} reaches F_n can be related to the total contact area based on the Abbott – Firestone curve:

$$\frac{A_{real}}{A_{tot}} = \Phi(z_n + h) \tag{7.5}$$

$$\frac{A_n}{A_{tot}} = \Phi(z_n) \tag{7.6}$$

Combining Equation (7.2), (7.3), (7.5) and (7.6), one can obtain the ratio between effective normal force and total normal force:

$$\frac{F_{eff}}{F_n} = \frac{A_{real}}{A_{tot}} = \frac{\Phi(z_n + h)}{\Phi(z_n)} \tag{7.7}$$

From Equation (7.7), the model for effective normal force can be described in Equation (7.8):

$$F_{eff} = F_n \frac{\Phi(z_n + h)}{\Phi(z_n)} \tag{7.8}$$

Equation (7.8) relates the effective normal force to the total normal force based on the Abbott – Firestone curve of the asperity profile and the hydrodynamic film thickness. Here, z_n should be normal force, material, and asperity profile dependent.

In fact, z_n can be determined based on Equation (7.3), (7.4) and (7.6). According to Equation (7.3), at z_n, the real contact area of the asperities A_n is F_n/H. Incorporating this equation and Equation (7.4) into Equation (7.6), one can obtain:

$$\Phi(z_n) = \frac{F_n/H}{\pi\left(\frac{3F_nR'}{4E'}\right)^{2/3}} \tag{7.9}$$

If the Abbott – Firestone curve of the asperity profile is measured, z_n can be calculated according to Equation (7.9). Once z_n is obtained, the corresponding hydrodynamic film thickness h can be added to z_n and then $\Phi(z_n+h)$ can be determined from the Abbott – Firestone curve.

7.2.3 Integrating the new effective normal force model into the tribocorrosion model

As described in Section 3.1, the tribocorrosion model which didn't consider lubrication effect can be modified by replacing the total normal force used in the model by the effective normal force in order to integrate the lubrication effects, as shown in Equation (7.10):

$$V_{tot} = k_m \frac{F_{eff}}{H} v_s + k_c \frac{Q_pMv_s}{nF\rho}\left(\frac{F_{eff}}{H}\right)^{1/2} \tag{7.10}$$

Now, the new effective normal force F_{eff} obtained in the previous section can be incorporated into the lubricated tribocorrosion model (Equation (7.10)) to get the composite model in a new form, which is based totally on mechanistic approaches. The model is shown in Equation (7.11):

$$V_{tot} = k'_{mech} \frac{F_n}{H} v_s \frac{\Phi(z_n+h)}{\Phi(z_n)} + k'_{chem} \frac{Q_pMv_s}{nF\rho}\left(\frac{F_n}{H}\right)^{0.5}\left(\frac{\Phi(z_n+h)}{\Phi(z_n)}\right)^{0.5} \tag{7.11}$$

where, k'_{mech} is the mechanical wear factor and k'_{chem} is the chemical wear factor,. h is the hydrodynamic film thickness, $0 < h < a$, a is the maximum height of the surface asperities.

7.3   Comparing model predictions to experimental results

The new composite model is developed in the previous section based on the plastic deformation of contacting asperities and considering the real contact area geometry. The model validity will be assessed here by comparison with the

experimental results obtained in section 7.1.

In order to apply the model to these experimental results, except the parameters listed in Table 7.5, there are still two parameters z_n, h and the Abbott – Firestone curve of the asperity profile which need to be determined. Once the Abbott – Firestone curve is obtained, $\Phi(z_n)$ can be determined and z_n can be calculated using Equation (7.9). The hydrodynamic film thickness h can be estimated using the minimum hydrodynamic film thickness equation (2.7), which has been used in the previous chapters. So, the only work needs to be done before applying the model is the measurement of the asperity profiles

Since the wear surfaces usually do not follow a simple mathematical distribution [103] such as Gaussian distribution, it is not always possible to have an actual mathematical function for $\Phi(z)$. As a result, the Abbott – Firestone curve of the asperity profile has to be measured. Once the Abbott – Firestone curve for a profile is measured, one can easily obtain the value for $\Phi(z)$ at any z. The Abbott – Firestone curves of six line profiles on each sample inside the wear surfaces were obtained after the wear test, as shown in Figure 7.3. In order to use them, two hypotheses are made:

(1)   The surface profiles obtained from the wear surfaces after experiment is representative to the surface profiles under loading during experiment.

(2)   In the wear surface, removing the conformal surfaces (as shown in Figure 7.8b) that are the waviness in the profile, the distribution of the remaining asperities is uniform, which means no specific preference in different directions.

Based on these two hypotheses, the line profiles along the sliding direction can be used, as shown in Figure 7.12(a). The profiles were firstly filtered by applying a cut-off length of 10 μm in order to remove the conformal surfaces and obtain the profiles of the asperities (Figure 7.12(b)). Then, the Abbott – Firestone curve of the filtered profile can be obtained (Figure 7.12(c)). From the second hypothesis, it also can be deduced that the fraction of the real contact area $\Phi(z)$ obtained from the line profile equals to the value obtained from the surface profile.

(a)

(b)

(c)
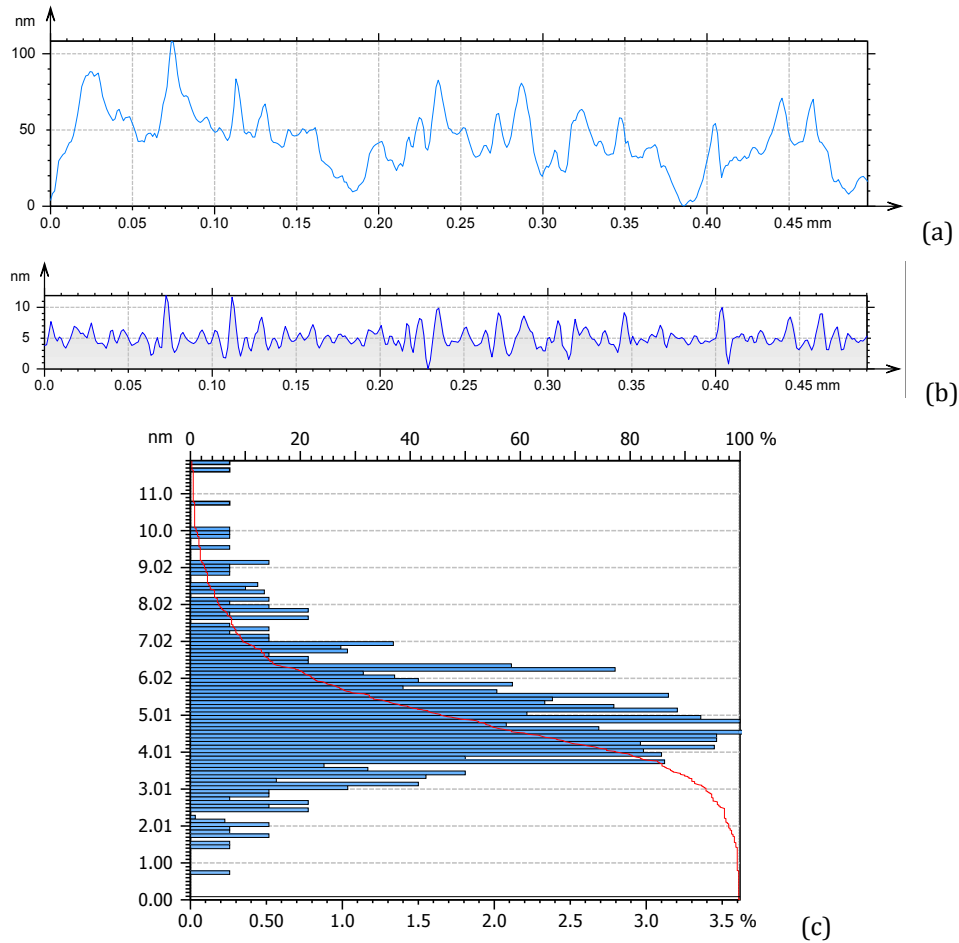
Figure 7.12 A Line profile from the wear surface tested in 60 vol.% glycerol content solution (a), the filtered profile (b) and the Abbott – Firestone curve of the filtered profile (c)

In order to obtain $\Phi(z_n)$, which is one of the values needed in the model (Equation (7.11)), the real contact area A_n when the effective normal force reaches the total normal force and the total contact area A_{tot} (Hertzian contact area) are required. The values for these two parameters for each test described in section 7.1 are shown in Table 7.6. From Equation (7.6), $\Phi(z_n)$ is the ratio between A_n and A_{tot}.

Once $\Phi(z_n)$ is determined, the value can be put into the Abbott – Firestone curve, as shown in Figure 7.12(c), in order to obtain the corresponding $z_{n,}$. Then, the corresponding calculated minimum hydrodynamic film thickness is added to z_n in order to find the real contact level (z_n+h_{min}) and from the Abbott – Firestone curve, the $\Phi(z_n+h_{min})$ can be determined.

Table 7.6 Summary of the contact area A_n and A_{tot} for each test

Glycerol content [vol. %]	A_n [10^{-3} mm^2]	A_{tot} [10^{-3} mm^2]	A_n/A_{tot}
0	0.787	4.469	17.6%
	0.752	4.469	16.8%
40	0.826	4.469	18.5%
	0.8	4.469	17.9%
60	0.923	4.469	20.6%
	0.878	4.469	19.6%
80	0.914	4.469	20.4%
	0.897	4.469	20.1%
95	1.077	4.469	24.1%
	1.002	4.469	22.4%

The values for the other parameters can be found in section 7.1. Figure 7.13 plots the mechanical and chemical wear rates with the variables from the experiments. The average values of $\Phi(z_n+h_{min})/\Phi(z_n)$ obtained from the three profiles for each sample were used in Figure 7.13 and the standard deviations were also plotted as error bars. It can be seen that the $\Phi(z_n+h_{min})/\Phi(z_n)$ values determined from the Abbott – Firestone curves from three line profiles have large scattering especially for the chemical wear due to the magnifying effect of the power 0.5 when considering the error in percentage. The scattering may be due to the low lateral resolution of the profilometer used (0.1 μm).

It can be seen from Figure 7.13 that the experimental results obtained in H_2SO_4 without glycerol are a little higher than the general trend from the other data points. If the four data points from this solution are omitted, the other data points follows quite well linear correlation, which indicates a possible effect from the glycerol on the wear property of the CoCrMo alloys in H_2SO_4 solution. The reason can be the absorption of the glycerol organic molecules on the wear surface to generate a boundary film below the lubricating film. However, this boundary film is not yet considered in the model.

Nevertheless, the correlations in Figure 7.13 are not bad and the trends are clearly there, which shows the model approach is promising.

(a)

(b)
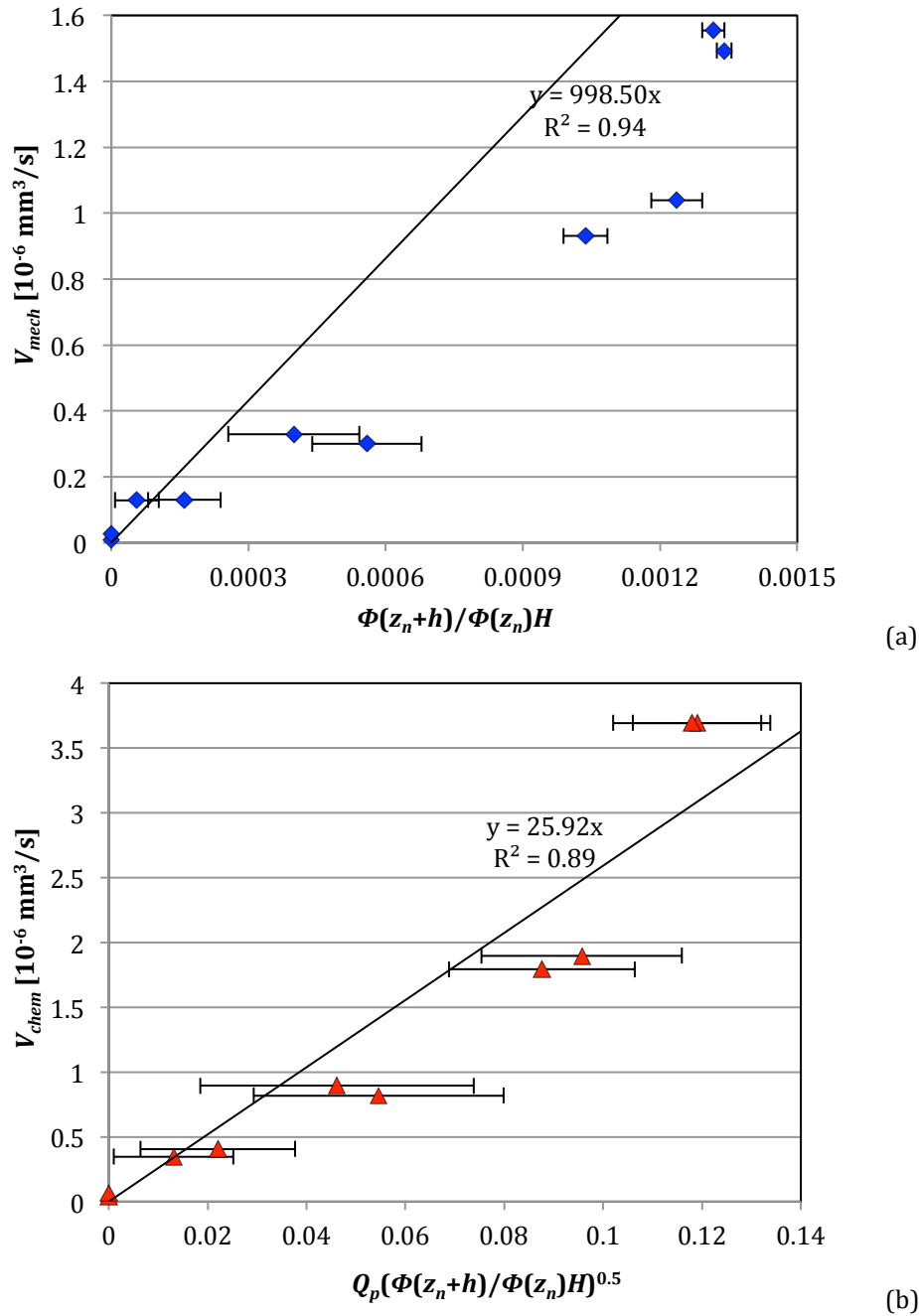
Figure 7.13 The correlation between mechanical (a) and chemical (b) wear rates and the group of variables

7.4 Discussion

A mechanistic wear model was developed in this chapter, which considers tribocorrosion and lubrication effects based on the geometrical real contact between asperities in mixed lubrication regime. The model was applied to an experimental study and compared to the experimental results. Since the real contact and surface topography during the experiments could not be measured,

the surface topography of the wear track after wear testing was used based on some hypotheses. Relatively good correlations were found between the model predictions and experimental results despite a certain errors from the determination of $\Phi(z_n)$ and $\Phi(z_n+h_{min})$ using the Abbott – Firestone curves. It should be noted that the quality of the Abbott – Firestone curves based on a vast database might be improved by increasing the resolution of the surface profile measurements. In the current surface topography measurement, the vertical resolution is pretty high, 0.1 nm which is much lower than the asperity height as shown in Figure 7.12(b). However, the lateral resolution is 1.3 μm, which is a little low since the lateral size of the asperities is generally several micrometers as shown in Figure 7.12(b). Measurements with better lateral resolution may suppress the errors in Figure 7.13.

Measurement of the asperity profiles of a wear track is a complex work. For example, in reciprocating ball-on-disk sliding, the wear track tends to follow a partial cylindrical shape with radius equal to that of the ball. To obtain the surface profile of the asperities, this general shape needs to be removed. The normal method is fitting the wear track using a cylindrical curve and then subtracting the wear surface by this fitted cylindrical curve. However, in real condition, the wear track is usually not with a perfect cylindrical shape and due to the scratches and hills in the wear track, this method may introduce big variation to the profiles of the asperities since the size of the asperities is normally much smaller comparing to the difference between the real surface and fitted shape. Line profile along the sliding direction is another method even may lose some information comparing to the surface profile. Line profile can be obtained along the sliding direction or perpendicular to the sliding direction. Comparing the first one, for the later one, the distance of the profile is limited by the width of the wear track and the problem of removing the cylindrical shape is still involved. This is the reason that in this study the line profiles along the sliding direction were used.

However, if it is known that the wear surface follows a certain distribution, the surface profile $\Phi(z)$ can thus be described by a known mathematical function, the whole surface profile and the Abbott – Firestone curve may not be necessary. For example, if it is found that the wear surface follows a Gaussian distribution,

only roughness R_q is needed in order to determine $\Phi(z_n)$ and $\Phi(z_n+h)$. Measuring roughness is usually simpler than the surface profile and Abbott – Firestone curve.

The surface profile of Gaussian distribution can be described by Equation (7.12) which is related to an error function erf(z). R_q is the root-mean-square roughness.

$$\Phi\left(\frac{z}{R_q}\right) = \frac{1}{2}\left[1 + \text{erf}\left(\frac{z}{\sqrt{2}R_q}\right)\right] \tag{7.12}$$

$$\text{erf}(z) = \frac{1}{\sqrt{\pi}}\int_{-z}^{z} e^{-x^2}\, dx \tag{7.13}$$

Based on that, the model can be modified, as shown in Equation (7.14):

$$V_{tot} = k'_{mech}\frac{F_n}{H}v_s\frac{1+\text{erf}\left(\frac{z_n+h}{\sqrt{2}R_q}\right)}{1+\text{erf}\left(\frac{z_n}{\sqrt{2}R_q}\right)} + k'_{chem}\frac{Q_pMv_s}{nF\rho}\left(\frac{F_n}{H}\right)^{0.5}\left(\frac{1+\text{erf}\left(\frac{z_n+h}{\sqrt{2}R_q}\right)}{1+\text{erf}\left(\frac{z_n}{\sqrt{2}R_q}\right)}\right)^{0.5} \tag{7.14}$$

With this assumption, only the surface roughness of the wear track needs to be measured instead of the whole surface profile and the Abbott – Firestone curve. This simplifies the application of the model to some situations where the wear surface profile follows a certain distribution such as Gaussian distribution. Unfortunately, this simplification can not be applied to the present experimental data since the asperity profiles do not follow Gaussian height distribution as indicated by the asymmetry in the Abbott – Firestone curves (Figure 7.12c).

It is clear that the wear surface topography is very important in this model. The surface topography during wear is expected to change gradually due to the plastic deformation of the materials, which is indicated by the running-in and steady state transition found in the wear of MoM artificial hip joints. However, the model currently doesn't consider the evolution of the wear surface topography due to the lack of tools to anticipate this evolution. The numerical simulation of the wear surface evolution [46,47] could be a useful tool to be combined with this model in order to predict the instantaneous wear rate due to the evolution of the wear surface topography and more precisely predict the final wear rates.

7.5 Conclusion

A first attempt to mechanistically model the effective normal load in lubricated condition was made in order to expand the applicability of the composite model into more general lubricated tribocorrosion condition. Following conclusions can be drawn:

(1) The lubrication effect in tribometer conditions is verified by changing the viscosity of the solutions. The total wear was found effectively reduced by increasing the viscosity of the solution thus increasing the hydrodynamic film thickness.

(2) Dowson's wear – minimum hydrodynamic film thickness correlation extracted from the running-in wear of MoM hip joint simulators is confirmed in tribometer conditions.

(3) The effective normal load is mechanistically modeled based on the topography of the contact surface and the hydrodynamic film thickness.

(4) A new mechanistic wear model is developed by replacing Dowson's empirical correlation by the mechanistic effective normal load model.

(5) The validity of the approach was assessed using the tribocorrosion experiments carried out in H_2SO_4 – glycerol solutions. The experimental mechanical and chemical wear rates were found to be consistent with this model approach.

Chapter 8 General discussion

In this study, tribocorrosion modeling of passive metals in lubricated conditions was carried out, which was initiated from the running-in wear modeling for MoM artificial hip joints and then attempted to be generalized to more general lubricated tribocorrosion conditions.

The first model developed in this study combines the tribocorrosion model and Dowson's running-in wear – minimum hydrodynamic film thickness correlation to quantitatively describe and predict tribocorrosion of passive metals in lubricated conditions. The key connection between them is the effective normal load which is the load carried only by the contacting asperities in lubricated condition. It is believed that only this load induces wear. Clearly, this load in lubricated condition is normally smaller than the total applied normal load and varies with the extent of lubrication effect. The extent of lubrication effect can be represented by the hydrodynamic film thickness and the idea is that higher hydrodynamic film thickness will decrease the fraction of asperity contact and thus the effective normal load, thus higher fraction of the total normal load will be carried by the lubricant, which doesn't induce wear.

Strictly speaking, this model is currently only valid for CoCrMo alloys in MoM hip joints condition due to the empirical nature of Dowson's correlation, which is extracted from the running-in wear of CoCrMo MoM hip joint simulator experiments. The Dowson's equation is in principle valid for the specific roughness found in artificial hip joints characterized by R_a values of typically a few ten nanometers, i.e. satisfying the condition for mixed lubrication for the typical hydrodynamic film thicknesses established in hip joints. For smoother or rougher surfaces, the applicability of Dowson's equation needs to be verified. As can be imagined, except for the hydrodynamic film thickness, surface roughness could be another factor influencing the extent of asperity contact, while not yet considered in the current model.

The modeling is based on the mechanism of plastic deformation at asperity contacts followed by the corrosion and repassivation of the depassivated

surfaces. This mechanism has been proposed by the previous tribocorrosion studies and used to model the tribocorrosion of passive metals. It should be noted that other wear mechanisms such as cracking or fatigue may also prevail in lubricated tribocorrosion conditions. The wear under these mechanisms may not follow the model prediction. Also, the model doesn't consider the build up of third bodies, the formation of tribolayer and the deposition of proteins, which may happen in the wear of artificial hip joints and influence the degradation of the implanted metals.

The use of the model requires the calibration of the factors k_{mech} and k_{chem} and proper measurement of the involved parameters, especially the passivation charge density. Due to the lack of the measurement of passivation charge density and surface micro-hardness, the model was calibrated using a well-controlled tribometer experimental study. Quite good correlations were found between the wear rates and the parameters, which also indicates the applicability of Dowson's correlation in tribometer conditions. This was later confirmed by tribometer experiments in H_2SO_4 – glycerol solutions of different viscosities.

The applicability of the model to different CoCr alloys was checked by comparing to tribocorrosion experimental results carried out using three CoCr alloys of different carbide concentrations. Quite good correlations were found for the CoCr alloys except one alloy that showed no correlation in the mechanical wear. Surface analysis revealed a different wear mechanism prevailing in the tribocorrosion of this alloy, which confirms the state that the wear under different mechanisms from the plastic deformation of the asperities may not follow this model prediction. Also, the different slopes found from the three alloys confirm that the k_{mech} and k_{chem} are material dependent and should be calibrated for each specific material (or alloy).

Once the model is calibrated for CoCrMo alloys, the model predictions can be compared to the experimental results. The model was found to predict remarkably well the wear rates observed in tribometer tribocorrosion experiments and the running-in wear rates of MoM artificial hip joints tested in simulators considering the uncertainties from k_{mech}, k_{chem} which should be calibrated for different CoCr alloys and passivation charge density Q_p which was not measured in the simulator experiments.

The model shows very powerful ability to predict the instantaneous wear rate in very complicated situations such as hip joint simulators and to identify the dominating wear mechanisms (mechanical or chemical). The model also allows evaluating the influence of material, mechanical, electrochemical, and physical parameters.

According to the model, both mechanical and chemical wear significantly contribute to MoM hip joint degradation. Thus, predictions based on only one mechanism likely lead to erroneous conclusions. This is for example the case of head radius that while having a significant effect on mechanical wear little affects chemical wear. The model also predicts that MoM hip joint damage occurs also during the swing phase in a single gait cycle and this is because of the large contribution of chemical wear. The model shows that wear accelerated corrosion (chemical wear) dominates metal degradation of MoM hip joints at larger head radii and smaller clearances.

As described before, the model surfers some limitations. However, despite these limitations, the model predicts very well the wear rates observed both in tribometer and simulator experiments. Firstly, this can be due to the fact that polished smooth samples were used in the tribometer and simulator experiments and the wear surfaces were also found relatively smooth (local roughness in several tens nanometer scale), thus the conditions for Dowson's correlation are generally fulfilled. Secondly, the model is based on the plastic deformation of the contacting asperities, which is commonly observed in these experimental studies. Other mechanisms such as third body generation seems not the dominating wear mechanism on the wear of CoCrMo alloys but may happen and contribute to the scattering of the wear results found in the tribometer and hip joint simulator experiments.

In order to overcome the limitation from Dowson's empirical correlation, it is then attempted to develop a mechanistic model to describe the extent of the effective normal load. Surface profiles of the asperities were considered and based on the distribution of the surface asperity heights, the real contact area can be geometrically obtained, which is proportional to the effective normal force. Clearly, in this model, the topography of the wear surface is needed in order determine the real contact area.

To obtain the real contact of the asperities, two hypotheses need to be made. Wear surfaces were under elastic and plastic deformations during loading, while surface profiles are usually measured after wear tests. The elastically deformed surfaces can recover, which may induce the asperity profiles without loading different from the ones during loading. However, the asperity profile during loading is normally unable to be measured. So the surface profiles after wear tests were used based on the hypothesis that the plastic deformation of the asperities remains and the difference between with and without loading is the elastic deformation inducing the change of the general shape of the contacting surfaces (waviness). This waviness can be removed by applying a cut-off to the profiles of the wear surface. From the comparison between the model predictions and the experimental results, this hypothesis was found reasonable.

To obtain the profiles of the surface asperities, the general form (waviness) of the wear surface should be removed. This is currently unable to be done for surface profiles if the surface doesn't have a regular shape (e.g. sphere, cylinder). In this study, the Abbott – Firestone curve of the line profiles in the wear surfaces after wear test were used. This is based on the hypothesis that the asperity profiles are uniform in every direction when the waviness is removed. The waviness of the profile was removed by applying a cut-off to the profiles. Clearly, the resolution of the profiles obtained from the profilometer may limit the precision in the determination of the real contact area.

As a first attempt, the model predictions are consistent with the current experimental results. Higher resolution in the profile measurements and more experimental results may reduce the scattering in the determination of the asperity contact area and increase the quality of the correlation between model prediction and experimental results.

As a general limitation, the models didn't consider time dependent effects. As a consequence of wear, the asperity height and thus the surface roughness are expected to steadily decrease with sliding time. This implies that a larger fraction of the load is progressively carried by the hydrodynamic film to the detriment of the load transmitted by asperities contacts. The wear rate should correspondingly decrease with time. This is indeed observed in hip joint simulator where, after an initial high wear phase (running-in period), the wear

rate becomes smaller and even negligible (steady state period). So, to generalize the model, surface topography evolution should be included. Tools to anticipate the evolution of surface topography during wear are needed. As a possible method, numerical method has been used to describe the evolution of the wear surface based on the deformation of the materials. The model could be combined with the numerical method to predict the instantaneous wear rate considering tribocorrosion, lubrication and real time surface topography.

Chapter 9 Conclusions

A tribocorrosion model for passive metals undergoing plastic deformation at asperity contacts combining mechanical wear (Archard's law), chemical wear (wear accelerated corrosion) and hydrodynamic fluid lubrication was proposed to quantitatively describe and predict material damage of passive metals. The model allows identifying the dominating wear mechanisms (mechanical or chemical) and evaluating the influence of well-defined material, mechanical, electrochemical and lubrication related parameters.

As applied to CoCrMo sliding tribocorrosion contacts, the model predicts remarkably well wear rates observed in tribometers and the running-in wear rates of MoM artificial hip joints tested in simulators. The model predictions concerning the effect of parameters such as head radius and clearance closely correlate with experimental observations.

The model allows thus to describe the effect of engineering relevant parameters such as head radius and clearance on the in vitro and in vivo degradation of CoCrMo artificial hip joints. As such, it constitutes a new and reliable theoretical tool for the development and optimization of biomedical alloys used in artificial hip joints.

The generalization of the model requires developing a mechanistic based approach to describe the effective normal force acting on asperities as an alternative to the Dowson's empirical correlation. Such an approach considering the asperity profile height distribution (Abbott – Firestone curves) and the hydrodynamic film thickness was proposed here and successfully compared to dedicated experiments. This shows that surface topography must be considered in order to better predict tribocorrosion rates in lubricated conditions.

Chapter 10 References

[1]   G.K. McKee, J. Watson-Farrar. Replacement of arthritic hips by the McKee-Farrar prosthesis. Journal of Bone and Joint Surgery-British Volume 48B (1966) 245-259.

[2]   J. Charnley. Arthroplasty of the hip: A new operation. The Lancet 277 (1961) 1129-1132.

[3]   A. Neville, Y. Yan. Biotribocorrosion: surface interactions in total joint replacement (TJR), in: D. Landolt, S. Mischler (Eds.), Tribocorrosion of Passive Metals and Coatings. Woodhead Publishing Limited, 2011, pp. 337-367.

[4]   I. Catelas, J.B. Medley, P.A. Campbell, et al. Comparison of in vitro with in vivo characteristics of wear particles from metal-metal hip implants. Journal of Biomedical Materials Research Part B: Applied Biomaterials 70B (2004) 167-178.

[5]   M.A. Wimmer, C. Sprecher, R. Hauert, et al. Tribochemical reaction on metal-on-metal hip joint bearings: A comparison between in-vitro and in-vivo results. Wear 255 (2003) 1007-1014.

[6]   S. Mischler, A. Igual Munoz. Wear of CoCrMo alloys used in metal-on-metal hip joint: A tribocorrosion appraisal. Wear 297(2013) 1081-1094.

[7]   R.M. Urban, J.J. Jacobs, M.J. Tomlinson, et al. Dissemination of wear particles to the liver, spleen, and abdominal lymph nodes of patients with hip or knee replacement. Journal of Bone and Joint Surgery-American Volume 82 (2000) 457-477.

[8]   L. Mattei, F.D. Puccio, B. Piccigallo, et al. Lubrication and wear modelling of artificial hip joints: A review. Tribology International 44 (2011) 532-549.

[9]   R.M. Hall, T.D. Brown, J. Fisher, et al. Introduction to lumbar total disc replacement: factors that affect tribological performance. Proceedings of the Institution of Mechanical Engineers. Part J: Journal of Engineering Tribology 220 (2006) 775-786.

[10]   L.H. Gill. Challenges in total ankle arthroplasty. Foot & Ankle International

25 (2004) 195-207.

[11] D. Nam, C.K. Kepler, S.J. Nho, et al. Observations on retrieved humeral polyethylene components from reverse total shoulder arthroplasty. Journal of Shoulder and Elbow Surgery 19 (2010) 1003-1012.

[12] S. Kurtz, K. Ong, E. Lau, et al. Projections of primary and revision hip and knee arthroplasty in the United States from 2005 to 2030. Journal of Bone and Joint Surgery-American Volume 89 (2007) 780-785.

[13] E. Ingham, J. Fisher. The role of macrophages in osteolysis of total joint replacement. Biomaterials 26 (2005) 1271-1286.

[14] O.M. Posada, R.J. Tate, M.H. Grant. Effects of CoCr metal wear debris generated from metal-on-metal hip implants and Co ions on human monocyte-like U937 cells. Toxicology in Vitro 29 (2015) 271-280.

[15] D.O. Molloy, S. Munir, C.M. Jack, et al. Fretting and corrosion in modular-neck total hip arthroplasty femoral stems. Journal of Bone and Joint Surgery-American Volume 96 (2014) 488-493.

[16] G. Gkagkalis, P. Mettraux, P. Omoumi, et al. Adverse tissue reaction to corrosion at the neck-stem junction after modular primary total hip arthroplasty. Orthopaedics & Traumatology: Surgery & Research 101 (2015) 123-126.

[17] N. Diomidis, S. Mischler, N.S. More, et al. Tribo-electrochemical characterization of metallic biomaterials for total joint replacement. Acta Biomaterialia 8 (2012) 852-859.

[18] R.M. Streicher, M. Semlitsch, R. Schön, et al. Metal-on-metal articulation for artificial hip joints: laboratory study and clinical results, Proceedings of the Institution of Mechanical Engineers. Part H: Journal of Engineering in Medicine 210 (1996) 223-232.

[19] A.W. Hodgson, S. Mischler, B. Von Rechenberg, et al. An analysis of the in vivo deterioration of Co-Cr-Mo implants through wear and corrosion. Proceedings of the Institution of Mechanical Engineers. Part H: Journal of Engineering in Medicine 221 (2007)291-303.

[20] M. Huber, G. Reinisch, G. Trettenhahn, et al. Presence of corrosion products and hypersensitivity-associated reactions in periprosthetic tissue after aseptic loosening of total hip replacements with metal bearing surfaces.

Acta Biomaterialia 5 (2009) 172-180.

[21] R. Büscher, A. Fischer. The pathways of dynamic recrystallization in all-metal hip joints. Wear 259 (2005) 887-897.

[22] D. Dowson. The relationship between steady-state wear rate and theoretical film thickness in metal-on-metal total replacement hip joints, in: D. Dowson, M. Priest, G. Dalmaz, A.A. Lubrecht (Eds.), Tribological Research and Design for Engineering Systems, Elsevier, 2003, pp. 273-280.

[23] D. Dowson. Tribological principles of metal-on-metal hip joint design. Proceedings of the Institution of Mechanical Engineers. Part H: Journal of Engineering in Medicine 220 (2006) 161–171.

[24] S. Mischler. Triboelectrochemical techniques and interpretation methods in tribocorrosion: A comparative evaluation. Tribology International 41 (2008) 573-583.

[25] A.I. Munoz, N. Espallargas. Tribocorrosion mechanisms in sliding contacts, in: D. Landolt, S. Mischler (Eds.), Tribocorrosion of Passive Metals and Coatings. Woodhead Publishing Limited, 2011, pp. 118-152.

[26] S. Mischler, S. Debaud, D. Landolt. Wear-accelerated corrosion of passive metals in tribocorrosion systems. Journal of the Electrochemical Society 145 (1998) 750-758.

[27] Y. Yan, A. Neville, D. Dowson, et al. Electrochemical instrumentation of a hip simulator: a new tool for assessing the role of corrosion in metal-on-metal hip joints. Proceedings of the Institution of Mechanical Engineers Part H-Journal of Engineering in Medicine 224 (2010) 1267-1273.

[28] J. Hesketh, X. Hu, Y. Yan, et al. Biotribocorrosion: Some electrochemical observations from an instrumented hip joint simulator. Tribology International 59 (2013) 332-338.

[29] D. Landolt, S. Mischler, M. Stemp. Electrochemical methods in tribocorrosion: a critical appraisal. Electrochimica Acta 46 (2001) 3913-3929.

[30] S. Guadalupe, S. Mischler, M. Cantoni, et al. Mechanical and chemical mechanisms in the tribocorrosion of a Stellite type alloy. Wear 308 (2013) 213-221.

[31] D. Landolt. Corrosion and Surface Chemistry of Metals. EPFL Press,

Lausanne, 2007.

[32] A. Bazzoni, S. Mischler, N. Espallargas. Tribocorrosion of pulsed plasma-nitrided CoCrMo implant alloy. Tribology Letters 49 (2013) 157-167.

[33] S. Mischler, A. Spiegel, M. Stemp, et al. Influence of passivity on the tribocorrosion of carbon steel in aqueous solutions. Wear 251 (2001) 1295-1307.

[34] A.I. Munoz, L.C. Julián. Influence of electrochemical potential on the tribocorrosion behaviour of high carbon CoCrMo biomedical alloy in simulated body fluids by electrochemical impedance spectroscopy. Electrochimica Acta 55 (2010) 5428–5439.

[35] H.H. Uhlig. Mechanism of fretting corrosion. Journal of Applied Mechanics 21 (1954) 401-407.

[36] J.F. Archard. Contact and rubbing of flat surfaces. Journal of Applied Physics. 24 (1953) 981-988.

[37] D. Dowson. Elastohydrodynamic and micro-elastohydrodynamic lubrication. Wear 190 (1995) 125-138.

[38] I.M. Hutchings. Tribology: Friction and Wear of Engineering Materials. CRC Press, 1992.

[39] B. Hamrock, D. Dowson. Elastohydrodynamic lubrication of elliptical contacts for material of low elastic modulus I-Fully Flooded Conjunction. Journal of Lubrication Technology 100 (1978) 236-245.

[40] D. Dowson. The relationship between steady-state wear rate and theoretical film thickness in metal-on-metal total replacement hip joints, in: D. Dowson D (Ed), Tribological Research and Design for Engineering Systems. Elsevier, 2003, pp. 273-280.

[41] C. Priestner, H. Allmaier, H.H. Priebsch, et al. Refined simulation of friction power loss in crank shaft slider bearings considering wear in the mixed lubrication regime. Tribology International 46 (2012) 200-207.

[42] C.B. Rieker, R. Schon, R. Konrad, et al. Influence of the clearance on in-vitro tribology of large diameter metal-on-metal articulations pertaining to resurfacing hip implants. Orthopedic Clinics of North America 36 (2005) 135–142.

[43] T.A. Maxian, T.D. Brown, D.R. Pedersen, et al. Finite element analysis of

acetabular wear: Validation, and fixation and backing effects. Clinical Orthopaedics and Related Research 344 (1997) 111–117.

[44] M.T. Raimondi, C. Santambrogio, R. Pietrabissa, et al. Improved mathematical model of the wear of the cup articular surface in hip joint prostheses and comparison with retrieved components. Proceedings of the Institution of Mechanical Engineers. Part H: Journal of Engineering in Medicine 215 (2001) 377–391.

[45] J.S.S. Wu, J.P. Hung, C.S. Shu, et al. The computer simulation of wear behavior appearing in total hip prosthesis. Computer Methods and Programs in Biomedicine 70 (2003) 81–91.

[46] F. Liu, I. Leslie, S. Williams, et al. Development of computational wear simulation of metal-on-metal hip resurfacing replacements. Journal of Biomechanics 41 (2008) 686–694.

[47] M.S. Uddin, L.C. Zhang. Predicting the wear of hard-on-hard hip joint prostheses. Wear 301 (2013) 192-200.

[48] M. Azzi, J.-E. Klemberg-Sapieha. Tribocorrosion test protocols for sliding contacts, in: D. Landolt, S. Mischler (Eds.), Tribocorrosion of Passive Metals and Coatings, Woodhead Publishing Limited, 2011, pp. 222-238.

[49] A.C. Vieira, L.A. Rocha, N. Papageorgiou, et al. Mechanical and electrochemical deterioration mechanisms in the tribocorrosion of Al alloys in NaCl and in $NaNO_3$ solutions. Corrosion Science 54 (2012) 26-35.

[50] S. Guadalupe. Tribocorrosion in pressurized high temperature water: a mass flow model based on the third body approach. PhD Thesis, EPFL, 2014.

[51] L. Benea, P. Ponthiaux, F. Wenger, et al. Tribocorrosion of stellite 6 in sulphuric acid medium: electrochemical behaviour and wear. Wear 256 (2004) 948-953.

[52] J.C. Shin, J.M. Doh, J.K. Yoon, et al. Effect of molybdenum on the microstructure and wear resistance of cobalt-base Stellite hardfacing alloys. Surface & Coating Technology 166 (2003) 117-126.

[53] H. Yu, R. Ahmed, H.D. Lovelock, et al. Influence of Manufacturing Process and Alloying Element Content on the Tribomechanical Properties of Cobalt-Based Alloys. Journal of Tribology-Transactions of the ASME 131

(2009) 011601-1-12.

[54] M.X. Yao, J.B.C. Wu, Y. Xie. Wear, corrosion and cracking resistance of some W- or Mo-containing Stellite hardfacing alloys. Materials Science and Engineering A-Structural Materials Properties Microstructure and Processing 407 (2005) 234-244.

[55] A.I. Munoz, S. Mischler. Effect of the environment on wear ranking and corrosion of biomedical CoCrMo alloys. Journal of Materials Science: Materials in Medicine 22 (2011) 437-450.

[56] M. Stemp, S. Mischler, D. Landolt. The effect of mechanical and electrochemical parameters on the tribocorrosion rate of stainless steel in sulphuric acid. Wear 255 (2003) 466–475.

[57] C. Myant, P. Cann. On the matter of synovial fluid lubrication: Implications for metal-on-metal hip tribology. Journal of the Mechanical Behavior of Biomedical Materials 34 (2014) 338-348.

[58] J. Stojadinovic, D. Bouvet, M. Declercq, et al. Influence of chelating agents on the tribocorrosion of tungsten in sulphuric acid solution. Electrochimica Acta 56 (2011) 7131–7140.

[59] P. Jemmely, S. Mischler, D. Landolt. Electrochemical modeling of passivation phenomena in tribocorrosion. Wear 237 (2000) 63-76.

[60] J.A. Bardwell, G.I. Sproule, M.J. Graham. Ex situ surface analysis of passive films on Fe-Cr alloys. Journal of the Electrochemical Society 140 (1993) 50-53.

[61] J.A. Bardwell, G.I. Sproule, D.F. Mitchell, et al. Nature of the passive film on Fe-Cr alloys as studied by [18]O secondary ion mass spectrometry: reduction of the prior film and stability to ex situ surface analysis. Journal of the Chemical Society-Faraday Transactions 87 (1991) 1011-1019.

[62] A.W.E. Hodgson, S. Kurz, S. Virtanen, et al. Passive and transpassive behaviour of CoCrMo in simulated biological solutions. Electrochimica Acta 49 (2004) 2167-2178.

[63] L.C. Julián, A.I. Munoz. Influence of microstructure of HC CoCrMo biomedical alloys on the corrosion and wear behaviour in simulated body fluids. Tribology International 44 (2011) 318–329.

[64] J.P. Paul. Forces transmitted by joints in the human body. Proceedings of

the Institution of Mechanical Engineers, Conference Proceedings, 181 (1966) 8-15.

[65] R.C. Johnston, G.L. Smidt. Measurement of hip-joint motion during walking-evaluation of an electrogoniometric method. Journal of Bone and Joint Surgery-American Volume 51A (1969) 1083-1094.

[66] D. Dowson, B. Jobbins. Design and development of a versatile hip joint simulator and a preliminary assessment of wear and creep in Charnley total replacement hip joints. Engineering in Medicine 17 (1988) 111-117.

[67] O. Calonius, V. Saikko. Force track analysis of contemporary hip simulators. Journal of Biomechanics 36 (2003) 1719-1726.

[68] O. Calonius, V. Saikko. Slide track analysis of eight contemporary hip simulator designs. Journal of Biomechanics 35 (2002) 1439-1450.

[69] V. Saikko, O. Calonius. Slide track analysis of the relative motion between femoral head and acetabular cup in walking and in hip simulators. Journal of Biomechanics 35 (2002) 455-464.

[70] J.B. Medley, J.M. Dowling, R.A. Poggie, et al. Simulator wear of some commercially available metal-on-metal hip implants, in: J.J. Jacobs, T.L. Craig (Eds.) Alternative Bearing Surfaces in Total Joint Replacement, American Society Testing and Materials, W Conshohocken, 1998, pp. 92-110.

[71] F.W. Chan, J.D. Bobyn, J.B. Medley, et al. Wear and lubrication of metal-on-metal hip implants. Clinical Orthopaedics and Related Research 369 (1999) 10-24.

[72] P. Pare, J.B. Medley, F.W. Chan, et al. On the role of the lambda parameter in simulator wear of metal-on-metal hip implants, in: D. Dowson, M. Priest, G. Dalmaz, A.A. Lubrecht (Eds.), Tribological Research and Design for Engineering Systems, Elsevier, 2003, pp. 281-290.

[73] I. Catelas, J.D. Bobyn, J.B. Medley, et al. Size, shape, and composition of wear particles from metal–metal hip simulator testing: Effects of alloy and number of loading cycles. Journal of Biomedical Materials Research Part A 67A (2003) 312-327.

[74] K.R. St. John, L.D. Zardiackas, R.A. Poggie. Wear evaluation of cobalt–chromium alloy for use in a metal-on-metal hip prosthesis. Journal of

Biomedical Materials Research Part B: Applied Biomaterials 68B (2004) 1-14.

[75] J.G. Bowsher, J. Nevelos, P.A. Williams, et al. 'Severe' wear challenge to 'as-cast' and 'double heat-treated' large-diameter metal-on-metal hip bearings. Proceedings of the Institution of Mechanical Engineers. Part H: Journal of Engineering in Medicine 220 (2006) 135-143.

[76] A. Angadji, M. Royle, S.N. Collins, et al. Influence of cup orientation on the wear performance of metal-on-metal hip replacements. Proceedings of the Institution of Mechanical Engineers. Part H: Journal of Engineering in Medicine 223 (2009) 449-457.

[77] J.G. Bowsher, I.C. Clarke, P.A. Williams, et al. What is a "Normal" wear pattern for metal-on-metal hip bearings? Journal of Biomedical Materials Research Part B: Applied Biomaterials 91B (2009) 297-308.

[78] A.A.J. Goldsmith, D. Dowson, G.H. Isaac, et al. A comparative joint simulator study of the wear of metal-on-metal and alternative material combinations in hip replacements. Proceedings of the Institution of Mechanical Engineers. Part H: Journal of Engineering in Medicine 214 (2000) 39-47.

[79] D. Dowson, C. Hardaker, M. Flett, et al. A hip joint simulator study of the performance of metal-on-metal joints: Part I: The role of materials. The Journal of Arthroplasty 19 (2004) 118-123.

[80] D. Dowson, C. Hardaker, M. Flett, et al. A hip joint simulator study of the performance of metal-on-metal joints: Part II: design. The Journal of Arthroplasty 19 (2004) 124-130.

[81] I.J. Leslie, S. Williams, C. Brown, et al. Surface engineering: A low wearing solution for metal-on-metal hip surface replacements. Journal of Biomedical Materials Research Part B: Applied Biomaterials 90B (2009) 558-565.

[82] C.X. Li, A. Hussain, A. Kamali. A hip simulator study of metal-on-metal hip joint device using acetabular cups with different fixation surface conditions. Proceedings of the Institution of Mechanical Engineers. Part H: Journal of Engineering in Medicine 225 (2011) 877-887.

[83] J. Hesketh, Q. Meng, D. Dowson, et al. Biotribocorrosion of metal-on-metal hip replacements: How surface degradation can influence metal ion

formation. Tribology International 65 (2013) 128-137.

[84] Y. Yan, A. Neville, J. Hesketh, et al. Real-time corrosion measurements to assess biotribocorrosion mechanisms with a hip simulator. Tribology International 63 (2013) 115-122.

[85] M. Al-Hajjar, J. Fisher, S. Williams, et al. Effect of femoral head size on the wear of metal on metal bearings in total hip replacements under adverse edge-loading conditions. Journal of Biomedical Materials Research Part B: Applied Biomaterials 101B (2013) 213-222.

[86] S.C. Scholes, S.M. Green, A. Unsworth. The wear of metal-on-metal total hip prostheses measured in a hip simulator. Proceedings of the Institution of Mechanical Engineers. Part H: Journal of Engineering in Medicine 215 (2001) 523-530.

[87] P.J. Firkins, J.L. Tipper, M.R. Saadatzadeh, et al. Quantitative analysis of wear and wear debris from metal-on-metal hip prostheses tested in a physiological hip joint simulator. Bio-Medical Materials and Engineering 11 (2001) 143-157.

[88] J.P. Kretzer, M. Krachler, J. Reinders, et al. Determination of low wear rates in metal-on-metal hip joint replacements based on ultra trace element analysis in simulator studies. Tribology International 37 (2010) 23-29.

[89] M. Keddam, F. Wenger. Electrochemical methods in tribocorrosion, in: D. Landolt, S. Mischler (Eds.), Tribocorrosion of Passive Metals and Coatings. Woodhead Publishing, Cambridge, 2011, pp. 187-221.

[90] S. Cao, S. G. Maldonado, S. Mischler. Tribocorrosion of passive metals in the mixed lubrication regime: theoretical model and application to metal-on-metal artificial hip joints. Wear 324–325 (2015) 55-63.

[91] G. Bergmann, G. Deuretzbacher, M. Heller, et al. Hip contact forces and gait patterns from routine activities. Journal of Biomechanics 34 (2001) 859-871.

[92] P.A. Varady, U. Glitsch, P. Augat. Loads in the hip joint during physically demanding occupational tasks: A motion analysis study. Journal of Biomechanics 48 (2015) 3227-3233.

[93] T.Y. Tsai, D. Dimitriou, J.S. Li, et al. Asymmetric hip kinematics during gait in patients with unilateral total hip arthroplasty: In vivo 3-dimensional

motion analysis. Journal of Biomechanics 48 (2015) 555-559.

[94] J.N.D. Torrão, M.P.S. dos Santos, J.A.F. Ferreira. Instrumented knee joint implants: innovations and promising concepts. Expert Review of Medical Devices 12 (2015) 571-584.

[95] A.I. Munoz, J. Schwiesau, B.M. Jolles, et al. In vivo electrochemical corrosion study of a CoCrMo biomedical alloy in human synovial fluids. Acta Biomaterialia 21 (2015) 228-236.

[96] J. Schurz, V. Ribitsch. Rheology of synovial fluid. Biorheology 24 (1987) 385-399.

[97] R. Büscher, G. Täger, W. Dudzinski, et al. Subsurface microstructure of metal-on-metal hip joints and its relationship to wear particle generation. Journal of Biomedical Materials Research Part B: Applied Biomaterials 72B (2005) 206-214.

[98] T. Ilchmann, M. Reimold, W. Muller-Schauenburg. Estimation of the wear volume after total hip replacement: A simple access to geometrical concepts. Medical Engineering & Physics 30 (2008) 373-379.

[99] G. Reinisch, K.P. Judmann, C. Lhotka, et al. Retrieval study of uncemented metal–metal hip prostheses revised for early loosening. Biomaterials 24 (2003) 1081-1091.

[100] J. Stojadinović, D. Bouvet, M. Declercq, et al. Effect of electrode potential on the tribocorrosion of tungsten. Tribology International 42 (2009) 575-583.

[101] J.B. Segur, H.E. Oberstar. Viscosity of glycerol and its aqueous solutions. Industrial & Engineering Chemistry 43(1951) 2117-2120.

[102] N.S. Cheng. Formula for the viscosity of a glycerol–water mixture. Industrial & Engineering Chemistry Research 47 (2008) 3285-3288.

[103] K.L. Johnson. Contact Mechanics. Cambridge University Press, Cambridge, 1985.

List of symbols

a	Maximum deviation of a surface profile (mm)
A	Contact area (mm^2)
$A_{i,ave}$	Average contact area of each asperity (mm^2)
A_{real}	Real contact area (mm^2)
A_n	The contact area when effective normal load reaches total normal load (mm^2)
A_{tot}	Total contact area (mm^2)
b	Proportionality factor
c_R	Radial clearance (mm)
E	Young's modulus (GPa)
E'	Effective Young's modulus (GPa)
$E_{electrode}$	Electrode potential (V)
E_p	Passive potential (V)
E_b	Transpassive potential (V)
erf	Error function
F	Faraday's constant (C/mol)
F_n	Normal force (N)
F_{eff}	Effect normal force carried by asperities (N)
h	Film thickness (nm)
h_{min}	Minimum film thickness (nm)
h_t	Depth of the wear track (mm)
H	Surface hardness (HV)
I_p	The excess current (mA)
k	Proportionality factor
κ	Conductivity (mS/cm)
K	Proportionality factor
k_0	Proportionality factor for effective normal load
k_c	Proportionality factor for chemical wear in tribocorrosion
k_m	Proportionality factor for mechanical wear in tribocorrosion
k_{mech}	Proportionality factor for mechanical wear in lubricated tribocorrosion
k_{chem}	Proportionality factor for chemical wear in lubricated tribocorrosion
k'_{mech}	Proportionality factor for mechanical wear in lubricated tribocorrosion
k'_{chem}	Proportionality factor for chemical wear in lubricated tribocorrosion
L	Sliding distance (mm)
M	Atomic mass (g/mol)
n	Oxidation valence
n_a	The number of asperities

n_r	The million cycles (or years) at the end of running-in period
n_t	The actual number of accomplished million cycles (or years)
ρ	Density (g/cm^3)
Q_p	Passivation charge density (mC/cm^2)
R	Radius of curvature (mm)
R'	Effective radius of curvature (mm)
R_a	Arithmetic average line roughness (µm)
R_a'	Composite arithmetic average line roughness (µm)
R_{dep}	Depassivation rate (mm^2/s)
R_q	Square root mean line roughness (µm)
t	Time (s)
u	Entraining velocity (mm/s)
μ	Coefficient of friction
U_{cap}	Volume of the cap in the wear track (mm^3)
U_{tot}	Total wear volume (mm^3)
U_{track}	Volume of the wear track (mm^3)
U_{mech}	Mechanical wear volume (mm^3)
U_{chem}	Chemical wear volume (mm^3)
U_{linear}	Linear wear volume (mm^3)
$U_{running-in}$	Running-in wear volume (mm^3)
V_{tot}	Total wear rate (mm^3/s)
V_{mech}	Mechanical wear rate (mm^3/s)
V_{chem}	Chemical wear rate (mm^3/s)
ν	Poisson's ratio
v_s	Sliding velocity (mm/s)
vol.%	Volumetric percentage
ω	Angular velocity (rad/s)
wt.%	Weight percentage
z	Deviation of the surface profile (mm)
z_0	Contacting level (mm)
z_n	Contacting level when effective normal load reaches total normal load (mm)
σ_s	Contact stress (Pa)
η	Viscosity of solution (Pa·s)
λ	Lambda ratio
ϕ	Probability function
Φ	Cumulative distribution function

List of abbreviations

AA	Abduction-adduction
ASTM	American society for testing and materials
BS	Bovine serum
BSA	Bovine serum albumin
CDF	Cumulative distribution function
CE	Counter electrode
CoF	Coefficient of friction
CoC	Ceramic-on-ceramic
CoM	Ceramic-on-metal
CoP	Ceramic-on-polymer
cP	Centipoise
EDTA	Ethylenediaminetetraacetic acid
FE	Flexion-extension
FEM	Finite element method
FIB	Focused ion beam
HC	High carbon
IE	Internal-external
IER	Internal-external rotation
ISO	International organizations for standardization
LC	Low carbon
MoM	Metal-on-metal
MoP	Metal-on-polymer
MSE	Standard mercury sulfate electrode
OCP	Open circuit potential
PMMA	Poly(methyl methacrylate)
RE	Reference electrode
SEM	Scanning electron microscope
SHE	Standard hydrogen electrode
THR	Total hip replacement
TKA	Total knee arthroplasty
UHMWPE	Ultra high molecular weight polyethylene
WE	Working electrode
XPS	X-ray photoelectron spectroscope

Curriculum Vitae

Shoufan CAO

Born December 29th, 1986 in Shandong, China

EDUCATION

2012-2016   Doctoral student and assistant in the Tribology and Interface Chemistry Group, Ecole Polytechnique Fédérale de Lausanne (EPFL), Switzerland under the supervision of Dr. Stefano Mischler.

2009-2012   Master student in the Institute of Tribology and Reliability Engineering, School of Materials Science and Engineering, China University of Mining and Technology.

2005-2009   Bachelor student in the School of Mechanical Engineering, Shandong Jiaotong University, China.

PUBLICATIONS

[1]   S. Cao, S. Guadalupe, S. Mischler. Tribocorrosion of passive metals in the mixed lubrication regime: theoretical model and application to metal-on-metal artificial hip joints. Wear (2015) 324-325: 55-63.

[2]   S. Cao, S. Mischler. Assessment of a recent tribocorrosion model for wear of metal-on-metal hip joints: Comparison between model predictions and simulator results. Wear (2016) 362-363: 170-178.

[3]   S. Cao, F. Sarasin, M. Cantoni, S. Mischler. Effect of surface films on tribological induced metallurgical transformations of steel in oil lubricated contacts. Wear (2016) 368-369: 75-83.

[4]   V. Gopal, M. Chandran, M.S.R. Rao, S. Mischler, S. Cao, G. Manivasagam. Tribocorrosion and electrochemical behaviour of nanocrystalline diamond coated Ti based alloys for orthopaedic application. Tribology International (2016), http://dx.doi.org/10.1016/j.triboint.2016.10.040.

ORAL PRESENTATIONS

[1]   The Swiss Tribology Technical Meeting, April 30th, 2014, EMPA Dubendorf, Switzerland. "Wear modeling of artificial hip joints combining tribocorrosion and lubrication".

[2]   The Swiss – Japanese Tribology Meeting, September 8-10th, 2014, ETHZ, Switzerland. "Tribocorrosion modeling of passive metals in mixed lubrication regime: application to metal-on-metal artificial hip joints".

[3]   21st Swiss Conference on Biomaterials and Regenerative Medicine, June 9-10th, 2015, EPFL, Switzerland. "Material degradation mechanism and wear modeling of metal-on-metal artificial hip joints".

[4]   42nd Leeds – Lyon Symposium on Tribology, September 7-9th, 2015, Lyon, France. "Wear modeling of metal-on-metal artificial hip joints by combining tribocorrosion and lubrication aspects".

[5]   EUROCORR 2016 Advances in Linking Science to Engineering, September 11-15th, 2016, Montpellier, France. "Tribocorrosion modeling of metal-on-metal hip joints including lubrication effects".

POSTERS

[1]   The 4th International Conference on Tribocorrosion, April 9-11th, 2014, "Wear modeling of artificial hip joints combining tribocorrosion and lubrication".

[2]   Gordon Research Conference – Tribology, Scientific Advancements for Critical Applications in Friction, Lubrication, and Wear, June 26th-July 1st, 2016, "Mechanistic wear model encompassing tribocorrosion and lubrication: From CoCrMo metal-on-metal artificial hip joints to generalization".

AWARD

[1]   The 2nd poster prize in the 4th International Conference on Tribocorrosion, April 2014.